

Flexible Antennas for Next-Generation Communication Systems

Lead Guest Editor: Binod Kumar Kanaujia

Guest Editors: Sachin Kumar, Kang Wook Kim, and Taimoor Khan





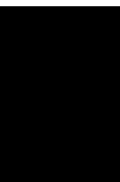
Flexible Antennas for Next-Generation Communication Systems

International Journal of Antennas and Propagation

Flexible Antennas for Next-Generation Communication Systems

Lead Guest Editor: Binod Kumar Kanaujia

Guest Editors: Sachin Kumar, Kang Wook Kim, and
Taimoor Khan






Copyright © 2022 Hindawi Limited. All rights reserved.

This is a special issue published in “International Journal of Antennas and Propagation.” All articles are open access articles distributed under the Creative Commons Attribution License, which permits unrestricted use, distribution, and reproduction in any medium, provided the original work is properly cited.

Chief Editor

Slawomir Koziel , Iceland


Associate Editors






Sotirios K. Goudos , Greece
N. Nasimuddin , Singapore
Ikmo Park , Republic of Korea

Academic Editors

Kush Agarwal , Singapore
Ana Alejos , Spain
Mohammad Ali, USA
Rodolfo Araneo, Italy
Hervé Aubert , France
Paolo Baccarelli , Italy
Xiulong Bao, Ireland
Giulio Maria Bianco , Italy
Pietro Bolli , Italy
Paolo Burghignoli , Italy
Shah Nawaz Burokur , France
Giuseppe Castaldi , Italy
Giovanni Andrea Casula , Italy
Luca Catarinucci, Italy
Felipe Cátedra , Spain
Marta Cavagnaro , Italy
Ayan Chatterjee , India
Maggie Y. Chen , USA
Shih Yuan Chen , Taiwan
Renato Cicchetti , Italy
Riccardo Colella , Italy
Laura Corchia , Italy
Claudio Curcio, Italy
Francesco D'Agostino , Italy
Michele D'Urso, Italy
María Elena De Cos Gómez , Spain
Arpan Desai, Taiwan
Alessandro Di Carlofelice , Italy
Giuseppe Di Massa , Italy
Flaminio Ferrara , Italy
Ravi Kumar Gangwar, India
Claudio Gennarelli , Italy
Farid Ghanem, Algeria
Rocco Guerriero , Italy
Kerim Guney, Turkey
Ashish Gupta , India
Tamer S. Ibrahim , USA




Muhammad Ramlee Kamarudin , Malaysia
Dmitry V. Kholodnyak , Russia
Rajkishor Kumar , India
Ping Li , China
Ding-Bing Lin , Taiwan
Angelo Liseno, Italy
Gui Liu , China
Pierfrancesco Lombardo , Italy
Lorenzo Luini , Italy
Giovanni Magno, Italy
Praveen Kumar Malik, India
Bappaditya Mandal, Sweden
Atsushi Mase, Japan
Diego Masotti , Italy
Christoph F. Mecklenbräuker , Austria
Ananda S. Mohan, Australia
Jose-Maria Molina-Garcia-Pardo , Spain
Giuseppina Monti , Italy
Giorgio Montisci , Italy
Andrea Francesco Morabito , Italy
Mohammad H. Neshati , Iran
Truong Khang Nguyen, Vietnam
Symeon Nikolaou , Cyprus
Amrindra Pal , India
Sandeep Kumar Palaniswamy, India
Mauro Parise , Italy
Josep Parrón, Spain
Shobhitkumar Patel , India
Anna Pietrenko-Dabrowska, Poland
Khaled ROUABAH, Algeria
MADAN KUMAR SHARMA, Oman
VISHAL SORATHIYA, India
Ahmad Safaai-Jazi, USA
Safieddin Safavi-Naeini, Canada
Stefano Selleri , Italy
Zijian Shao, USA
Raffaele Solimene , Italy
Gina Sorbello , Italy
Seong-Youp Suh, USA
Larbi Talbi, Canada
Luciano Tarricone, Italy
Sreenath Reddy Thummalur, India
Giuseppe Torrisi , Italy
Trushit Upadhyaya , India








Chien-Jen Wang , Taiwan
Mustapha C E Yagoub , Canada
Yuan Yao , China
Tao Zhou , China
Muhammad Zubair , Pakistan

Contents

On the Design and Development of Planar Monopole Antenna for Bone Crack/Void Detection

Ananda Venkatesan Boologam, Kalimuthu Krishnan , Sandeep Kumar Palaniswamy , Sachin Kumar , Shreya Bhowmik, Nivesh Sharma, Deepesh Vaish, and Sourish Chatterjee
Research Article (12 pages), Article ID 4663488, Volume 2022 (2022)



Conformal Quad-Port UWB MIMO Antenna for Body-Worn Applications

Thennarasi Govindan, Sandeep Kumar Palaniswamy , Malathi Kanagasabai , Sachin Kumar ,
Thipparaju Rama Rao , and Mohammed Gulam Nabi Alsath 
Research Article (13 pages), Article ID 9409785, Volume 2021 (2021)

Design and Performance Analysis of Compact Wearable Textile Antennas for IoT and Body-Centric Communication Applications

Sanjit Varma , Somia Sharma , Merbin John , Richa Bharadwaj , Anuj Dhawan , and Shibani K. Koul 
Research Article (12 pages), Article ID 7698765, Volume 2021 (2021)

A Novel Multiband Fractal Antenna for Wireless Application

Lan Wang , Jianguo Yu , Tangyao Xie, and Kun Bi
Research Article (9 pages), Article ID 9926753, Volume 2021 (2021)

Research Article

On the Design and Development of Planar Monopole Antenna for Bone Crack/Void Detection

Ananda Venkatesan Boologam, Kalimuthu Krishnan , Sandeep Kumar Palaniswamy , Sachin Kumar , Shreya Bhowmik, Nivesh Sharma, Deepesh Vaish, and Sourish Chatterjee

Department of Electronics and Communication Engineering, SRM Institute of Science and Technology, Kattankulathur, 603203, India

Correspondence should be addressed to Kalimuthu Krishnan; kalimutk@srmist.edu.in and Sandeep Kumar Palaniswamy; vrpchs@gmail.com

Received 23 July 2021; Revised 21 January 2022; Accepted 4 April 2022; Published 5 May 2022

Academic Editor: Hervé Aubert

Copyright © 2022 Ananda Venkatesan Boologam et al. This is an open access article distributed under the Creative Commons Attribution License, which permits unrestricted use, distribution, and reproduction in any medium, provided the original work is properly cited.

In this study, the design of a compact narrowband monopole antenna for bone crack detection is presented. The proposed antenna consists of a modified hexagon-shaped radiator with six triangular slits integrated on its bottom periphery, a rectangular-shaped ground plane, and a microstrip feed line of $50\ \Omega$. The antenna is fabricated on the FR-4 substrate with a thickness of 1.6 mm, an overall size of $32\ \text{mm} \times 30\ \text{mm}$, and electrical dimensions of $0.13\lambda_0 \times 0.122\lambda_0$, where λ_0 is the free space wavelength at 2.45 GHz. The resonant frequency of the designed antenna is 2.45 GHz. The antenna offers a gain of 1.68 dB and an efficiency of 85.3%. The presence of a crack in the bone is detected by observing the shift in the peak resonating frequency of the antenna. This method can detect bone fractures in a noninvasive manner. The human arm model is constructed, and the effect of bone cracks of different lengths on the resonating frequency is investigated. The pig bone and tissues are used to validate the simulated results. The simulated results are in agreement with the measured outcomes. Also, the specific absorption rate (SAR) of the antenna is calculated and found to be less than $0.57\ \text{W/kg}$. The designed monopole antenna has several advantages, including a small footprint, straightforward design, low cost, and easy integration with other devices. The proposed method is suitable for primary-level bone crack diagnosis.

1. Introduction

The importance of bones in the human body is well understood. They perform important functions such as mineral storage and providing mechanical strength to soft tissues and organs. A bone fracture can occur for a variety of reasons. Osteoporosis, caused by a lack of vitamin D, causes bone brittleness, which can lead to bone cracks. An accident also can cause fractures or defects in human bones. The tibia, also known as the shinbone, is the longest bone in the human body and is located in the lower part of the leg. There is a higher possibility for the occurrence of a tibia fracture. Tibia fractures are common in children, athletes, and the elderly, and they are difficult to detect at the outset [1]. The uncontrolled movement of a fractured part may aggravate the injury. Therefore, detecting bone fractures at

an early stage is expected as the restricted activity of the affected region can aid in the rapid healing of the fractured part. Techniques such as X-ray, ultrasound, computed tomography, and magnetic resonance imaging can be used to detect fracture. X-ray is the most commonly used method for detecting bone cracks. However, frequent exposure of the human body to X-rays may increase the risk of cancer. An ultrasound uses nonionized radiations to detect fractures, but the presence of speckles reduces image resolution, which affects diagnosis accuracy, and ultrasonic waves are highly attenuated by multiple layers of the human body. Computer tomography uses ionized radiation for diagnosis, which has the potential to cause cancer in pediatric patients. The magnetic resonance technique requires a complicated system, skilled technicians, and a high operating cost. However, due to high radiation levels, these

techniques are not suitable for children and pregnant women. Therefore, a more efficient, noninvasive, safe, and nonionized radiation method is required for detecting bone fractures [2].

Microwaves, unlike ultrasonic waves, can easily penetrate and are not attenuated by multiple layers of the human body having different dielectric constant values. This feature of microwaves attracts planar antennas for medical diagnosis. The International Telecommunication Union (ITU) has recommended that the frequency bands 401–406 MHz, 433.1–434.8 MHz, 608–614 MHz, 868–868.6 MHz, 902.8–928 MHz, 1.395–1.4 GHz, 1.427–1.432 GHz, and 2.45–2.5 GHz, popularly known as industrial, scientific, and medical (ISM) bands, can be used for medical implant communication services [3, 4]. Since the human body is made up of layers with different dielectric constants, an antenna resonating at lower frequencies will have a greater depth of penetration. However, antennas operating at lower frequencies may have larger dimensions [5]. Composite left/right-handed materials have been used in the design of sensing antennas due to their unique properties such as uniform group velocity, zero attenuation, and constant phase [6–8]. Several techniques, such as high-permittivity substrates and reactive elements, have also been used to design compact diagnostic/sensing antennas. In [9], a metamaterial-based antenna array was used for detecting tumors in breast tissues. In this method, the antennas were placed around the breast model, with one antenna acting as a transmitter at a time and the other antennas acting as receivers. The receiver antennas adjacent to the transmitter antennas receive the signal reflected from the tissue surface, while the opposite-side antennas collect the signal that traveled through the breast tissue. In this manner, the magnitude and phase information of the scattered signal were captured, and this information was then used for the dielectric characterization of the breast tissues.

Once a bone crack has occurred, it is necessary to monitor the affected area on a regular basis to ensure quick restoration and healing. Fracture healing can be monitored by passing current through the implanted pins and recording the variation in impedance to determine the level of recovery. The impedance decreases when the bone fracture is restored after three to four weeks [10]. However, the disadvantage of this method is that the variation in impedance level is small, and making differentiation is a difficult task. In another technique [11], some of the electromagnetic properties of the bone, such as dielectric constant, inductance, and conductance, were used to monitor fracture healing. In this method, two monopoles were placed across the fractured part, and the amount of power received was measured. When the bone crack was large in size, the power received was initially low, but it gradually increases as the crack healed. Microwave imaging allows the noninvasive diagnosis of biological tissues while also being low in cost and risk of manipulation. The microwave tomographic system identifies variations in dielectric constants between tissue and bones, and the rapid localization of the dielectric frontier allows image construction of the bone structure [12]. The authors of [13] designed a microwave ring resonator for bone fracture detection, wherein the affected region was scanned and variations in

transmission characteristics were used to characterize the fracture. When the antenna/resonator is placed closer to the human body, some of its performance characteristics, such as resonant frequency, gain, and efficiency, slightly deviate from their actual values [14–16]. However, the absorption of electromagnetic radiation by the human body is a major concern, and if it exceeds certain limits, it may cause health issues [17]. In biomedical applications, an antenna can be used as an implantable or on-body device to detect disease or abnormalities in organs. An implantable antenna should be biocompatible and small in size [18]. Several decades ago, implanted devices were powered, controlled, and monitored by external stations linked by wired connections, which could result in unavoidable surgical complications. Modern antenna technology significantly reduces the issue of surgical risk to human life [19]. A monopole antenna is an excellent candidate for detecting disease/abnormalities in the human body due to its straightforward design, simple fabrication on the dielectric substrate, small size, low cost, easy integration with other devices, and improved performance in multipath environments [20–23]. Also, the various performance metrics of the monopole antenna, such as impedance bandwidth, gain, and efficiency, can be easily controlled by altering the ground shape and adjusting the gap between the radiator and ground plane [24–26].

This study presents the design of a narrowband monopole antenna for bone fracture detection. The antenna prototype is tested on the pig bone, and the effect of different length bone cracks on the resonating frequency is investigated. This manuscript is divided into five sections. Section 1 discusses various causes of bone cracks, different methods of fracture detection, and their benefits and drawbacks. Section 2 describes the antenna design procedure and parametric specifications. Section 3 describes the structure of the human arm model, specific absorption rate (SAR), and antenna characteristics in different environments. Section 4 discusses the bone fracture detection process and the results obtained, and Section 5 provides the conclusion.

2. Antenna Design

The proposed monopole antenna is shown in Figure 1. The radiator and ground plane are printed on the front and back sides of the FR-4 material with a thickness of 1.6 mm, dielectric constant of 4.4, and loss tangent of 0.02. The antenna consists of a modified hexagon-shaped radiator with six triangular slits integrated on its bottom periphery, a rectangular-shaped ground plane, and a microstrip feed line of the width of 3.1 mm to match the $50\ \Omega$ impedance. The final structure of the antenna is obtained after four stages of evolution. The fabricated antenna prototype is shown in Figure 2. The physical size of the antenna is $32\ \text{mm} \times 30\ \text{mm}$, and its electrical dimensions are $0.13\lambda_0 \times 0.122\lambda_0$, where λ_0 is the free space wavelength at 2.45 GHz. The 3D EM simulator CST Microwave Studio[®] is used for simulating the antenna design.

The evolution of the proposed antenna is shown in Figure 3. A rectangle and a hexagon are combined to form a radiator in the first stage, as shown in Figure 3(a). The antenna is excited by a microstrip line, and a rectangular-

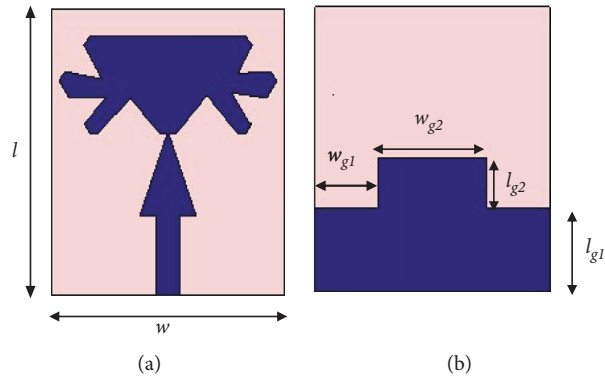


FIGURE 1: Proposed monopole antenna. (a) Front plane. (b) Back plane ($l = 32$ mm, $w = 30$ mm, $l_{g1} = 9.4$ mm, $l_{g2} = 5.6$ mm, $w_{g1} = 8$ mm, and $w_{g2} = 14$ mm).

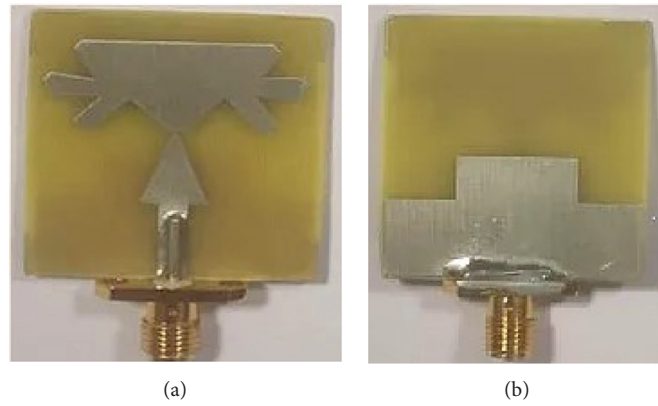


FIGURE 2: Fabricated antenna prototype. (a) Front view. (b) Rear view.

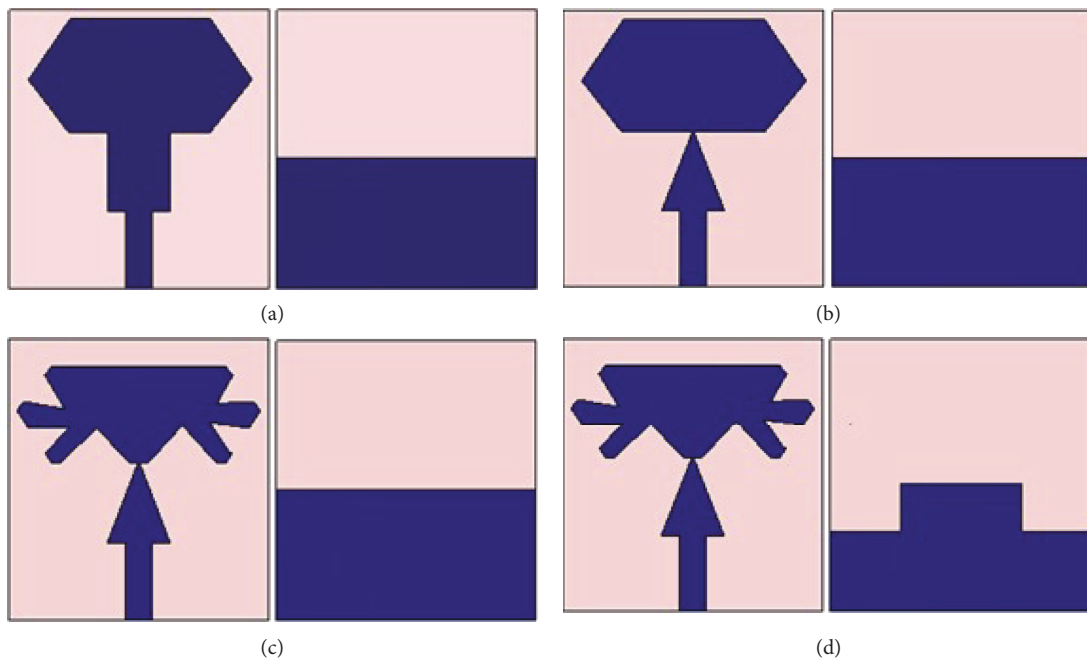


FIGURE 3: Evolution stages of the antenna. (a) Stage 1. (b) Stage 2. (c) Stage 3. (d) Stage 4.

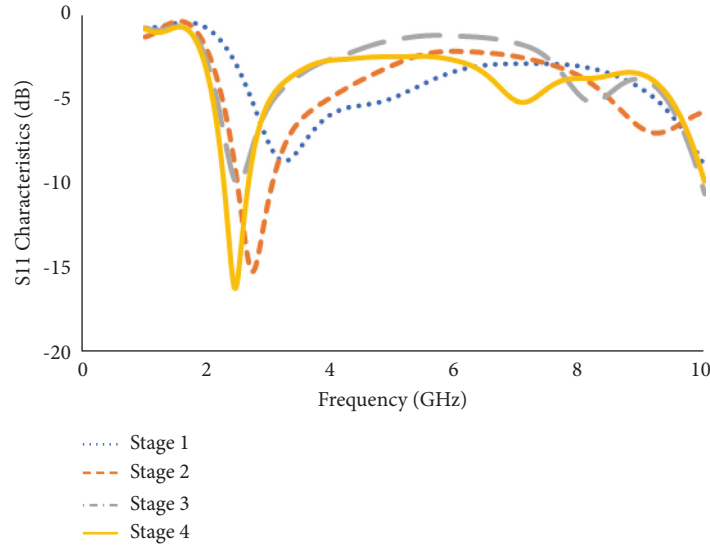


FIGURE 4: Reflection coefficient characteristics of the antenna stages.

shaped partial ground plane is designed on the backside of the substrate. In the first stage of evolution, the antenna shows a resonance at 3.24 GHz, but the impedance matching is poor at this frequency. The rectangular patch is then tapered in order to concentrate the charge carriers in a specific portion of the radiator, resulting in a resonant frequency shift to 2.74 GHz, as shown in Figure 3(b). In the third stage, six triangular slits are introduced in the bottom periphery of the radiator (shown in Figure 3(c)) to increase the length of the current path. In the next stage, rectangular slits are cut into the ground plane, reducing capacitive reactance, and allowing the antenna to resonate at 2.458 GHz with a reflection coefficient of -16.28 dB, as shown in Figure 3(d). Figure 4 depicts the reflection coefficient characteristics at various stages of evolution.

To understand the theoretical aspects of the antenna, the equivalent circuit model and surface current distribution are studied. Figure 5(a) depicts the electrical equivalent circuit of the designed antenna, and Figure 5(b) shows the real and imaginary impedance characteristics of the antenna. Both the real and imaginary curves move from high to low at 2.45 GHz resonant frequency resulting in a parallel combination of R, L, and C components in the circuit model.

The surface current distribution is depicted in Figure 6. It shows that the current density of 2.45 GHz is highly concentrated in the triangular slit region.

The E-plane and H-plane radiation patterns of the designed antenna are shown in Figures 7(a) and 7(b), respectively. The figure clearly shows that the antenna produces an omnidirectional radiation pattern at 2.45 GHz. The measured gain and radiation efficiency of the antenna are shown in Figure 8. The gain of the antenna is 1.68 dB, and its efficiency is 85.3%.

3. System Description

3.1. Human Arm Model. The human arm consists of four layers as shown in Figure 9. The bone is the innermost layer,

and the skin is the outermost layer. Muscle and fat are found between these two layers. Each layer has different relative permittivity, conductivity, and loss tangent values, which are listed in Table 1 [27].

3.2. SAR. Since the human body is made up of many layers with different conductive and dielectric properties, and when the antenna is operated closer to the human body, some of the radiated power is absorbed by the body, which may result in higher SAR [28–30].

The SAR is an important parameter that quantifies the amount of electromagnetic energy absorbed by body tissues. The standard unit for measuring SAR is W/kg.

$$\text{SAR} = \frac{\sigma |E|^2}{\rho} \text{ W/kg}, \quad (1)$$

where E is the root mean square of the electric field (V/m), σ is the conductivity (S/m), and ρ is the mass density of the tissue (kg/m^3).

According to the FCC guidelines, the SAR should be less than 1.6 W/Kg, and the simulated SAR value for the designed antenna is <0.812 W/Kg. The SAR of the proposed monopole antenna is depicted in Figure 10.

In order to measure the SAR, microwave signals with 1 mW power are applied to the antenna, and the thermogram readings are taken before and after (20 minutes) excitation.

$$\text{SAR} = \frac{\Delta T}{\Delta t} C_t \text{ W/kg}, \quad (2)$$

where ΔT is the rise in the temperature ($^{\circ}\text{C}$), Δt is the time duration for which microwave signals are applied (second), and C_t is the heat capacity ($\text{J/kg}^{\circ}\text{C}$) of different parts, such as skin, fat, muscle, and bone.

The temperature rose from 34.1°C to 34.3°C after 1,200 seconds of excitation, and the increase in temperature by

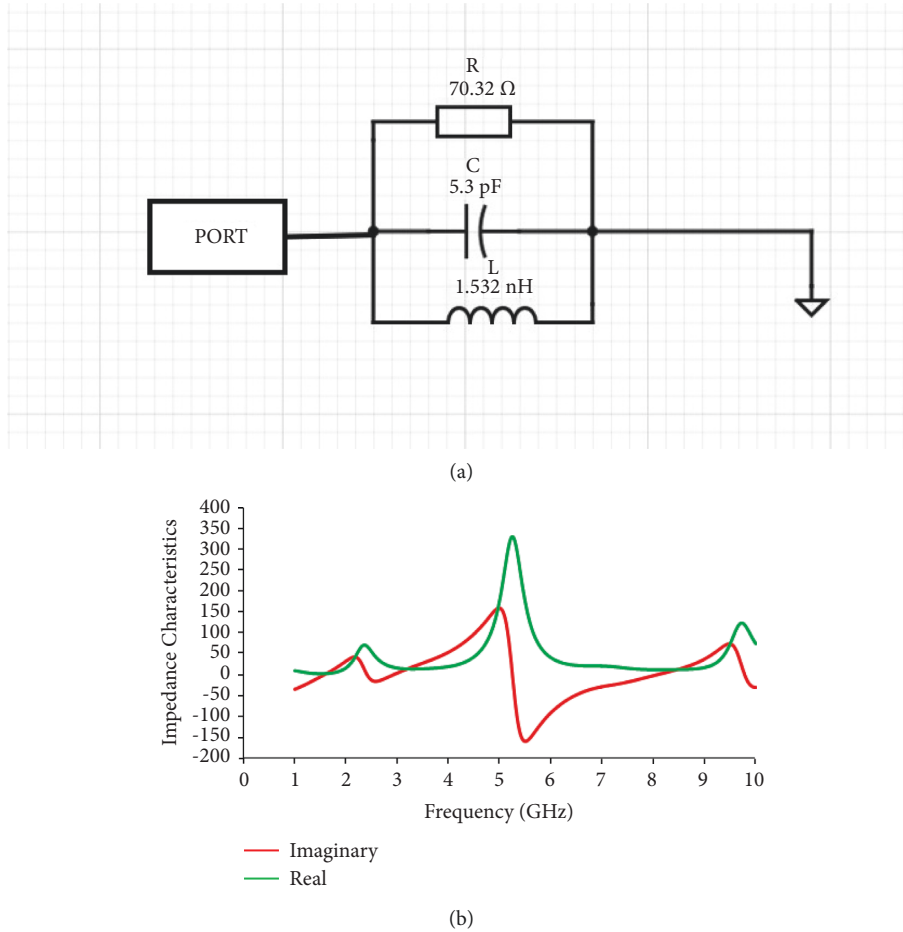


FIGURE 5: Equivalent circuit study. (a) Circuit model. (b) Real and imaginary characteristics.

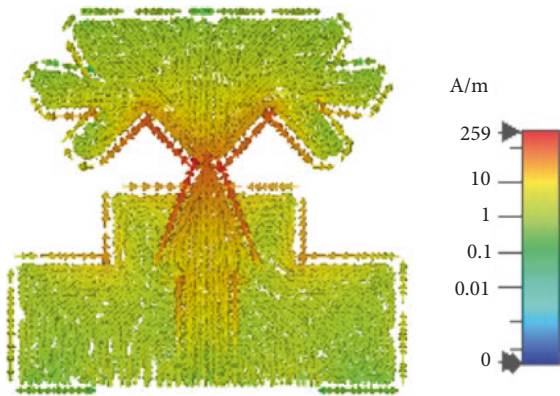


FIGURE 6: Surface current distribution of the antenna at 2.45 GHz.

0.2°C remained the same for a long duration of time. Then, the SAR of the antenna is calculated, using expression (2), as 0.57 W/kg.

3.3. *Antenna Characteristics along with the Arm Model.* When the antenna is simulated in free space, the peak resonance is noticed at 2.458 GHz. If the same antenna is placed on the arm model that does not have a crack, the

resonant frequency shifts to the lower side at 2.124 GHz [31], as shown in Figure 11.

4. Bone Fracture Detection

The antenna is placed on the arm model to detect bone cracks. Cracks of varying lengths are induced in the bone model, and the changes in the reflection coefficient characteristics of the antenna are noted. The length of the bone crack is determined by the amount of shift of the resonating band.

The dielectric properties, such as permittivity (ϵ_r) and permeability (μ_r), play an important role in the material characterization. The dielectric properties of a material can be influenced by factors such as density, structure deformation, water content, and porosity. The speed of propagation of an electromagnetic wave is determined by the permittivity of the medium through which it travels and interacts with the material in three ways: absorption, reflection, and transmission. The amount of reflection depends on the permittivity of the material and the frequency of the propagating microwave signal.

In the presented work, the electromagnetic radiations are used to characterize the dielectric properties of the bone structure without causing any destruction. The obtained

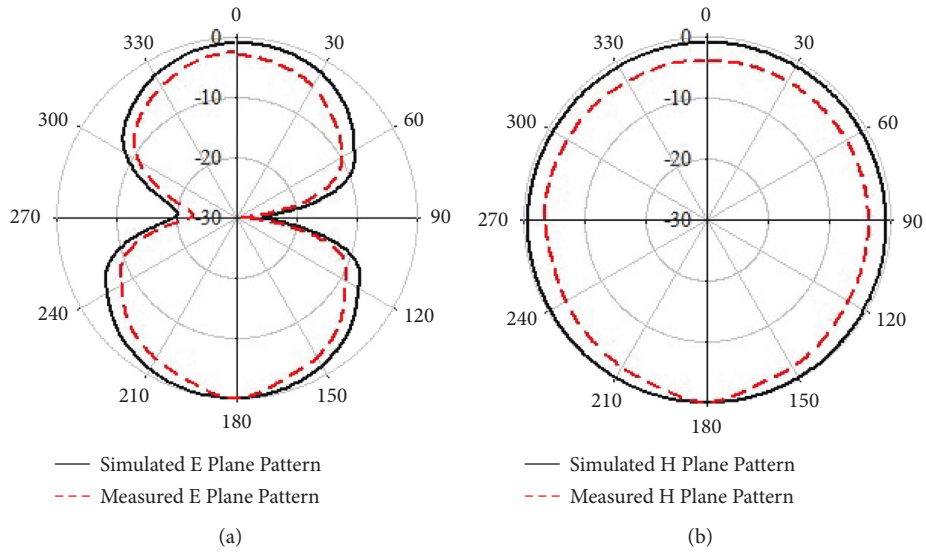


FIGURE 7: Radiation patterns at 2.45 GHz. (a) E-plane. (b) H-plane.

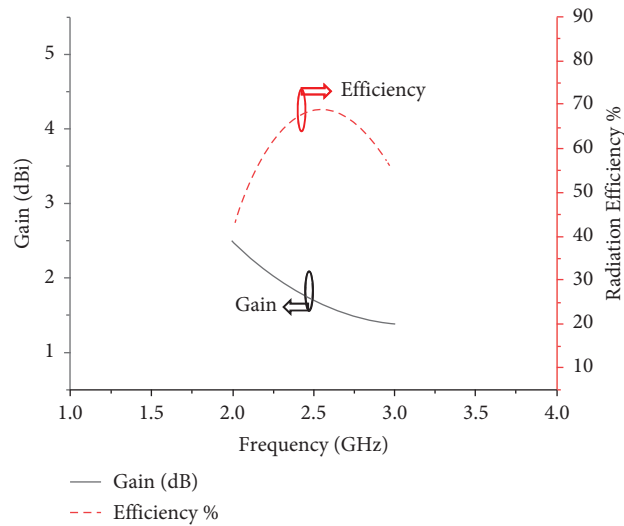


FIGURE 8: Measured gain and efficiency of the proposed antenna.

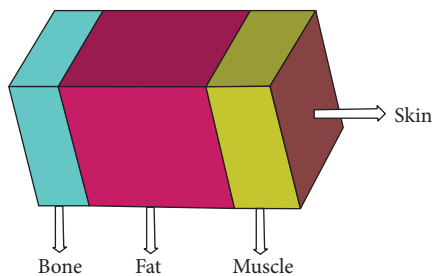


FIGURE 9: Human arm model.

reflection coefficients are analyzed to detect changes in the bone profile. There is a difference in the peak value of the reflection coefficients between the bone with and without a crack. The amount of frequency deviation is proportional to the crack's dimension. This is due to the fact that if a crack

exists, the permittivity of the bone changes, affecting the reflection coefficient characteristics.

$$\Gamma = \frac{Z_L - Z_0}{Z_L + Z_0} = \frac{\sqrt{(\mu_r/\epsilon_r)} - 1}{\sqrt{(\mu_r/\epsilon_r)} + 1}, \quad (3)$$

where

$$Z_L = \exp(j\omega\sqrt{(\mu_r\epsilon_r)}d). \quad (4)$$

When the antenna is placed over the arm model without a bone crack, the reflections of the radiations are only due to bone having relative permittivity of 12.66. If a crack is present in the bone (i.e., air is the medium in the crack), the S_{11} characteristics are determined by the effective dielectric constant of the bone and the air gap.

TABLE 1: Characteristics of various layers of human arm.

Layer	Thickness (mm)	Relative permittivity (mm)	Loss tangent	Density (kg/m ³)
Skin	0.4	41.4	0.418	1100
Fat	30	5.46	0.186	1100
Muscle	69.6	55	0.342	1040
Bone	13	18.49	0.214	1008

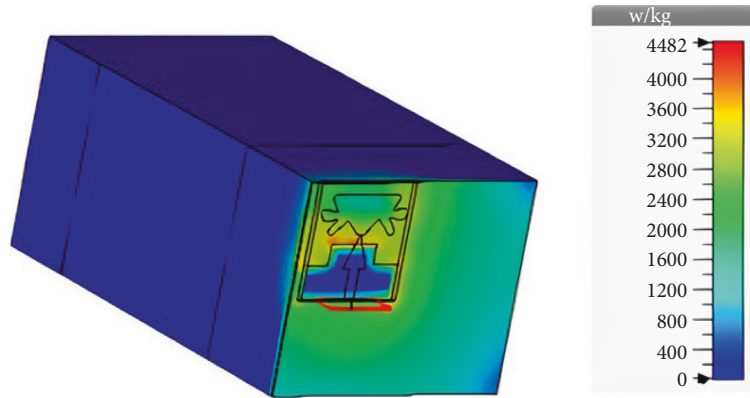


FIGURE 10: SAR analysis.

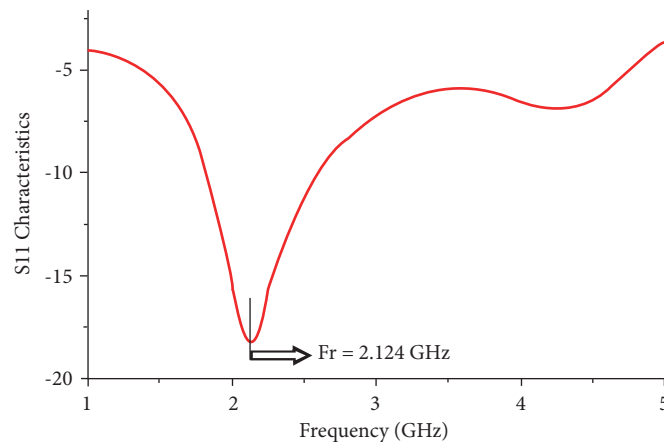


FIGURE 11: Reflection coefficients when the antenna is placed closer to the human arm.

For a crack length of 2 mm, the antenna shows a resonant peak at 2.132 GHz. The resonant frequency moves to the higher side as the bone crack length increases, and for a crack length of 10 mm, the resonance shifts to 2.16 GHz, as shown in Figure 12. This is due to the fact that when a crack is present, the radiation from the antenna is reflected by two mediums with different dielectric constants (12.66 and 1). The resonant frequencies for different fracture lengths are presented in Table 2.

The antenna is fabricated, and its reflection coefficients are measured using VNA. When used in free space, the antenna shows the peak resonance at 2.45 GHz, and when positioned closer to the human arm, as shown in Figures 13 and 14, the resonance is achieved at 2.122 GHz.

Also, a portion of pig bone and tissue was used to validate the simulated results. Fractures of varying lengths were induced, the fabricated antenna was placed over the pig bone (Figure 15), and the corresponding changes in the

reflection coefficients are shown in Figure 16. The measurements show that the experimental values are consistent with the simulated values for different fracture lengths.

Pig bone and tissues were chosen for the bone crack detection process due to their similarities to human bone and tissues. The antenna ground plane is placed on the skin, and the resonance frequency is measured using the VNA. Without a bone crack, the antenna produces resonance at 2.122 GHz, which is nearly identical to the simulated resonance at 2.124 GHz. Then, in the pig bone, fractures of various lengths such as 10 mm, 20 mm, and 30 mm were induced, and the change in the reflection coefficient characteristics was examined, as shown in Figure 17. The difference between the obtained frequency (f_n) and no crack frequency (f_c) is calculated, as shown in Table 3, and plotted on the x -axis (frequency difference (d_f), GHz) and crack/fracture length (mm) on the y -axis, as shown in Figure 18. The obtained

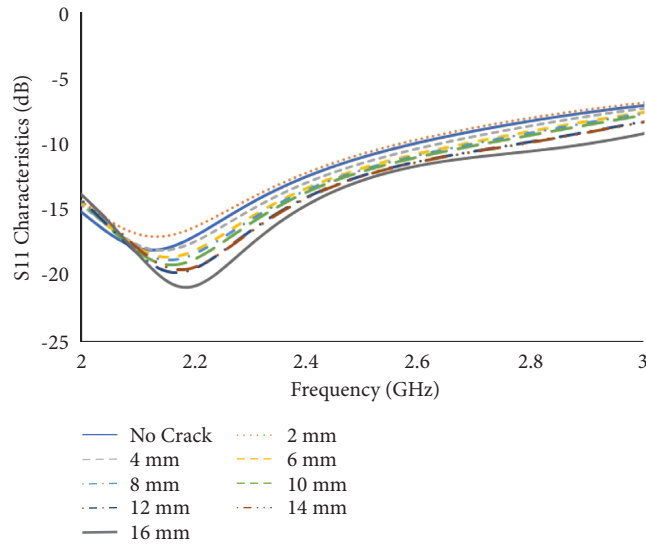


FIGURE 12: Resonant frequencies for different fracture lengths.

TABLE 2: Resonant frequencies for different fracture lengths.

Void size	Freq. (GHz)	Shift (in MHz)	Void size (in mm)	Freq. (GHz)	Shift (in MHz)
0	2.124	—	—	—	—
2	2.132	8	10	2.16	36
4	2.144	20	12	2.168	44
6	2.152	28	14	2.176	52
8	2.156	32	16	2.184	60



FIGURE 13: Measurement setup using a VNA.

frequency deviation is 0.03 GHz or 30 MHz, which is good enough to differentiate crack lengths. Also, a linear relationship is established between fracture length (mm) and frequency deviation (GHz), as shown in equation (5).

$$\text{Fracture length} = 278.2 \times (d_f) - 0.64, \quad (5)$$

where d_f is the difference in frequency.

The presented work is compared to recently published work in Table 4, and the highlights and advantages of the proposed antenna system are as follows:

- (i) The conventional fracture diagnosis methods, such as X-ray, ultrasound, computed tomography, and magnetic resonance imaging, use ionized radiations, which may pose health risks to humans. In this work, an



FIGURE 14: On-body testing of the antenna.

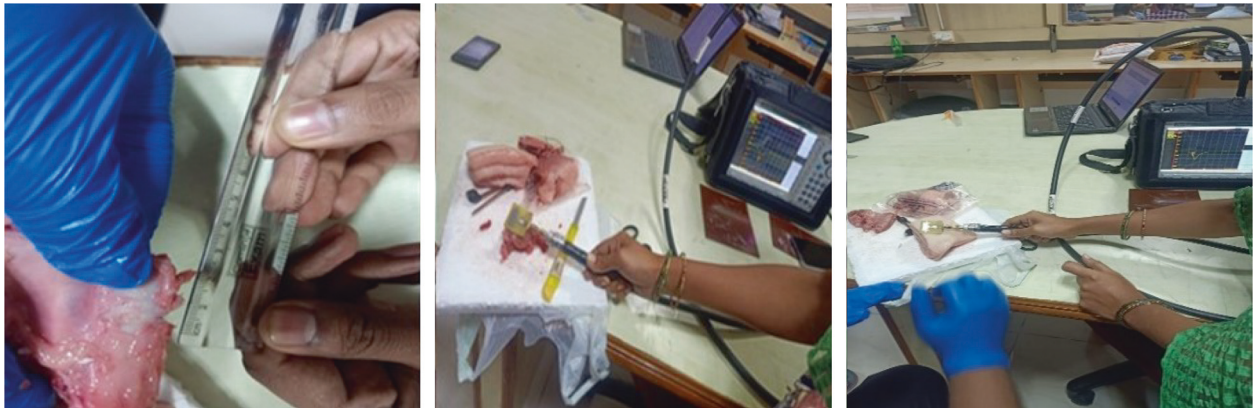


FIGURE 15: Measurement of S11 parameters on pig bone.

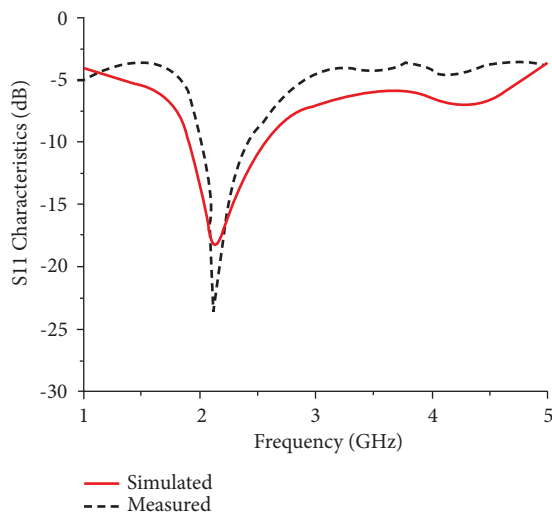


FIGURE 16: Reflection coefficient of the antenna on pig bone.

efficient, noninvasive, safe, and nonionized radiation method is proposed for detecting bone fractures.

- (ii) A planar monopole antenna operating at the ISM band is designed for bone crack detection. Microwaves, unlike ultrasonic waves, can easily penetrate and are not attenuated by the multiple layers of the human body with different dielectric constant values. This method noninvasively detects bone fractures and does not require any additional circuitry to process the data.

The antenna prototype is tested on the pig bone, and the effect of different length bone cracks on the resonating frequency is investigated. A linear relationship is found between crack length (mm) and frequency deviation (GHz).

- (iii) When designing the antenna, care has been taken to keep the SAR below 1.6 W/kg, as the antenna is operating in close proximity to the human body. Microwaves may be absorbed by human tissues, and microwave absorption above a certain threshold may pose health risks.
- (iv) A compact planar monopole antenna, with a size of 32 mm × 30 mm, is designed to radiate at 2.45 GHz for bone crack detection.
- (v) The proposed bone crack detection method does not require any additional processing units.
- (vi) Fresh pig bone (rather than the human bone) was used to validate the simulated results, whereas in other works, the authors did not validate the simulated results or use artificial bone models or old human bones for measurements.
- (vii) Since the antenna is operating in close proximity to the human body, microwaves may be absorbed by human tissues, and microwave absorption above a certain threshold may pose health risks. When designing the antenna, care has been taken to keep the SAR below 0.57 W/kg.

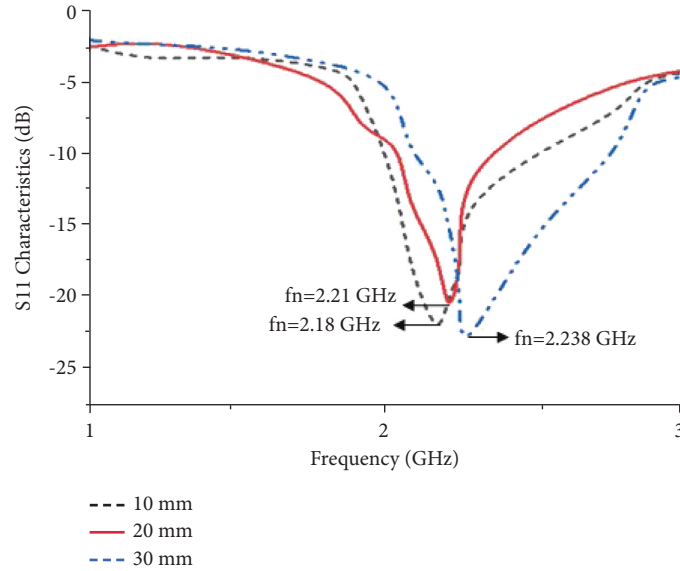


FIGURE 17: Measured reflection coefficients for different fracture lengths.

TABLE 3: Details of the frequency difference/shift.

Crack length (mm)	Peak resonance (GHz) (f_n , where $n = 1, 2, 3, 4$)	Frequency difference (GHz) ($d_f = f_n - f_c$)
No crack	$2.122 = f_c$	—
10	2.18	0.058
20	2.21	0.088
30	2.238	0.166

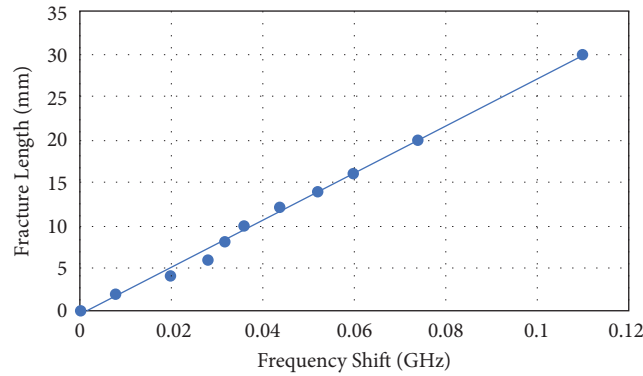


FIGURE 18: Variation of frequency shift with the fracture length.

TABLE 4: Comparison of the reported antenna designs with the proposed antenna.

Parameters	[8]	[9]	[10]	[11]	Proposed
Antenna type	Implantable monopole	Antipodal vivaldi	Microwave ring resonator	Microstrip patch	Planar monopole
Operating frequency (GHz)	1 to 4	0.5 to 4	2.45	2.45	2.45
Dimensions (mm × mm), ($\lambda_0 \times \lambda_0$)	$60 \times 55, 0.2 \times 0.18$	$100 \times 50, 0.167 \times 0.083$	$80 \times 114, 0.25 \times 0.45$	$48.7 \times 55.9, 0.2 \times 0.22$	$32 \times 30, 0.128 \times 0.12$
Sensitivity	Moderate	Moderate	High	Low	Moderate
SAR (W/kg)	—	—	<1.6	—	<0.812
Experimental validation done	Yes	Yes	Yes	No	Yes
Requirement of an additional processing unit	No	Yes	Yes	No	No

The proposed monopole antenna can be an excellent candidate for detecting bone cracks due to its straightforward fabrication on the dielectric substrate, small size, low cost, ease of integration with other devices, improved performance in multipath environments, and ease of operation as special skills are not required to use such device.

5. Conclusions

A planar monopole antenna is designed and developed for bone crack detection applications. The proposed antenna produces an omnidirectional radiation pattern with a gain of 1.68 dB and an efficiency of 85.3%. The EM simulator CST Microwave Studio[®] is used to simulate the human arm model, with fractures of varying lengths introduced. The designed antenna is scanned over the arm model, and the changes in the reflection coefficient characteristics are examined. The pig bone is used for the measurement, with cracks of varying lengths introduced and variations in the reflection coefficients investigated. The measured values agree well with the simulated results. It is observed that the resonant frequency of the antenna shifts to the higher side as the crack length increases. As the crack length increases from 10 mm to 30 mm, the corresponding resonance frequency shifts from 2.18 GHz to 2.38 GHz. Therefore, the frequency deviation is used to quantify the length of the fracture. Also, a linear expression is obtained for measuring the crack length as a function of frequency deviation. The SAR value of the proposed antenna is less than 0.57 kg/W. The presented method could be a low-cost RF solution for bone fracture detection.

Data Availability

Data are available on request.

Conflicts of Interest

The authors declare that there are no conflicts of interest regarding the publication of this paper.

References

- [1] J. Kenwright, J. Richardson, J. Cunningham et al., "Axial movement and tibial fractures. A controlled randomised trial of treatment," *Journal of Bone & Joint Surgery, British Volume*, vol. 73-B, no. 4, pp. 654–659, 1991.
- [2] Y. Bishitz, N. Ozana, Y. Beiderman et al., "Noncontact optical sensor for bone fracture diagnostics," *Biomedical Optics Express*, vol. 6, no. 3, pp. 651–657, 2015.
- [3] A. W. Damaj, H. M. El Misilmani, and S. A. Chahine, "Implantable antennas for biomedical application, an overview on alternative antenna design methods and challenges," in *Proceedings of the International Conference on High Performance Computing & Simulation (HPCS)*, pp. 31–37, Orleans, France, July 2018.
- [4] E. Avila-Navarro and C. Reig, "Directive microstrip antennas for specific Below-2.45 GHz applications," *International Journal of Antennas and Propagation*, vol. 2012, Article ID 612170, 6 pages, 2012.
- [5] S. Symeonidis, W. G. Whittow, C. Panagamuwa, and M. Zecca, "An implanted antenna system for the monitoring of the healing of bone fractures," in *Proceedings of the Loughborough Antennas & Propagation Conference (LAPC)*, pp. 1–4, Loughborough, UK, November 2015.
- [6] M. Alibakhshikenari, B. S. Virdee, A. Ali, and E. Limiti, "Extended aperture miniature antenna based on CRLH metamaterials for wireless communication systems operating over UHF to C-band," *Radio Science*, vol. 53, no. 2, pp. 154–165, 2018.
- [7] M. A. Kenari, "Printed planar patch antennas based on metamaterial," *International Journal of Electronics Letters*, vol. 2, no. 1, pp. 37–42, 2014.
- [8] M. Alibakhshikenari, B. S. Virdee, A. Ali, and E. Limiti, "A novel monofilar-Archimedean metamaterial inspired leaky-wave antenna for scanning application for passive radar systems," *Microwave and Optical Technology Letters*, vol. 60, no. 8, pp. 2055–2060, 2018.
- [9] M. Alibakhshikenari, B. S. Virdee, P. Shukla et al., "Metamaterial-Inspired antenna array for application in microwave breast imaging systems for tumor detection," *IEEE Access*, vol. 8, Article ID 174667, 2020.
- [10] M. C. Lin, D. Hu, M. Marmor, S. T. Herfat, C. S. Bahney, and M. M. Maharbiz, "Smart bone plates can monitor fracture healing," *Scientific Reports*, vol. 9, no. 1, pp. 2122–2215, 2019.
- [11] S. Symeonidis, W. G. Whittow, M. Zecca, and C. Panagamuwa, "Bone fracture monitoring using implanted antennas in the radius, tibia and phalange heterogeneous bone phantoms," *Biomedical Physics & Engineering Express*, vol. 4, no. 4, Article ID 45006, 2018.
- [12] G. Ruvio, A. Cuccaro, R. Solimene, A. Brancaccio, B. Basile, and M. J. Ammann, "Microwave bone imaging: a preliminary scanning system for proof-of-concept," *Healthcare Technology Letters*, vol. 3, no. 3, pp. 218–221, 2016.
- [13] V. S. Ramalingam, M. Kanagasabai, and E. F. Sundarsingh, "A compact microwave device for fracture diagnosis of the human tibia," *IEEE Transactions on Components, Packaging, and Manufacturing Technology*, vol. 9, no. 4, pp. 661–668, 2019.
- [14] G. M. Jagan, N. Arun Palanikumar, A. C. Varun Miranda, and S. Esther Florence, "Development of A Planar sensor for monitoring orthopaedic health," *International Journal of Advance Computational Engineering and Networking (IJACEN)*, vol. 4, no. 5, pp. 24–28, 2016.
- [15] V. S. Ramalingam, M. Kanagasabai, and E. F. Sundarsingh, "Detection of voids in fiber reinforced plastics using magnetoinductive coupled microstrip sensor," *IEEE Sensors Journal*, vol. 15, no. 8, pp. 4182–4183, 2015.
- [16] M. K. Sharma, M. Kumar, J. P. Saini, D. Kanaujia, S. P. Singh, and A. L. Ekuakille, "Experimental investigation of the breast phantom for tumor detection using ultra-wide band-MIMO antenna sensor (UMAS) probe," *IEEE Sensors Journal*, vol. 20, no. 12, pp. 6745–6752, 2020.
- [17] S. Kumari and V. R. Gupta, "Measurement of specific absorption rate of monopole patch antenna on human arm," *International Journal of Microwave and Optical Technology*, vol. 10, no. 3, 2015.
- [18] S. M. Abbas, Y. Ranga, and K. P. Esselle, "Reconfigurable antenna options for 2.45/5 GHz wireless body area networks in healthcare applications," in *Proceedings of the 2015 37th Annual International Conference of the IEEE Engineering in Medicine and Biology Society (EMBC)*, pp. 5465–5468, Milan, Italy, August 2015.
- [19] A. Gupta, A. Kansal, and P. Chawla, "A survey and classification on applications of antenna in health care domain: data

- transmission, diagnosis and treatment,” *Sādhana*, vol. 46, no. 2, pp. 68–17, 2021.
- [20] M. M. Soliman, M. E. H. Chowdhury, A. Khandakar et al., “Review on medical implantable Antenna technology and imminent research challenges,” *Sensors*, vol. 21, no. 9, pp. 3163–3228, 2021.
- [21] S. Ashok Kumar and T. Shanmuganantham, “Design of clover slot antenna for biomedical applications,” *Alexandria Engineering Journal*, vol. 56, no. 3, pp. 313–317, 2017.
- [22] M. Ahmed, C. H. See, I. M. Danjuma et al., “An active microwave sensor for near field imaging,” *IEEE Sensors Journal*, vol. 17, no. 9, pp. 2749–2757, 2017.
- [23] M. Alibakhshi-Kenari, M. Naser-Moghadasi, and R. Sadeghzadeh, “The resonating MTM-based miniaturized antennas for wide-band RF-microwave systems,” *Microwave and Optical Technology Letters*, vol. 57, no. 10, pp. 2339–2344, 2015.
- [24] S. Doddipalli, A. Kothari, and P. Peshwe, “A low profile ultrawide band monopole antenna for wearable applications,” *International Journal of Antennas and Propagation*, vol. 2017, Article ID 7362431, 9 pages, 2017.
- [25] M. A. Kenari and M. N. Moghadasi, “UWB miniature antenna based on the CRLH-TL with increase gain for electromagnetic requirements,” *Advanced Electromagnetics*, vol. 3, no. 1, pp. 61–65, 2014.
- [26] M. Alibakhshi-Kenari, M. Movahhedi, and H. Naderian, “A new miniature ultra wide band planar microstrip antenna based on the metamaterial transmission line,” in *Proceedings of the IEEE Asia-Pacific Conference on Applied Electromagnetics (APACE)*, pp. 293–297, Melaka, Malaysia, December 2012.
- [27] S. Bhattacharjee, S. Maity, S. K. Metya, and C. T. Bhunia, “Performance enhancement of implantable medical antenna using differential feed technique,” *Engineering Science and Technology, an International Journal*, vol. 19, no. 1, pp. 642–650, 2016.
- [28] U. Ali, S. Ullah, J. Khan et al., “Design and SAR analysis of wearable antenna on various parts of human body, using conventional and artificial ground planes,” *Journal of Electrical Engineering and Technology*, vol. 12, no. 1, pp. 317–328, 2017.
- [29] B. N. Balarami Reddy, P. Sandeep Kumar, T. Rama Rao, N. Tiwari, and M. Balachary, “Design and analysis of wide-band monopole antennas for flexible/wearable wireless device applications,” *Progress In Electromagnetics Research M*, vol. 62, pp. 167–174, 2017.
- [30] B. Sugumaran, R. Balasubramanian, and S. K. Palaniswamy, “Reduced specific absorption rate compact flexible monopole antenna system for smart wearable wireless communications,” *Engineering Science and Technology, an International Journal*, vol. 24, no. 3, pp. 682–693, 2021.
- [31] S. Shrestha, M. Agarwal, P. Ghane, and K. Varahramyan, “Flexible microstrip antenna for skin contact application,” *International Journal of Antennas and Propagation*, vol. 2012, Article ID 745426, 5 pages, 2012.

Research Article

Conformal Quad-Port UWB MIMO Antenna for Body-Worn Applications

Thennarasi Govindan,¹ Sandeep Kumar Palaniswamy¹,¹ Malathi Kanagasabai²,² Sachin Kumar³,¹ Thipparaju Rama Rao³,¹ and Mohammed Gulam Nabi Alsath³

¹Department of Electronics and Communication Engineering, SRM Institute of Science and Technology, Kattankulathur 603203, India

²Department of Electronics and Communication Engineering, College of Engineering, Guindy, Anna University, Chennai 600025, India

³Department of Electronics and Communication Engineering, SSN College of Engineering, Chennai 603110, India

Correspondence should be addressed to Sandeep Kumar Palaniswamy; vrpchs@gmail.com

Received 23 July 2021; Revised 23 November 2021; Accepted 1 December 2021; Published 30 December 2021

Academic Editor: Mourad Nedil

Copyright © 2021 Thennarasi Govindan et al. This is an open access article distributed under the Creative Commons Attribution License, which permits unrestricted use, distribution, and reproduction in any medium, provided the original work is properly cited.

A conformal four-port multiple-input-multiple-output (MIMO) antenna operating at 2.4 GHz and ultrawideband (UWB) is presented for wearable applications. The unit element of the MIMO antenna is a simple rectangular monopole with an impedance bandwidth of 8.9 GHz (3.1–12 GHz). In the monopole radiator, stubs are introduced to achieve 2.4 GHz resonance. Also, a defect is introduced in the ground plane to reduce backside radiation. The efficiency of the proposed antenna is greater than 95%, and its peak gain is 3.1 dBi. The MIMO antenna has an isolation of >20 dB, and the estimated specific absorption rate (SAR) values for 1 gm of tissue are below 1.6 W/Kg. The size of the four-port MIMO antenna is $1.38\lambda_0 \times 0.08\lambda_0 \times 0.014\lambda_0$.

1. Introduction

Wearable technology is one of the most popular research topics these days as it provides useful information about the fitness of a person. Wearable technology has been widely used in a variety of fields such as medicine, military, sports, and communication [1]. Body-worn devices such as fitness bands, smartwatches, smart jewellery, and smart helmets are commonly used for health monitoring. The antennas used in these smart devices operate at 2.45 GHz ISM band and ultrawideband (UWB) [2]. In [3], a male finger ring antenna was designed for healthcare applications. In [4], an UWB antenna was reported for the indoor positioning systems. Antennas used in wearable devices should be lightweight, flexible, and conformal [5]. In [6], a button-shaped wearable antenna was designed that can be attached to clothing. In [7], the multilayer weaving method was used to create a textile antenna made of conductive threads. UWB antennas integrated with the 2.45 GHz frequency band were reported in

[8, 9] to achieve a high data rate using small transmit power. A UWB multiple-input-multiple-output (MIMO) configuration was proposed to provide reliable data transmission while avoiding multipath fading. However, the mutual coupling is the main problem in MIMO antennas. The use of decoupling structures to reduce mutual coupling in a wideband vehicular antenna was described in [10]. Another important feature of wearable antennas is their close proximity to the human body. Therefore, specific absorption rate (SAR) analysis is performed to confirm that the radiation exposure is within the prescribed limit [11].

In this paper, a four-port MIMO/diversity wristband antenna is designed on a flexible and conformable silicone rubber substrate. The MIMO antenna consists of four antenna elements that are placed horizontally to provide pattern diversity. This paper is organized as follows. Section 2 describes the design of the proposed wearable antenna. Section 3 discusses the MIMO antenna results, diversity characteristics, and the SAR analysis. Section 4 presents the conclusion of the proposed work.

2. Antenna Design

2.1. UWB Antenna Element. The proposed antenna is a rectangular monopole with a defect in the ground plane as shown in Figures 1(a) and 1(b), respectively. The evolution of the proposed antenna is depicted in Figure 2. Figure 2(a) consists of a simple rectangular radiator and a modified ground plane. However, Antenna 1 has poor impedance matching, as illustrated in Figure 3. In the next step, rectangular slots are etched from the radiator on both sides of the feed line to improve impedance matching, as shown in Figure 2(b) (Antenna 2). In Figure 2(c) (Antenna 3), a U-shaped slot is incorporated into the ground plane to further improve the impedance matching. This step increased the impedance bandwidth significantly. Furthermore, a meander line stub and rectangular slot are introduced in the radiator and ground plane, respectively, to achieve an extra resonance at 2.4 GHz, as illustrated in Figure 2(d) (Antenna 4). Table 1 displays the design parameters of the proposed antenna.

For a better understanding, the surface current distribution of the proposed antenna element at 2.4 GHz, 3 GHz, 6 GHz, and 10 GHz is shown in Figure 4. It is observed that the UWB is controlled by the rectangular monopole radiator, while the 2.4 GHz resonance is controlled by the meander line stub and slotted ground plane. The antenna is designed on the silicone rubber substrate material of dielectric constant of 2.9 and loss tangent of 0.358 [12]. The substrate material has a perimeter of $1.38\lambda_0$, with a bending radius of 16.0825 mm readily available adult size silicone rubber wristband in the market. The proposed antenna operates in the (2.05–2.6 GHz) ISM band and the (3.1–12 GHz) UWB band. The size of the antenna element is $0.437\lambda_g \times 0.025\lambda_g$ mm², where λ_g is the guided wavelength.

The lower band-edge frequency (f_l) of the monopole planar antenna is determined using the following equation [13, 14]:

$$f_l = \frac{7.2}{(l + r + p) \times k}, \quad (1)$$

where l is the height of the antenna, r denotes the width of the monopole antenna, and $p = 0.2$ cm is the distance between the radiator and the ground plane.

$$k = \sqrt[4]{\epsilon_{eff}}. \quad (2)$$

The fourth root of the effective dielectric constant is the factor k .

Equation (1) is restructured for the proposed wristband antenna as follows:

$$f_l = \frac{7.2}{(1.92\pi[(a + b)] + p) \times k}. \quad (3)$$

The expression $(l + r)$ is related to $1.92\pi[(a + b)]$, which is equivalent to the perimeter of the monopole radiator. a and b correspond to the semiwidth and semilength of the radiator. The parameters a , b , l , r , and p are measured in centimetres, and f_l is measured in GHz.

The 2.45 GHz resonant frequency is obtained using a stub of length $\lambda_0/4 = L1 + L2 + L3 + \dots + L17$ as depicted in Figure 5.

The above equations are accompanied with the equivalent circuit as given in Figure 6.

Figure 6 shows the equivalent circuit of the proposed antenna, which is made up of R, L, and C components. The antenna impedance characteristics (Figure 7) show the series and parallel layout of the equivalent circuit. It is considered a series connection when the real and imaginary curves are from low to high, and a parallel connection if they move from high to low [15]. The values of the R, L, and C components are depicted in Figure 6. Since the impedance curves move from high to low at 2.4 GHz, they are shown in parallel, and the impedance curves go from low to high at 3.1 GHz (the start of the UWB) and 10.6 GHz (the end of the UWB), they are represented in series.

A parametric analysis of the radiator and ground plane is performed to achieve 2.4 GHz and UWB, as shown in Figures 8–11. The length of the stub “ o ” is varied to achieve the 2.4 GHz ISM band. When “ o ” is decreased to 0.4 mm, the reflection coefficient curve shifts to the left, and when “ o ” is greater than 0.5 mm, the reflection coefficient curve shifts to the right. Figure 6 depicts the effect of parameter “ f .” The reflection coefficient curves show that when “ f ” increases, the impedance matching improves, resulting in the UWB. Figure 10 depicts the effect of ground plane parameter “ q .” It is evident that as “ q ” increases, the resonance bandwidth increases due to improved impedance matching. Figure 11 depicts the reflection coefficients for various slot lengths “ r .” When $r = 1.5$ mm, the UWB is obtained, but no resonance occurs in the 2.4 GHz ISM band. Whereas at $r = 2.5$ mm, the 2.4 GHz ISM band is obtained, but the reflection coefficient curve shifts towards the higher frequency side. Therefore, the optimal width of the slot should be 2 mm.

2.2. MIMO Antenna. The proposed wristband MIMO antenna with and without ground plane is depicted in Figure 12. As [16], the investigations on connected ground plane are conducted, and the S-parameter results (Figure 13) show that there is no discernible effect on the performance of the proposed MIMO antenna due to the conformal nature of the prototype. The spacing between the antenna elements is $0.07\lambda_0$, which offers interelement isolation of >20 dB. A parametric analysis of the wristband antenna is performed by varying the bending radius. The bending radius of 16.0825 mm is chosen as adult size silicone rubber wristbands of this size are readily available in the market.

The parametric analysis is conducted by varying the bending radius, and the S-parameter curves are shown in Figures 14 and 15. Figure 14 demonstrates that the reflection coefficients for seven different bending radii do not vary significantly, and all of these curves covered the UWB and 2.4 GHz band. However, the spacing between the antenna elements may vary due to changes in the bending radius. The spacing is reduced to $0.0385\lambda_0$ for a bending radius of 14.5825 mm in Case 1 and increased to $0.105\lambda_0$ for a bending radius of 17.5825 mm in Case 2. It is observed that the interelement isolation increases with a larger bending radius and decreases with a smaller bending radius, shown in Figure 15. Further reduction of bending radius below

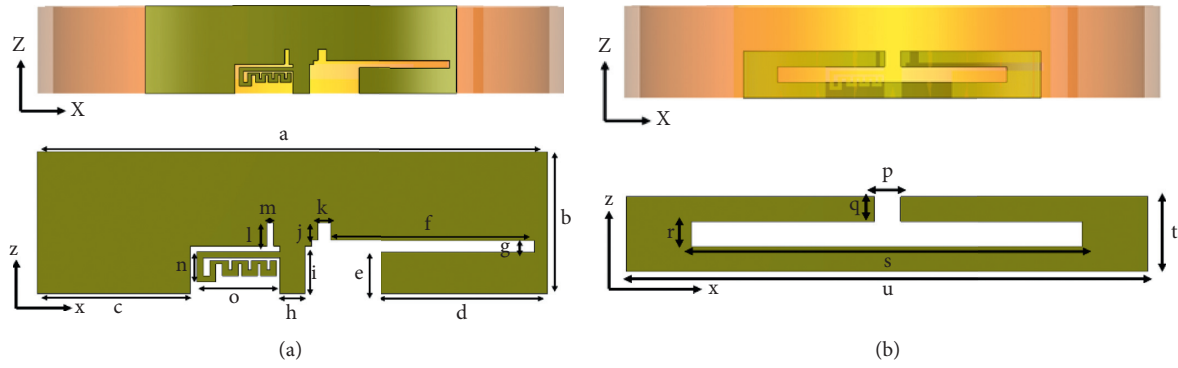


FIGURE 1: Proposed wristband antenna: (a) front view and (b) rear view.

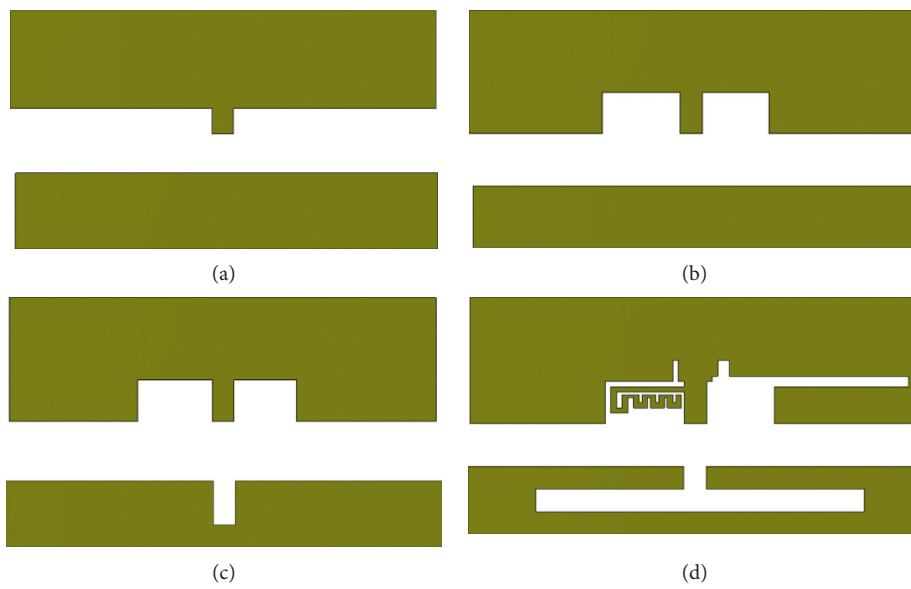


FIGURE 2: Evolution of the proposed antenna: (a) Antenna 1, (b) Antenna 2, (c) Antenna 3, and (d) Antenna 4.

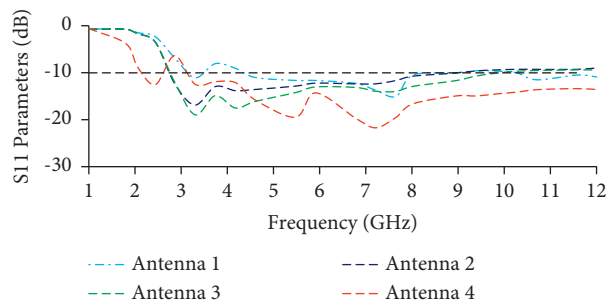


FIGURE 3: Reflection coefficients of the evolution stages.

TABLE 1: Dimensions of the wristband antenna.

Parameter	a	b	c	d	e	f	g	h	i	j	k
Value (mm)	40	12	12	13	3.5	16	1	2	4	1.5	1
Parameter	l	m	n	o	p	q	r	s	t	u	
Value (mm)	2	0.5	6.25	0.5	2	2	2	30	6	40	

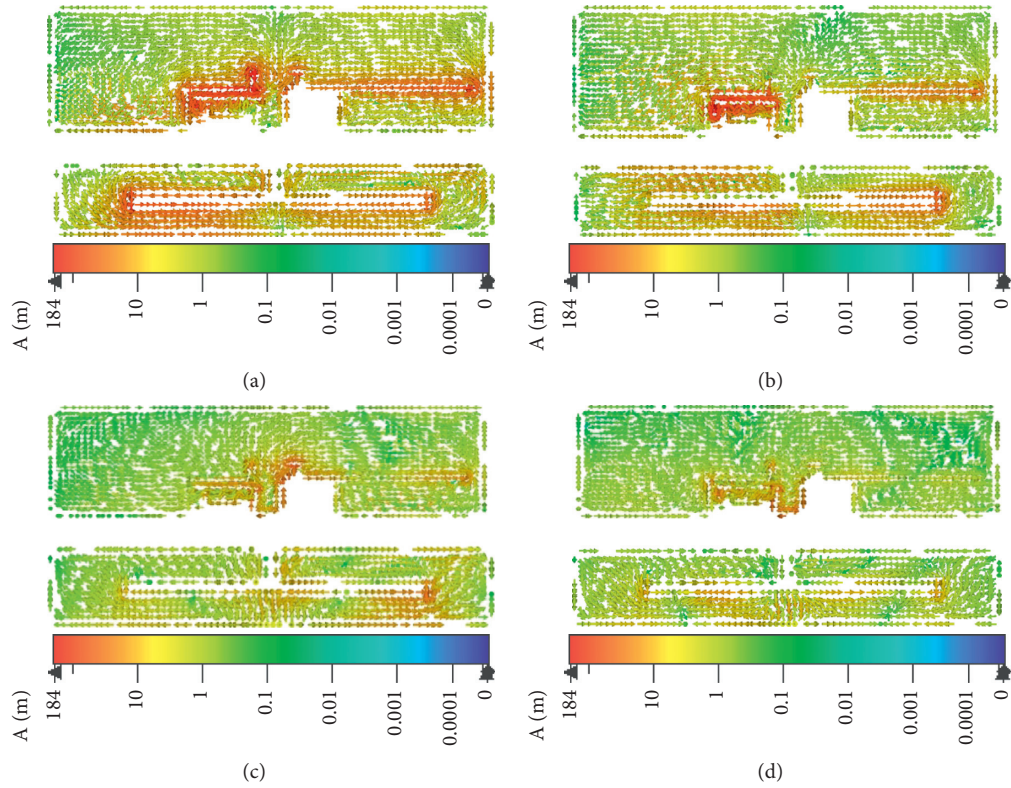


FIGURE 4: Surface current distribution at (a) 2.4 GHz, (b) 3 GHz, (c) 6 GHz, and (d) 10 GHz.

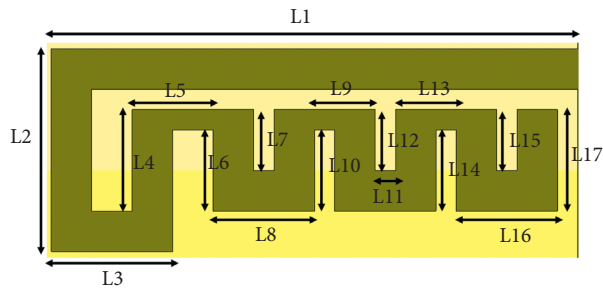


FIGURE 5: Stub of length $\lambda_0/4$ to achieve 2.45 GHz resonant frequency.

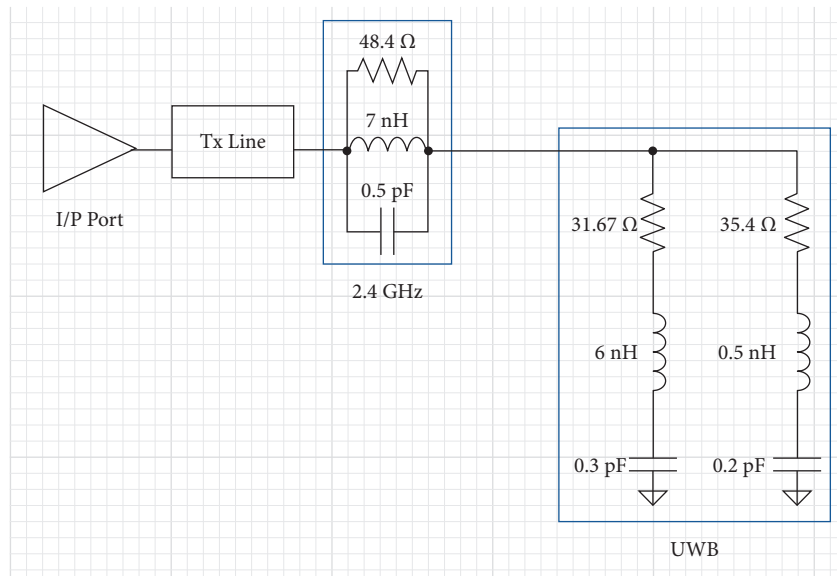


FIGURE 6: Equivalent circuit of the proposed wristband antenna.

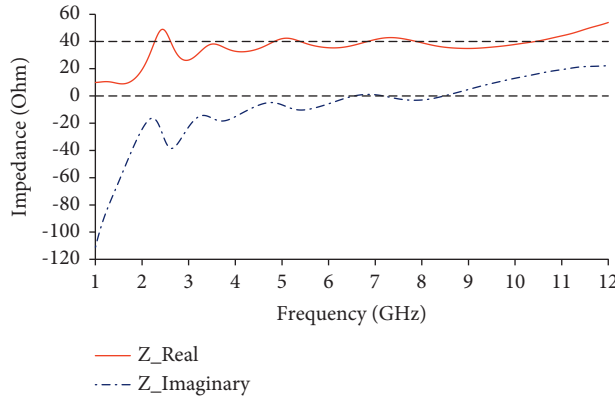


FIGURE 7: Impedance characteristics of the proposed wristband antenna.

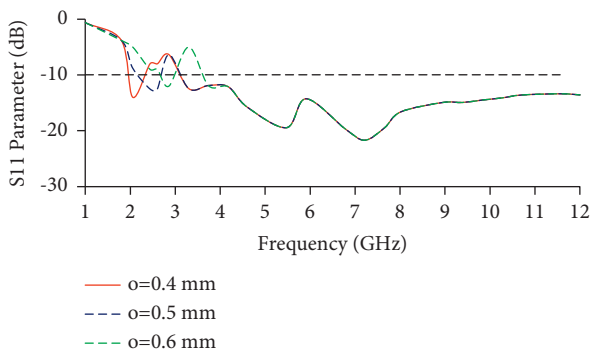


FIGURE 8: Reflection coefficients with varying lengths of stub “o.”

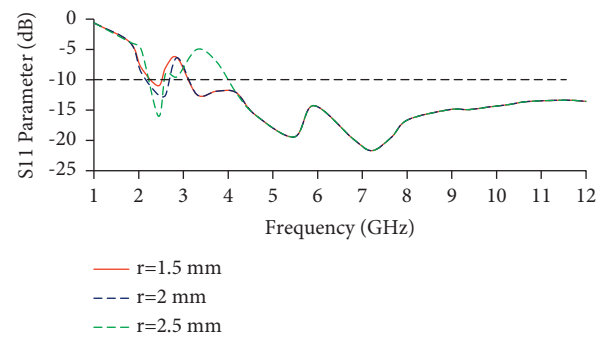


FIGURE 11: Reflection coefficients with varying lengths of slot “r.”

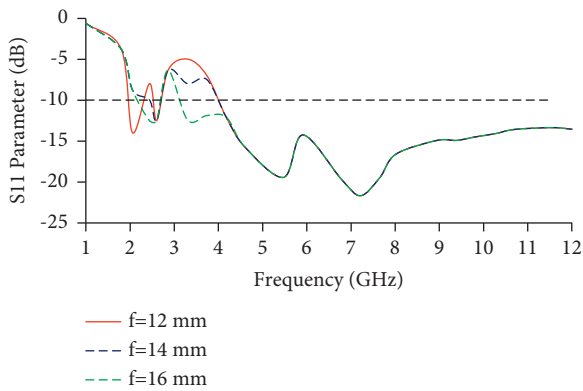


FIGURE 9: Reflection coefficients with varying lengths of “f.”

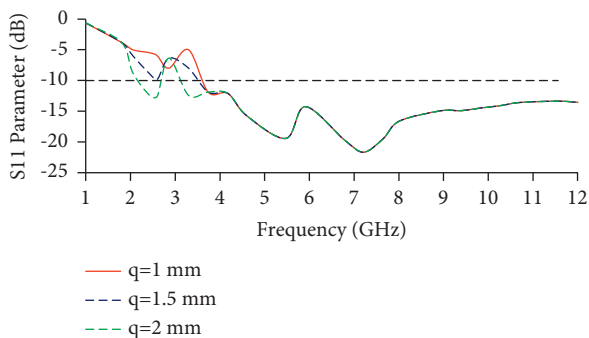


FIGURE 10: Reflection coefficients with varying lengths of slot “q.”

14.5825 mm increases the mutual coupling, which affects the antenna’s performance. There is no use of increasing the band size further as it will not match with the market available wristband. Therefore, band size with a bending radius of 16.0825 mm is considered in the proposed work.

3. Results and Discussion

3.1. S-Parameters. Figures 16(a)–16(c) show the fabricated prototype and its S-parameter measurement on the Anritsu MS 2037C vector network analyzer. The simulated and measured S-parameters of the MIMO antenna are given in Figures 17 and 18. The antenna exhibits an impedance bandwidth of 2.05–2.6 GHz in the ISM band and 3.1–12 GHz in the UWB. The reflection coefficient curves for Antenna 1, Antenna 2, Antenna 3, and Antenna 4 are all similar; therefore, S_{11} is only shown at port-1 for brevity. Figure 18 shows the mutual coupling between the antenna elements, which is greater than 20 dB.

3.2. Radiation Performance. The proposed antenna is tested in an anechoic chamber with a horn antenna as the standard reference antenna. The anechoic chamber measurement setup is shown in Figure 19. Figure 20 depicts the radiation patterns obtained in free space and on the human wrist at 2.4 GHz, 3 GHz, 6 GHz, and 10 GHz. The radiation patterns on the human wrist show suppressed back radiations.

The gain and efficiency plots of the proposed antenna are shown in Figure 21. The simulated and measured peak gain

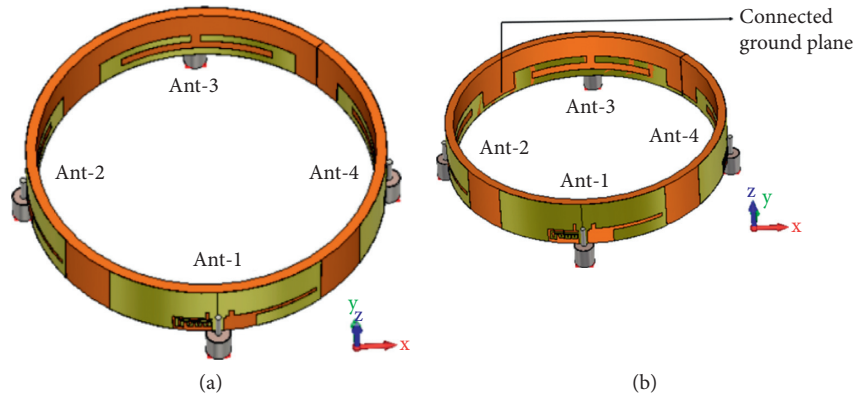


FIGURE 12: Prototype of the wristband antenna (a) without common ground plane and (b) with common ground plane.

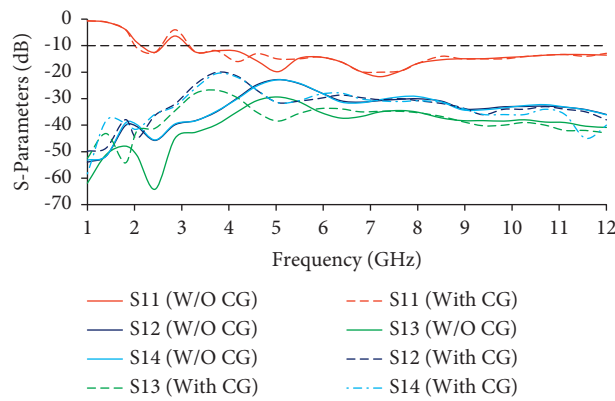


FIGURE 13: Simulated S-parameters of the proposed wristband antenna (with and without CG (common ground) plane).

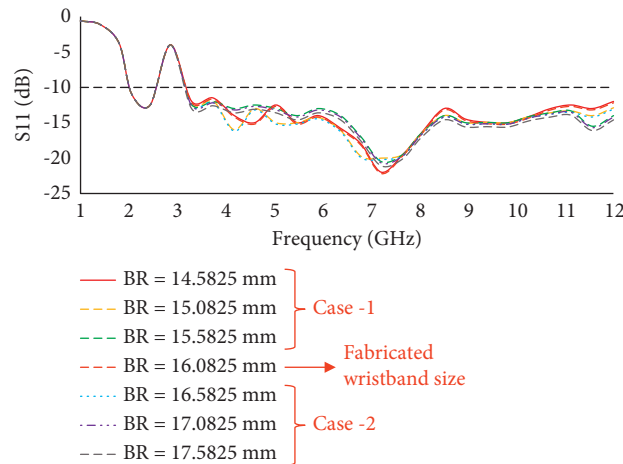


FIGURE 14: Reflection coefficients of the proposed wristband antenna at different bending radii (BR).

values are 4.7 dBi and 3.1 dBi, respectively. The difference between simulated and measured gain values is due to the manual fabrication process, cable effect, and SMA connector soldering [17, 18]. It may also be due to conductive adhesives used during fabrication and the tapes during anechoic chamber measurements. Other losses, such as conductor, dielectric, surface radiation, and power leakage from the connector, are also present in the measurements, which were

almost negligible in the simulated results. The efficiency of the wristband antenna is greater than 95%.

3.3. *Diversity Performance.* Envelope correlation coefficient (ECC) is used to calculate the correlation between antenna elements. It can be calculated using far-field as follows [19]:

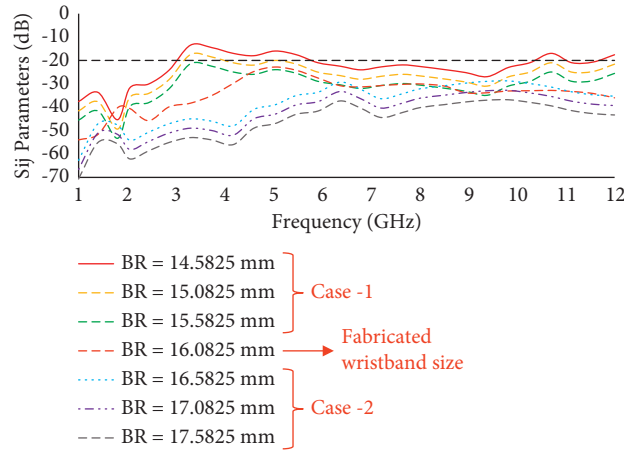


FIGURE 15: Mutual coupling of the proposed wristband antenna at different bending radii (BR).

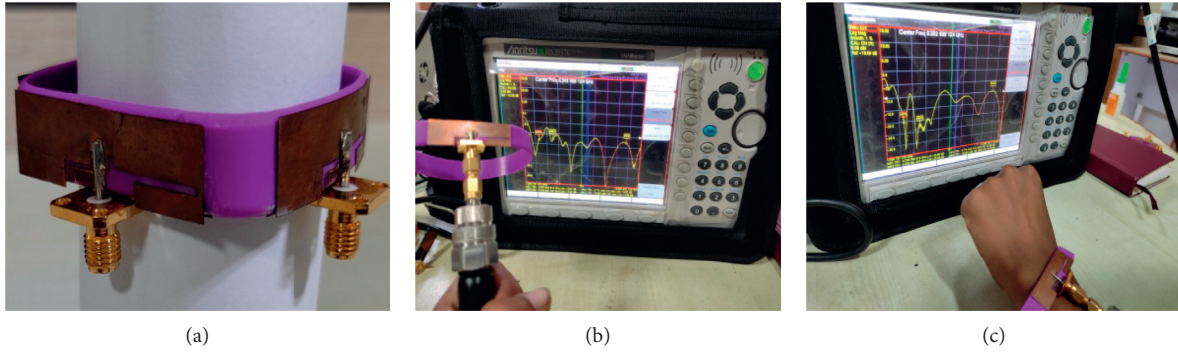


FIGURE 16: (a) Photograph of the fabricated prototype, (b) antenna measurement in free space, and (c) antenna measurement on the human wrist.

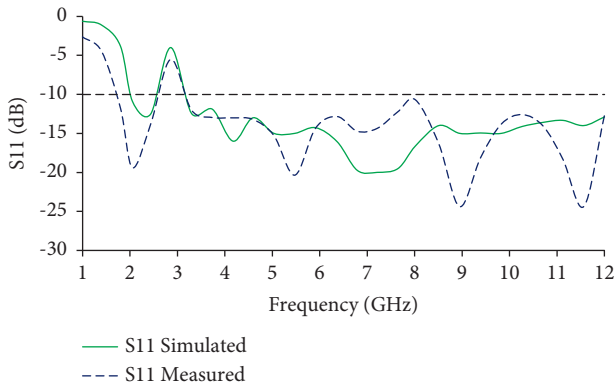


FIGURE 17: Simulated and measured S_{11} of the proposed wristband antenna.

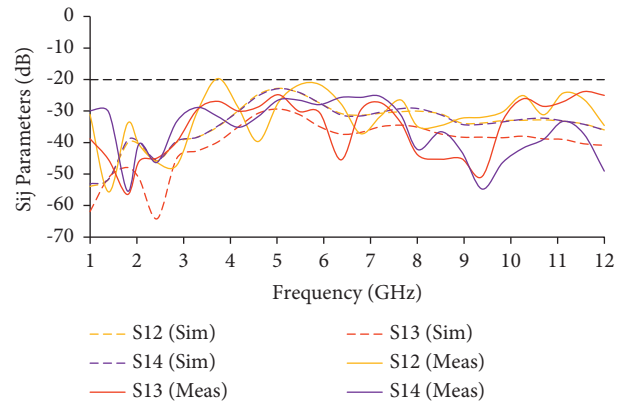


FIGURE 18: Simulated and measured S_{ij} -parameters of the proposed wristband antenna.

$$ECC = \frac{\left| \iint \left[\vec{F}_1(\theta, \varphi) \cdot \vec{F}_2(\theta, \varphi) \right] d\Omega \right|^2}{\iint \left| \vec{F}_1(\theta, \varphi) \right|^2 d\Omega \iint \left| \vec{F}_2(\theta, \varphi) \right|^2 d\Omega} \quad (4)$$

The ECC of the antenna is shown in Figure 22, and the obtained ECC values are <0.1 . Diversity gain (DG) refers to the process of transmitting a signal with the minimum loss. It is obtained by using (5). The DG plots are shown in

Figure 23, and the DG of the proposed antenna is greater than 9.4 dB.

$$DG = \sqrt{1 - |ECC|^2} \quad (5)$$

Channel capacity loss (CCL) is a measure of channel loss in a MIMO system. CCL is calculated using the following equation [20]:

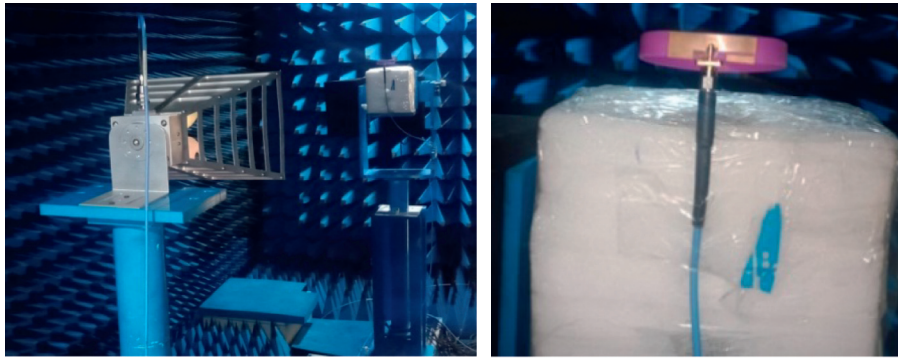


FIGURE 19: Anechoic chamber measurement of the proposed wristband antenna.

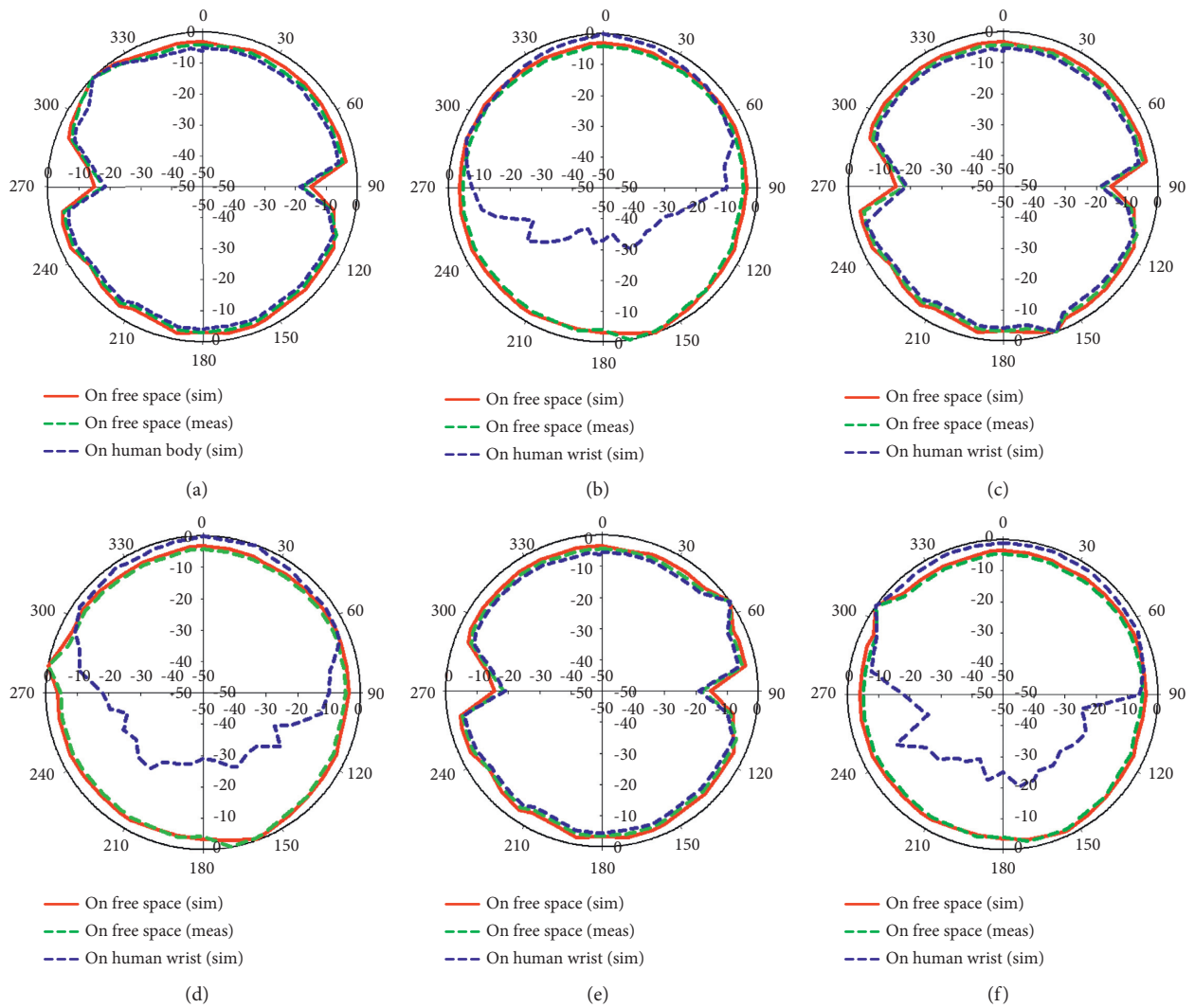


FIGURE 20: Continued.

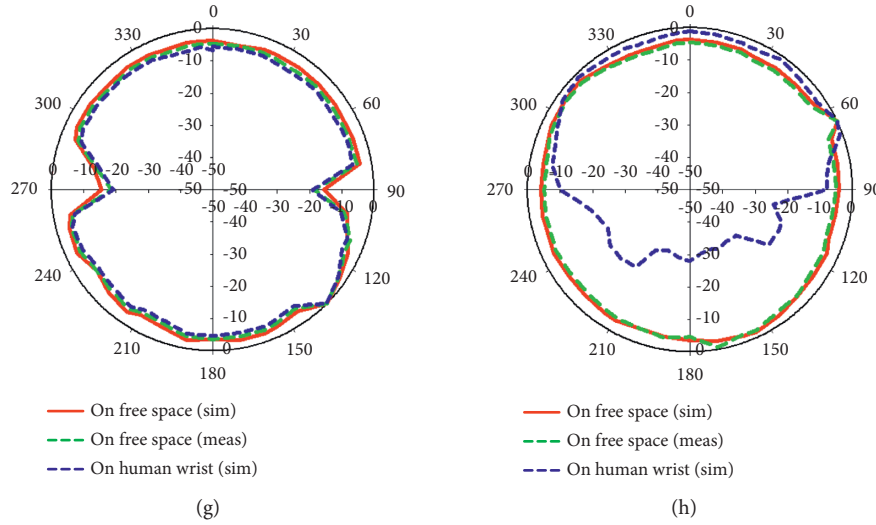


FIGURE 20: Radiation patterns of the proposed wristband antenna: (a) 2.4 GHz, E-plane, (b) 2.4 GHz, H-plane, (c) 3 GHz, E-plane, (d) 3 GHz, H-plane, (e) 6 GHz, E-plane, (f) 6 GHz, H-plane, (g) 10 GHz, E-plane, and (h) 10 GHz, H-plane.

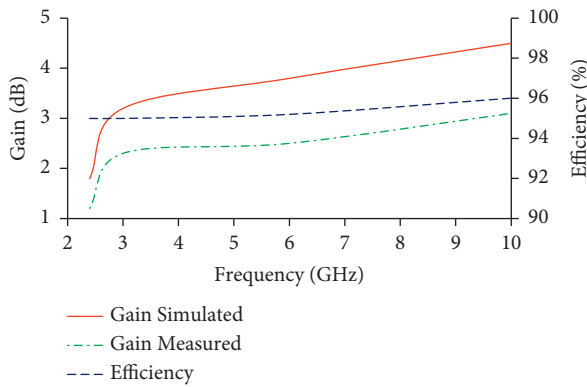


FIGURE 21: Gain and efficiency of the proposed wristband antenna.

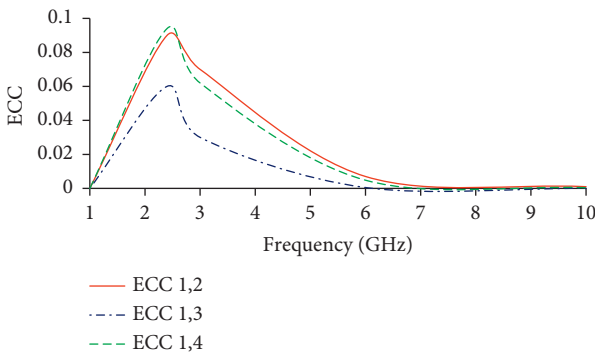


FIGURE 22: ECC of the proposed wristband antenna.

$$CCL = -\log_2 |\psi|^R. \quad (6)$$

The total active reflection coefficient (TARC) is defined as the ratio of total reflected power b_i to total incident power a_i , as given in the following equation [20]:

$$TARC = \frac{\sqrt{\sum_{i=1}^N |b_i|^2}}{\sqrt{\sum_{i=1}^N |a_i|^2}}. \quad (7)$$

The measured CCL and TARC values are depicted in Figures 24 and 25.

3.4. SAR Analysis. In body-worn wearable applications, the radiated energy is absorbed by the human body. This can be evaluated by using SAR analysis. The simulations of the antenna on the cylindrical human body model (shown in Figure 26) are carried out using the CST Microwave Studio[®] software using an input power of 1 Watt. The characteristics of the human body tissue model are tabulated in Table 2.

The obtained SAR values at 2.4 GHz, 3 GHz, 6 GHz, and 10 GHz frequencies are 0.191 W/Kg, 0.195 W/Kg, 0.718 W/Kg, and 0.928 W/Kg, respectively, which are less than the Federal Communications Commission (FCC) limit of 1.6 W/Kg, shown in Figure 27. The wristband antenna is also simulated using a human wrist phantom as depicted in Figure 28. The SAR values at 2.4 GHz, 3 GHz, 6 GHz, and 10 GHz are 0.308 W/Kg, 0.329 W/Kg, 0.543 W/Kg, and 0.873 W/Kg, respectively. The fabricated antenna prototype (shown in Figure 16(a)) is measured in free space and on a human wrist using the vector network analyzer, as shown in Figures 16(b) and 16(c), respectively. The simulated and measured reflection coefficients in free space and on the human body are depicted in Figure 29. It can be observed that both the simulated and measured reflection coefficients, in free space and on the human body, cover the 2.4 GHz band and UWB.

Table 3 compares the proposed wristband antenna with the existing antenna designs. Table 3 shows that the proposed wristband antenna covers the UWB and 2.45 GHz ISM band. The proposed antenna is conformal in comparison to the antenna designs reported in [21–25, 28, 29]. It

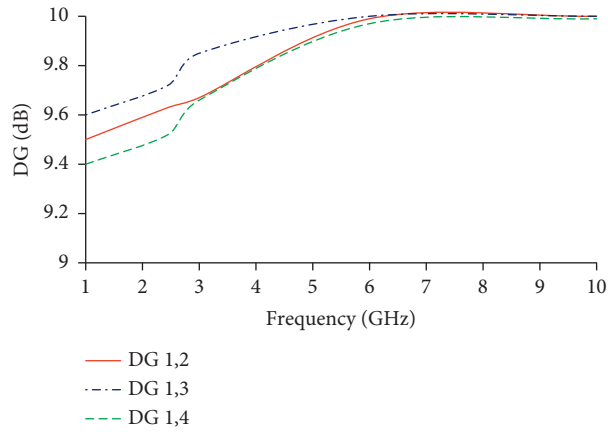


FIGURE 23: Diversity gain of the proposed wristband antenna.

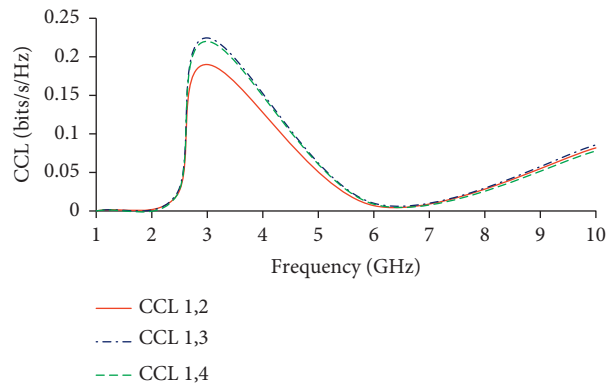


FIGURE 24: CCL of the proposed wristband antenna.

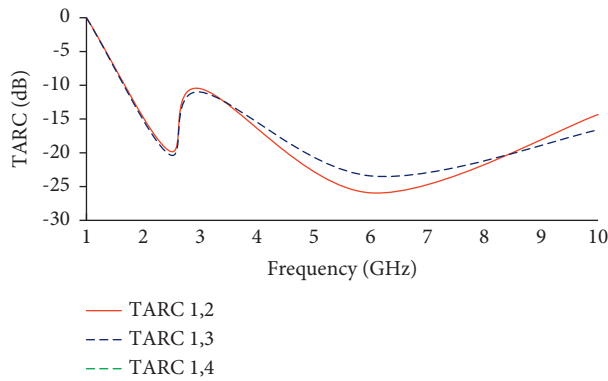


FIGURE 25: TARC of the proposed wristband antenna.

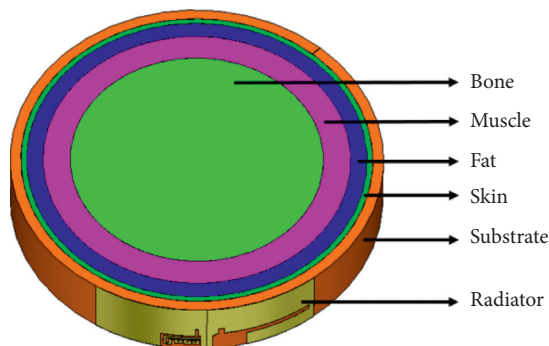


FIGURE 26: Cylindrical human body tissue model of the proposed wristband antenna.

TABLE 2: Characteristics of human body tissue.

Cylindrical human layers	Frequency (GHz)	Dielectric constant (ϵ_r)	Loss tangent ($\tan \delta$)	Thickness (mm)
Skin	2.4	42.923	0.272	1
	3	37.358	0.2786	
	6	34.215	0.3584	
	10	30.705	0.4806	
Fat	2.4	5.285	0.145	5
	3	5.2138	0.15011	
	6	4.8608	0.19612	
	10	4.5572	0.23373	
Muscle	2.4	52.791	0.241	13
	3	51.936	0.24804	
	6	47.069	0.34935	
	10	41.954	0.46476	
Bone	2.4	12.661	0.2524	12
	3	8.35	0.1434	
	6	7.73	0.173	
	10	7.6	0.196	

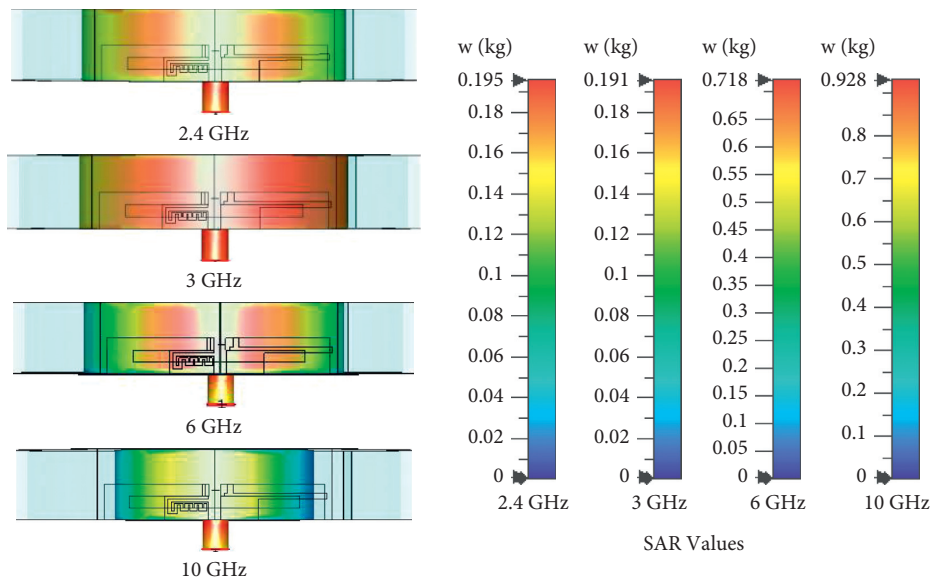


FIGURE 27: SAR values of the proposed wristband antenna using the cylindrical human tissue model.

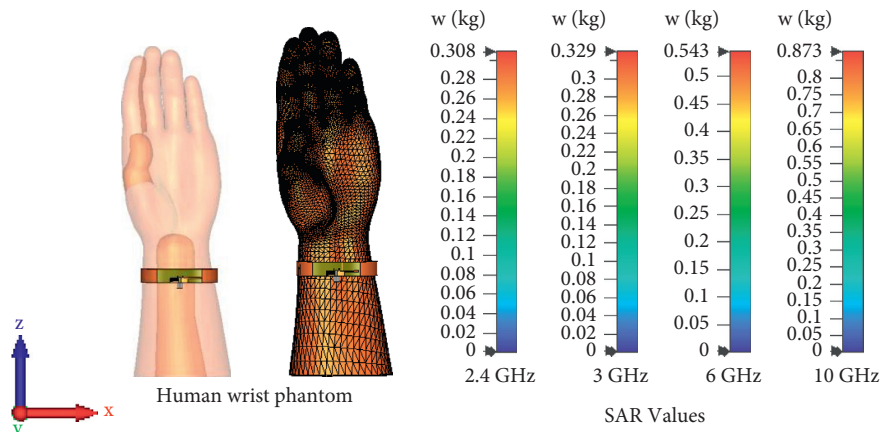


FIGURE 28: SAR values of the proposed wristband antenna on the human wrist phantom.

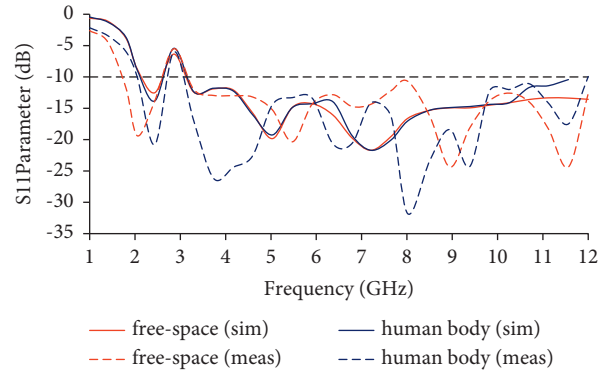


FIGURE 29: Reflection coefficients of the proposed wristband antenna in free space and on the human body.

TABLE 3: Comparison of the proposed wristband antenna with the existing designs.

Ref.	Size ($\lambda_g \times \lambda_g$)	Ports	Substrate	Bandwidth (GHz)	Diversity type	Isolation (dB)
[21]	0.616×0.51	4	Plexi glass	24.1–27.18, 33–44.13	—	>16
[22]	0.05×0.05	2	Roger RO4003 C	5.2–6.3	Polarization/pattern	>22
[23]	0.443×0.22	8	FR-4	3.1–6	Spatial	<10
[24]	0.095×0.014	2	FR-4	3.33–3.67	Pattern	>14
[25]	0.0148×0.0148	2	RO4350	0.665–1.3, 1.415–2, 2.42–3.09, 3.18–3.89	—	>11.7
[26]	0.32×0.32	3	Taconic TLY-5	4.63–5.87	Pattern	>16.5
[27]	0.996×0.126	2	Coloured plastic	7.96–8.76	—	>21
[28]	0.095×0.095	2	FR-4	2.18–2.85	Polarization	>13
[29]	0.214×0.214	4	FR-4	1.71–3.94	—	>26
[30]	0.158×0.1	2	Jean	2.74–12.33	—	>26
Prop.	0.437×0.025	4	Silicone rubber	2.1–2.6, 3.1–12	Pattern	>22

also provides greater than 20 dB isolation when compared with the antenna configurations of [21, 23–26, 28].

4. Conclusion

A body-worn wristband antenna is proposed in this work. The proposed MIMO antenna is composed of four horizontally placed antenna elements that provide pattern diversity. The proposed antenna has a -10 dB bandwidth of 8.9 GHz (3.1–12 GHz) in the UWB and 0.55 GHz (2.05–2.6 GHz) in the ISM band. SAR analysis is investigated to determine the radiation level for on-body applications. The obtained SAR values satisfy the limits recommended by the FCC. The proposed wristband MIMO antenna, due to its low cost, provides user safety on a limited budget.

Data Availability

The data used to support the findings are available from the corresponding upon request.

Conflicts of Interest

The authors declare that they have no conflicts of interest.

References

- [1] M. Virili, H. Rogier, F. Alimenti, P. Mezzanotte, and L. Roselli, "Wearable textile antenna Magnetically coupled to flexible active Electronic circuits," *IEEE Antennas and Wireless Propagation Letters*, vol. 13, pp. 209–212, 2014.
- [2] L. Zhang, Z. Wang, and J. L. Volakis, "Textile antennas and Sensors for body-worn applications," *IEEE Antennas and Wireless Propagation Letters*, vol. 11, pp. 1690–1693, 2012.
- [3] P. S. Taylor and J. C. Batchelor, "Finger-worn UHF far-field RFID tag antenna," *IEEE Antennas and Wireless Propagation Letters*, vol. 18, no. 12, pp. 2513–2517, 2019.
- [4] X. Shan and Z. Shen, "Miniaturized UHF/UWB tag antenna for indoor positioning systems," *IEEE Antennas and Wireless Propagation Letters*, vol. 18, no. 12, pp. 2453–2457, 2019.
- [5] Z. Hamouda, J.-L. Wojkiewicz, A. A. Pud et al., "Dual-band elliptical planar conductive polymer antenna printed on a flexible substrate," *IEEE Transactions on Antennas and Propagation*, vol. 63, no. 12, pp. 5864–5867, 2015.
- [6] H. Xiaomu, S. Yan, and G. A. E. Vandenbosch, "Wearable button antenna for dual-band WLAN applications with combined on and off-body radiation patterns," *IEEE Transactions on Antennas and Propagation*, vol. 65, no. 3, pp. 1384–1387, 2017.
- [7] E. F. Sundarsingh, M. Kanagasabai, and V. S. Ramalingam, "Completely integrated multilayered weave electro-textile antenna for wearable applications," *International Journal of Microwave and Wireless Technologies*, vol. 9, no. 10, pp. 2029–2036, 2017.
- [8] H. R. Khaleel, A. Issac, H. Al-Rizzo, and A. Bihnam, "Wearable printed monopole antenna for uwb and ism applications," in *Proceedings of the USNC-URSI Radio Science Meeting (Joint with AP-S Symposium)*, p. 5, Memphis, TN, USA, July 2014.
- [9] R. Narayan, S. Ataman, and M. Mathian, "A dual-band planar monopole antenna for 2.4 GHz ISM and UWB Applications," in *Proceedings of the IEEE 27th Convention of Electrical and*

- Electronics Engineers in Israel*, pp. 1–4, Eilat, Israel, November 2012.
- [10] X.-L. Li, G.-M. Yang, and Y.-Q. Jin, “Isolation enhancement of wideband vehicular antenna array using fractal decoupling structure,” *IEEE Antennas and Wireless Propagation Letters*, vol. 18, no. 9, pp. 1799–1803, 2019.
- [11] A. Alemarjee and S. Noghianian, “On-body low-profile textile antenna with artificial magnetic conductor,” *IEEE Transactions on Antennas and Propagation*, vol. 67, no. 6, pp. 3649–3656, 2019.
- [12] “Properties of silicone rubber,” <https://www.azom.com/properties.aspx?ArticleID=920>.
- [13] R. Singh and G. Kumar, *Broadband Planar Monopole Antennas*, IIT, Bombay, India, 2004.
- [14] K. P. Ray, “Design aspects of printed monopole antennas for ultra-wide band Applications,” *International Journal of Antennas and Propagation*, vol. 2008, Article ID 713858, 8 pages, 2008.
- [15] R. Sanyal, P. P. Sarkar, and S. Sarkar, “Octagonal nut shaped monopole UWB antenna with sextuple band notched characteristics,” *AEU-International Journal of Electronics and Communications*, vol. 110, pp. 1434–8411, 2019.
- [16] M. S. Sharawi, “Current Misuses and future Prospects for printed multiple-input, multiple-output antenna systems [wireless Corner],” *IEEE Antennas and Propagation Magazine*, vol. 59, no. 2, pp. 162–170, 2017.
- [17] A. Hoque, M. T. Islam, and A. F. Almutairi, “Low-profile slotted metamaterial antenna based on bi slot microstrip patch for 5g application,” *Sensors*, vol. 20, pp. 1–20, 2020.
- [18] M. Alibakhshikenari, B. S. Virdee, A. A. Althuwayb et al., “Study on on-Chip antenna design based on metamaterial-Inspired and substrate-integrated Waveguide properties for Millimetre-wave and THz integrated-circuit applications,” *Journal of Infrared, Millimeter and Terahertz Waves*, vol. 42, no. 1, pp. 17–28, 2021.
- [19] C. Yu, S. Yang, Y. Chen et al., “A super-wideband and high isolation MIMO antenna system using a windmill-shaped decoupling structure,” *IEEE Access*, vol. 8, pp. 115767–115777, 2020.
- [20] P. Kumar, S. Urooj, and A. Malibari, “Design and implementation of quad-element super-wideband MIMO antenna for IoT applications,” *IEEE Access*, vol. 8, pp. 226697–226704, 2020.
- [21] A. Desai, C. D. Bui, J. Patel, T. Upadhyaya, G. Byun, and T. K. Nguyen, “Compact wideband four element optically transparent MIMO antenna for mm-wave 5G applications,” *IEEE Access*, vol. 8, pp. 194206–194217, 2020.
- [22] U. Ullah, I. B. Mabrouk, and S. Koziel, “Enhanced-performance circularly polarized MIMO antenna with polarization/pattern diversity,” *IEEE Access*, vol. 8, pp. 11887–11895, 2020.
- [23] C.-Y.-D. Sim, H.-Y. Liu, and C.-J. Huang, “Wideband MIMO antenna array design for future mobile devices operating in the 5G NR frequency bands n77/n78/n79 and LTE band 46,” *IEEE Antennas and Wireless Propagation Letters*, vol. 19, no. 1, pp. 74–78, 2020.
- [24] Z. Xu and C. Deng, “High-isolated MIMO antenna design based on pattern diversity for 5G mobile terminals,” *IEEE Antennas and Wireless Propagation Letters*, vol. 19, no. 3, pp. 467–471, 2020.
- [25] R. Hussain, M. U. Khan, and M. S. Sharawi, “Design and analysis of a miniaturized meandered slot-line-based quad-band frequency agile MIMO antenna,” *IEEE Transactions on Antennas and Propagation*, vol. 68, no. 3, pp. 2410–2415, 2020.
- [26] K. Zhang, Z. H. Jiang, W. Hong, and D. H. Werner, “A low-profile and wideband triple-mode antenna for wireless body area network concurrent on-/off-body communications,” *IEEE Transactions on Antennas and Propagation*, vol. 68, no. 3, pp. 1982–1994, 2020.
- [27] A. K. Biswas, S. S. Pattanayak, and U. Chakraborty, “Evaluation of dielectric properties of colored resin plastic button to design a small MIMO antenna,” *IEEE Transactions on Instrumentation and Measurement*, vol. 69, no. 11, pp. 9170–9177, 2020.
- [28] B. Wang and S. Yan, “Design of smartwatch integrated antenna with polarization diversity,” *IEEE Access*, vol. 8, pp. 123440–123448, 2020.
- [29] A. Iqbal, A. Smida, A. J. Alazemi, M. I. Waly, N. Khaddaj Mallat, and S. Kim, “Wideband circularly polarized MIMO antenna for high data wearable biotelemetric devices,” *IEEE Access*, vol. 8, pp. 17935–17944, 2020.
- [30] A. K. Biswas and U. Chakraborty, “Compact wearable MIMO antenna with improved port isolation for ultra-wideband applications,” *IET Microwaves, Antennas & Propagation*, vol. 13, no. 4, pp. 344–354, 2019.

Research Article

Design and Performance Analysis of Compact Wearable Textile Antennas for IoT and Body-Centric Communication Applications

Sanjit Varma ¹, Somia Sharma ², Merbin John ¹, Richa Bharadwaj ²,
Anuj Dhawan ¹ and Shiban K. Koul ²

¹Department of Electrical Engineering, IIT Delhi, New Delhi 110016, India

²Centre for Applied Research in Electronics, IIT Delhi, New Delhi 110016, India

Correspondence should be addressed to Richa Bharadwaj; richabharadwaj@hotmail.com

Received 8 April 2021; Revised 23 July 2021; Accepted 12 August 2021; Published 24 August 2021

Academic Editor: Sachin Kumar

Copyright © 2021 Sanjit Varma et al. This is an open access article distributed under the Creative Commons Attribution License, which permits unrestricted use, distribution, and reproduction in any medium, provided the original work is properly cited.

This paper presents two compact textile-based planar dipole and loop antennas for wearable communication applications operating in the 2.4 GHz industrial, scientific, and medical radio (ISM) bands. The antennas were fabricated on a 0.44 mm thin camouflaged-military print, cotton jean cloth using conductive copper threads, and sewing embroidery technique to create the radiating structure. Design and performance analyses of the antennas were carried out using simulations; further experiments were performed in anechoic chamber and indoor environment to validate the designs. The experiments were carried out in a free space scenario and on the various locations of the human subject such as the torso and limb joints. The performance of the antennas was investigated based on the reflection coefficient in normal and bent conditions corresponding to the different radii of the locations of the human limbs. The antennas perform well in free space and on-body scenarios in flat and bend conditions providing return loss below -10 dB in all cases with an acceptable resonant frequency close to 2.4 GHz due to the antenna bending and body effects. The radiation pattern measurements are also reported in this work for free space and on-body scenarios. It is observed that the presence of the human body significantly influences the antenna radiation pattern which leads to an increase in the front-to-back ratio and also makes the antenna more directive. Overall, the performance of the fabricated embroidered textile antennas was found suitable for various wearable body-centric applications in indoor environments.

1. Introduction

Wearable communication technologies offer promising solutions for applications in the field of biomedical, consumer electronics, sports, military, and smart home applications. Recent developments in miniaturized and flexible electronic devices have made commercialization of such devices possible which has paved the road for vast utility in wearable Internet of Things (IoT) applications [1]. Their lightweight, low-cost manufacturing, ease of fabrication, and the availability of inexpensive flexible substrates (i.e., papers, textiles, and polymers) make flexible electronics an appealing candidate for the next generation of consumer electronics [2, 3].

Research is being carried out at various frequency bands available in the open literature for wireless body area

network (WBAN) applications ranging from 2.4/5.8 GHz industrial, scientific, and medical (ISM) band [4], 3.1–10.6 GHz ultra-wideband (UWB) [5–7], and the millimeter wave (mm-Wave) band 57–64 GHz [8, 9]. The 2.4 GHz ISM band is very suitable for wearable body-centric communication due to the global availability of the spectrum and wide range of applications in the field of healthcare, smart homes, sports, military, and day-to-day life [2, 3].

Antenna is one of the key components of the wearable communication device providing a robust communication link between various devices. Wearable antennas should be very compact, low-profile, lightweight, mechanically robust, efficient, and preferably flexible to suit the conformal structure of the body surface [2–5]. These antennas should also perform well when placed in proximity of the human body and have suitable performance in terms of operating

frequency and desired radiation characteristics [10]. Several works have been carried out on rigid substrates which lack flexibility and can be fragile due to the dynamic movements and postures made by the user. To address this problem, various flexible substrates are proposed in the open literature. Commonly used flexible materials for antennas are polyimides (PI), polydimethylsiloxane (PDMS), polytetrafluoroethylene (PTFE), liquid crystal polymer (LCP), Kapton, and paper-based substrates [2, 3, 6–9, 11].

Apart from polymer-based substrates, textile-based substrates are also gaining popularity due to the ease of integration of the antenna directly with the clothing as well as due to the flexible and conformal nature of the textile fabrics [12]. Textile materials commonly used as substrates are cotton cloth, felt, denim, fleece, nylon, and polyester. Different fabrication methods are chosen depending on the substrate material, application, and suitability; these methods include inkjet-printing, screen-printing, 3D printing, sewing, and embroidered techniques [2, 3, 13, 14]. Textile material selection in terms of electrical properties and thickness, manufacturing process, feeding method, and the overall antenna design are important aspects to be considered while designing such antennas. Antenna designs such as dipole, loop, spiral, and patch are commonly chosen structures for various communication applications [15–20]. Advanced antenna structures like (electromagnetic bandgap) EBG, artificial magnetic conductors (ACM), and substrate-integrated waveguide (SIW) antennas to enhance the performance of the antenna have been reported in open literature [21–23].

This paper proposes two compact, low-profile textile-based antennas which can be integrated into the clothing suitable for healthcare, indoor, and military IoT applications. The proposed design exploits the lightweight and flexible properties of the cotton cloth along with the high conductivity copper threads which are embroidered using sewing technology to form the radiating elements over the textile. The dipole antenna operates at 2.19–3.44 GHz and the loop antenna operates at 2.35–2.81 GHz frequency range in free space scenario. Various antenna parameters such as return loss and radiation patterns have been analysed for free space and on-body scenarios. Flexibility tests have also been carried out by bending the antenna at different radii corresponding to that of the radii of the limb joints of the human subject.

The novelty of the work described in this paper lies in the fabrication of highly conformal and flexible textile antennas using highly flexible customized copper threads in an automated manner. Moreover, this paper presents an in-depth analysis and comparison for the two textile antennas for on-body measurements in flat as well as bending scenarios (apart from free space scenarios), which is limited in the open literature. Various positions of the limbs have also been analysed to see the effect of orientation and proximity with the torso/thigh region depending on the antenna location. A 0.44 mm thin jeans cloth has been employed as a substrate which makes the antenna design more challenging.

The antenna prototypes are presented in Section 2 along with the simulation and measurement results. Section 3 gives

details of the on-body measurement procedure and compares free space and on-body measurements related to S_{11} and far-field radiation patterns. Section 4 deals with the study on the influence of the antenna performance when bent at different radii for free space and on-body scenarios and key findings are reported. The conclusion is presented in Section 5 with highlights on the future aspects.

2. Fabricated Textile Antenna Prototype and Performance Analysis

The proposed textile dipole and loop antenna structures comprise the radiating elements (two arms and rectangular loop structure, resp.) fabricated using the copper metal threads over a jeans cotton cloth fabric. These flexible and conformal copper threads or yarns were developed by twisting multiple thin copper wires, each wire's diameter being 0.071 mm. The antennas are designed to work at 2.4 GHz, ISM band using the jeans cotton material as the substrate with a relative permittivity of 1.67 [12]. The copper threads are embroidered into the substrate material of the antennas to form the radiating elements. The thickness of the copper thread is 0.345 mm throughout and the substrate thickness is around 0.44 mm.

The final schematic and dimensions of the antennas are present in Figure 1(a) for the dipole antenna and Figure 1(b) for the loop antenna. The length of the dipole antenna arm is calculated by half-wavelength of the desired frequency, that is, 2.4 GHz. The separation between the two antenna arms and the length of those arms are important factors that are sensitive to the change in the output frequency at which the antenna performs. To verify the proposed design performance before physically fabricating them using the embroidery sewing tool, a CST model was simulated with the same dimensions.

The sewing machine used to fabricate the copper-thread-based antennas over the textile material is Bernina B720 [24]. This machine has a Bernina hook system, which gives it a maximum sewing and embroidery speed of 1000 stitches per minute. The maximum stitch width the tool can provide is 5.5 mm with a maximum stitch length of 6 mm. The antenna design models were integrated with the tool using the “Bernina Embroidery Software Designer Plus” software which was purchased along with the sewing tool itself. Figure 1(c) shows the sewing process in which a dipole antenna pattern is being embroidered using copper thread over the denim cloth fabric.

A thin 3 mm foam (which provides no changes in the relative permittivity) was applied on the backside of the antenna fabric to add extra support to the textile during free space and body-centric measurements. The fabricated prototype of the textile dipole antenna and loop antenna is presented in Figures 1(d) and 1(e), respectively. A 50 Ω SMA connector was carefully soldered to the edges of the dipole and rectangular loop structures.

The performance of the wearable textile antennas was measured through a programmable 2-port vector network analyser (PNA-E8364C) in terms of reflection coefficient (S_{11}) and compared with the simulated results obtained from CST

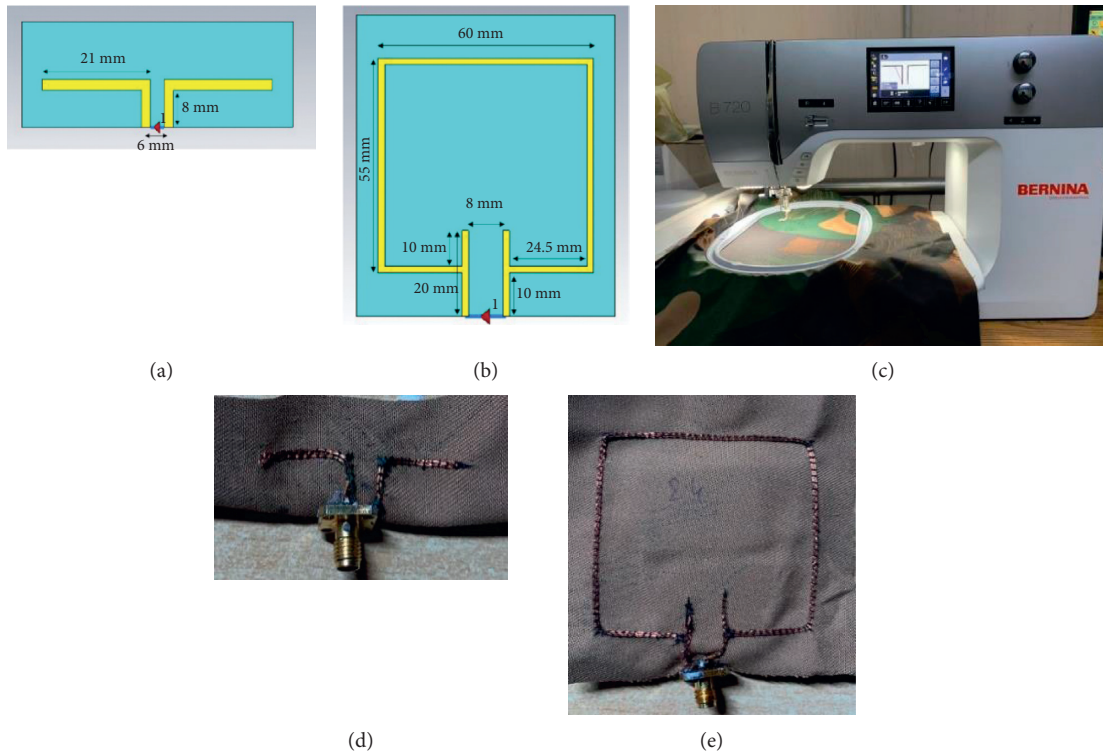


FIGURE 1: Schematic of the textile-based (a) dipole and (b) loop antenna. (c) The Bernina 720 sewing machine tool used for sewing the radiating element structures in the form of embroidered pattern over the denim-cotton fabric. Fabricated prototype of the textile (d) dipole and (e) loop antenna.

microwave studio. Radiation pattern measurements were also carried out in the anechoic chamber at the RF and Microwave Lab, CARE, IIT Delhi, and with those obtained from the simulation results. Good agreement is found between the simulation and measurement results for both proposed antennas. Figure 2(a) presents S_{11} results for the simulated and measured textile dipole antenna structure. It is observed that both results provide below -10 dB return loss and resonate in the 2.4 GHz, ISM band, and perform well in a free space/indoor environment. The deviations observed in the simulated and measured results can be possibly attributed to the radiating material in these textile antennas being conductive threads in comparison to a uniform sheet of copper in the simulated design, as well as to a difference in the permittivity of the substrate employed in the simulations from that of the jeans cloth substrate in these antennas. The presence of a 50-ohm SMA conductor soldered to the antenna structure can also bring about some variation between the measured and simulated results. Figures 2(b) and 2(c) present the simulated and measured radiation pattern of the dipole antenna for E-plane and H-plane. Similar radiation patterns are observed for both cases, hence validating the performance of the fabricated antenna.

3. Body-Centric Measurement Scenarios

Body-centric measurements were performed on a human subject in an indoor laboratory environment in the 2.4 GHz ISM frequency band. The male human subject has

a height of 167 cm and a weight of 74 kg with an average build. The wearable antenna was placed on the torso region of the human subject to compare with the free space S_{11} results (Figure 3(a)). The wearable textile antennas are able to achieve below -10 dB return loss for on-body scenarios indicating good performance of the antenna when placed in the proximity of the body. An example of the measured and simulated S_{11} results of the textile loop antenna is presented in Figure 3(b), for both the free space and the on-body scenarios. For the on-body simulation results, a phantom representing the torso region of the human body with dimensions $200 \times 200 \times 70$ mm³ is designed in CST microwave studio. The human phantom consists of skin, fat, and muscle as the three layers with electrical properties such as permittivity and conductivity as per data provided in [25] for 2.4 GHz frequency. The thickness of the skin, fat, and muscle layer is 3 mm, 7 mm, and 60 mm, respectively [26]. A shift of 100 MHz in the resonant frequency is observed when placed over the body (2.4 GHz) in comparison to the free space (2.5 GHz) results which is due to the body effects that influence the antenna performance.

Apart from S_{11} measurements, far-field radiation pattern measurements are also carried out for both antennas studied in an anechoic chamber for free space and on-body scenarios. The antenna pattern measurements are performed for E-plane and H-plane to understand the influence of the human subject in both planes. The results for the textile dipole antenna and loop antenna are presented in

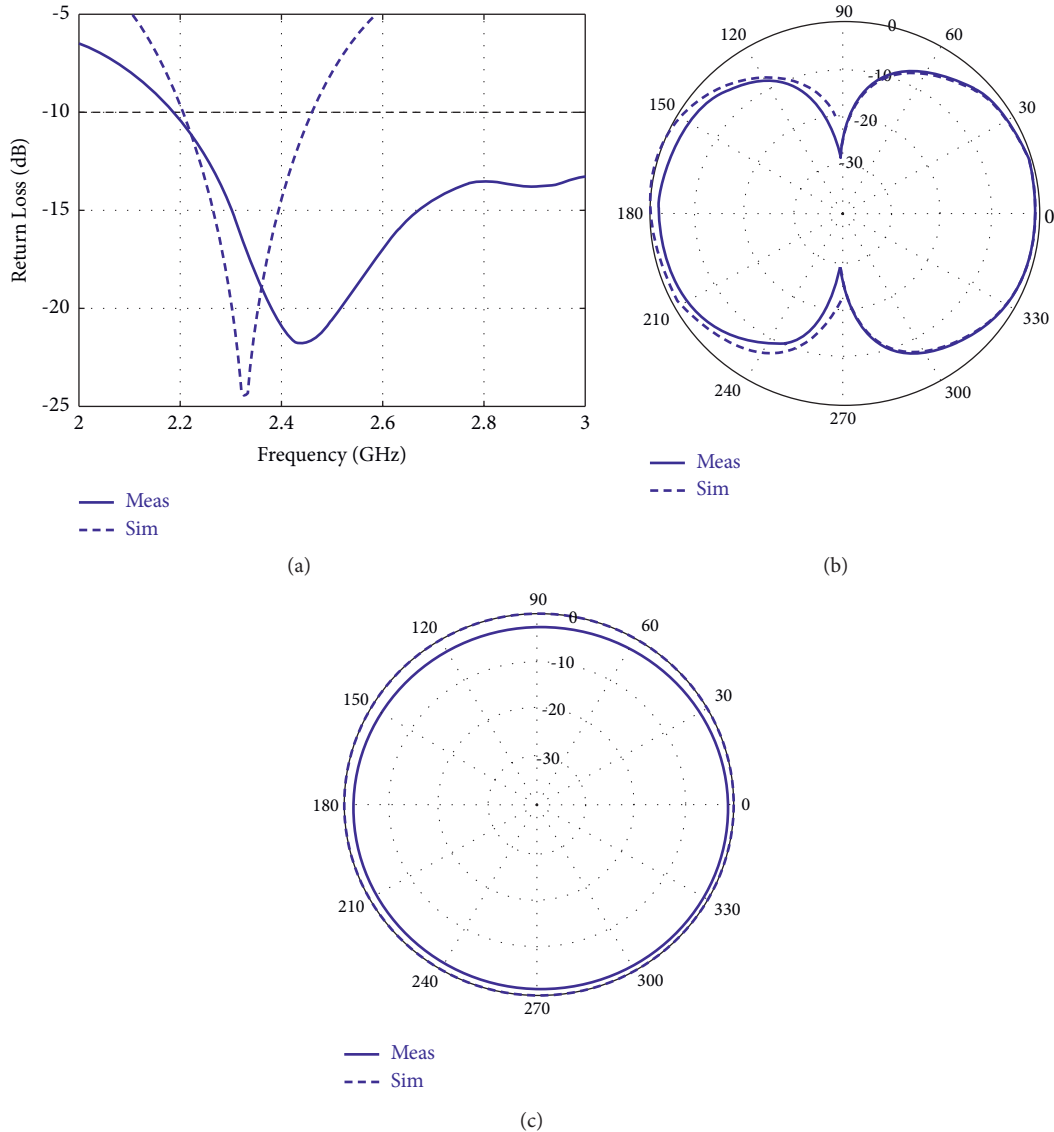


FIGURE 2: Measured and simulation results for S_{11} parameters for free space scenario: (a) dipole antenna. Measured and simulated antenna radiation pattern results: (b) E-plane and (c) H-plane.

Figures 4(a)–4(d), respectively. It is observed that both antennas are strongly influenced by the presence of the human subject which increases the front-to-back ratio of the radiation pattern and makes the pattern more directive in nature [27, 28].

4. Impact of Antenna Bending

One of the main challenges of the textile wearable antenna design is the uncertain form of the garment surface due to frequent movements performed by the human subject and also the nature of the fabric [29]. Hence, the wearable antennas integrated with the garment also encounter scenarios such as bending, stretching, flexing, and crumpling apart from the normal flat condition [29, 30]. This section evaluates the antenna performance under bending conditions for free space and on-body scenarios.

4.1. Free Space Measurements. For free space measurements, the antenna is bent over a cylindrical foam of different radii corresponding to the curvatures of the joints of the limbs of the human subject. The limb joints considered are wrist, elbow, shoulder, and knee. Figures 5(a) and 5(b) present the experimental setup for the antenna bent on foam for the dipole antenna for the radii corresponding to the wrist and elbow. Figures 5(c) and 5(d) present the experimental setup for the antenna bent on foam for the loop antenna for the radii corresponding to the shoulder and knee. Table 1 summarises the radii and circumference values for various limb locations chosen that are considered for free space foam experiments to measure the S_{11} parameters.

The S_{11} results corresponding to different bending radii are presented in Figures 6(a) and 6(b) for the dipole and loop antenna, respectively. It is observed that the bending condition of the textile antenna has a strong effect on the S_{11}

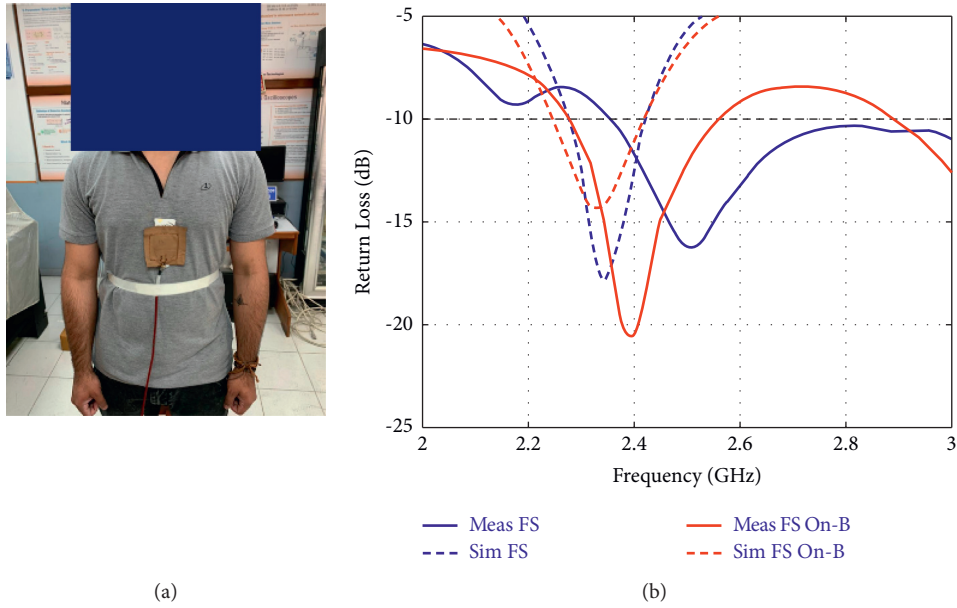


FIGURE 3: (a) Textile loop antenna is placed on the torso region of the human subject. (b) Free space (FS) and on-body (On-B) S_{11} measurement and simulation results.

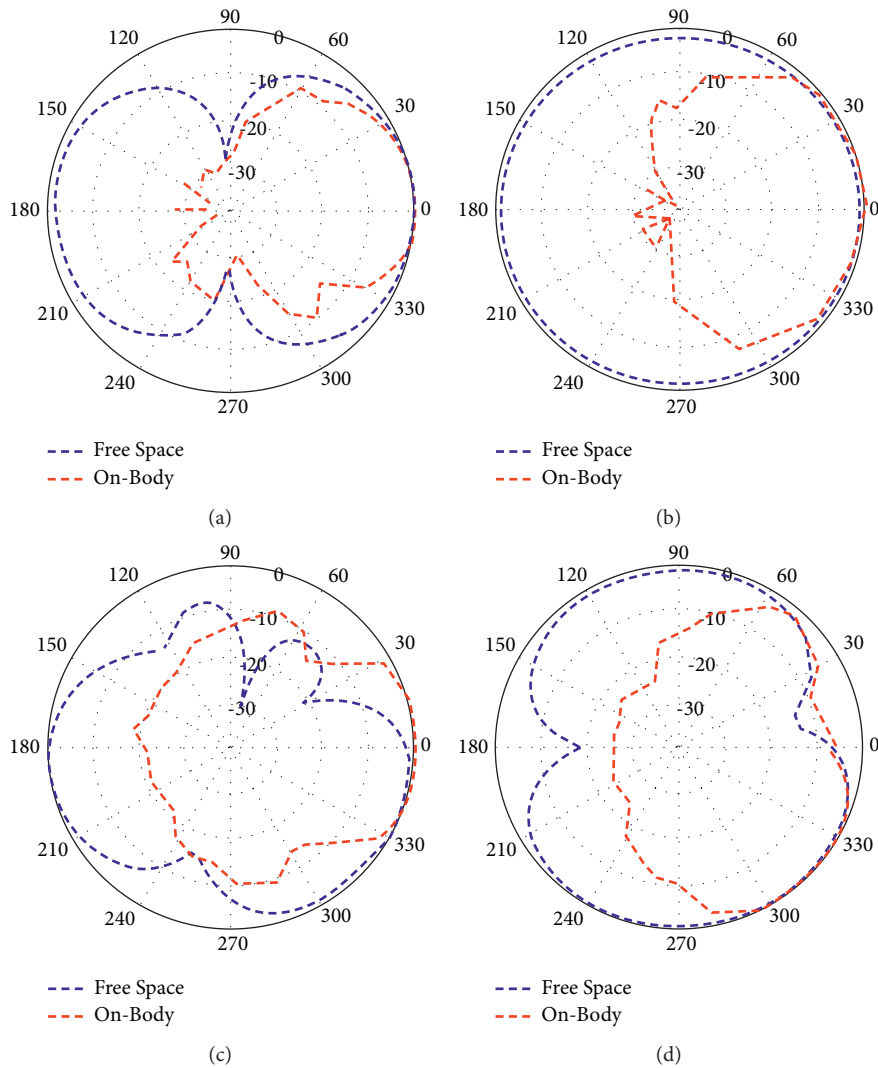


FIGURE 4: Measured free space and on-body radiation patterns. Dipole antenna: (a) E-plane and (b) H-plane. Loop antenna: (c) E-plane and (d) H-plane.

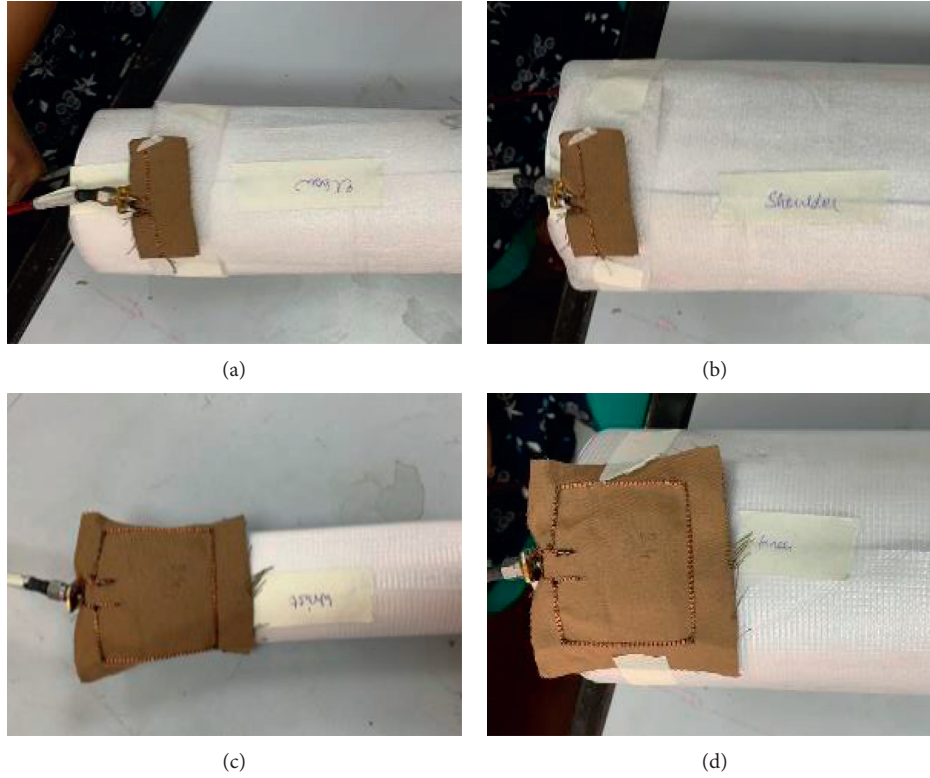


FIGURE 5: Photograph of the various antenna structures bent with different radii corresponding to the limb joint locations. Textile dipole antenna: (a) elbow and (b) shoulder. Textile loop antenna: (c) wrist and (d) knee.

TABLE 1: Wearable antenna locations: radii values for free space and on-body antenna bending experiment

	Radii (mm)	Circumference (mm)
<i>Upper limbs</i>		
Wrist	25.7	161.5
Elbow	42.9	270.0
Shoulder	54.1	340.0
<i>Lower limbs</i>		
Knee	57.2	359.4

results leading to a shift in the resonant frequency and also the magnitude of the S_{11} results. Significant deviation from the flat case results is observed for the lowest bending radii = 25.7 mm as the antenna structure is quite affected by the degree of bending taking place especially for the textile dipole antenna. The bending scenario leads to a change in the resonant length of the antenna leading to variation in the S_{11} characteristics. Minimum variation is observed for the highest bending radii = 57.2 mm as this scenario is approaching towards the flat orientation of the antenna. As observed in Figure 6(a), the dipole antenna resonant frequency spans from 2.45 GHz to 2.58 GHz and the loop antenna resonant frequency spans from 2.48 GHz to 2.52 GHz for the bending radii range considered. The S_{11} magnitude of the resonant frequency varies from -20.16 dB to -18.56 dB and -15.41 to -14.98 dB for the dipole and loop antenna, respectively. The variation of the resonant frequency and the magnitude is more significant for the textile dipole antenna.

4.2. On-Body Measurements. On-body antenna bending experiments have been carried out for various locations of the human subject which are the wrist, elbow, shoulder, and knee joints. The antenna bending experiment is performed for two positions of the upper and lower limb while the subject is in a sitting posture. In the first position, the arm is at a 0-degree position with respect to the shoulder joint (as depicted in Figure 7(a)) and the leg is stretched out straight making 0 degrees with respect to the thigh joint (as depicted in Figure 7(b)). In the second scenario, the position of the arm is at 90 degrees with respect to the shoulder joint (as depicted in Figure 7(c)) and the leg bent at 90 degrees with respect to the knee joint (as depicted in Figure 7(d)).

As observed in Figures 8(a), 8(b), 9(a), and 9(b) corresponding to the dipole antenna and loop antenna, respectively, the S_{11} magnitude and resonant frequency vary for various on-body locations on the antenna. This is attributed to the body effects and also the different curvatures of bending of the textile antenna depending on the radii of

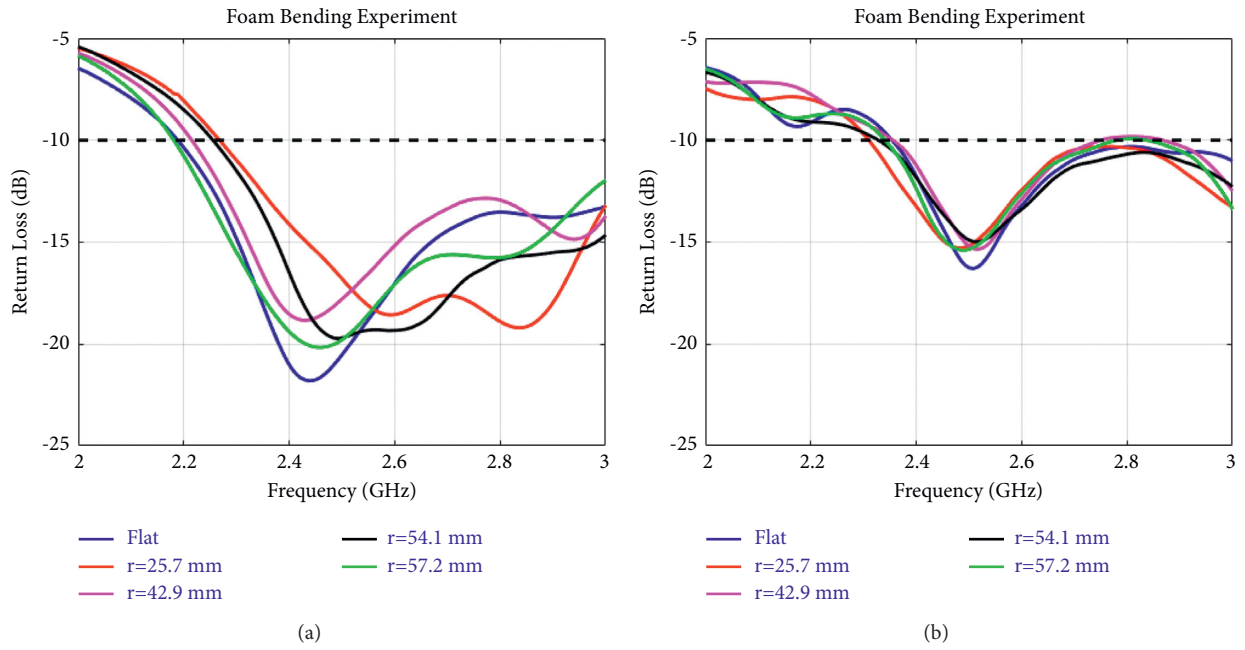


FIGURE 6: Measured S_{11} plots of the antennas bent with different radii: (a) dipole antenna and (b) loop antenna. Bending radii considered ranges from 25.7 mm to 57.2 mm and compared with the flat case scenario.



FIGURE 7: Continued.



FIGURE 7: Measurements for various on-body antenna locations and bending curvatures for the upper and lower limbs. Position I (0 degrees): (a) dipole antenna, wrist, and (b) dipole antenna, knee. Position II (90 degrees): (c) loop antenna, elbow, and (d) loop antenna, knee.

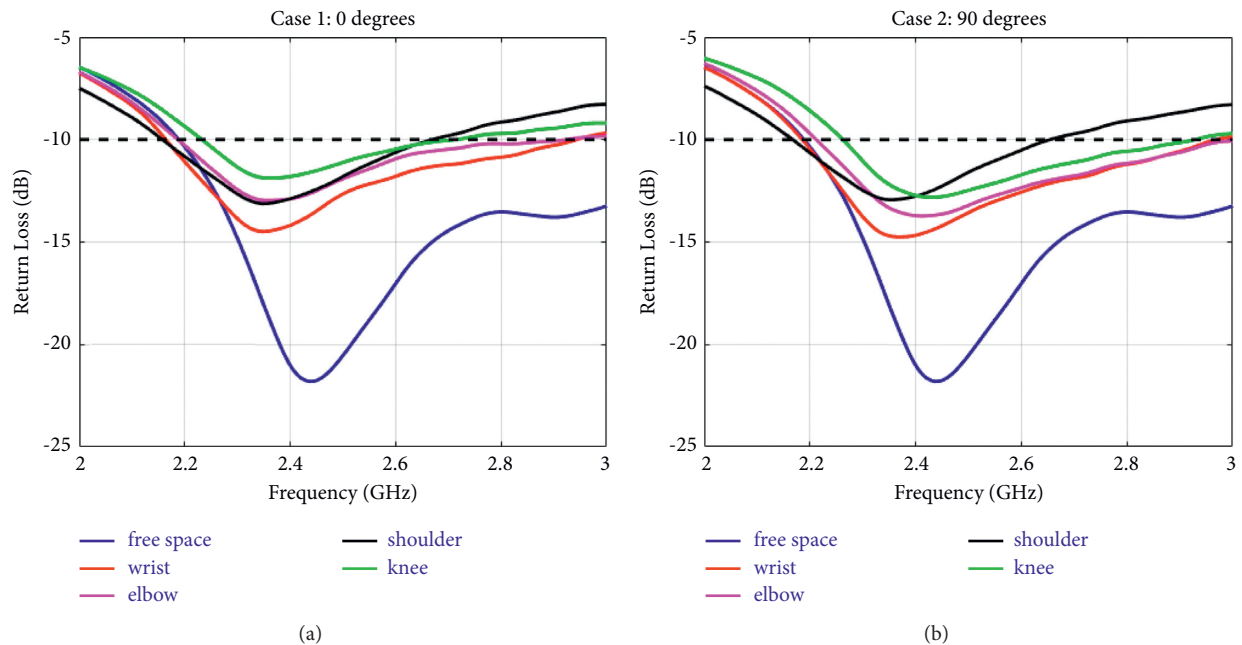


FIGURE 8: Variation in S_{11} results for the textile dipole antenna for various on-body limb locations and bending radii: (a) position I (0 degrees) and (b) position II (90 degrees).

the body locations. For the dipole antenna, the S_{11} curve shifts upward due to the antenna bending with a span of magnitude ranging from -14.5 dB to -11.8 dB for Position I and -14.9 dB to -12.8 dB for Position II. The resonant frequencies shift in the range of 2.34 GHz to 2.38 GHz for Position I and 2.38 GHz to 2.41 GHz for Position II. Both orientations of the limbs 0 and 90 degrees show similar

variation in the S_{11} parameters with a 90-degree scenario depicting slightly better S_{11} resonance. This can be due to the reduction in body effects caused from the torso or thigh region when the limbs are positioned in the 90-degree case.

For the textile loop antenna, higher fluctuation in the magnitude of the S_{11} results are observed (Figures 9(a)–9(b)) for the different on-body locations and bending curvatures.

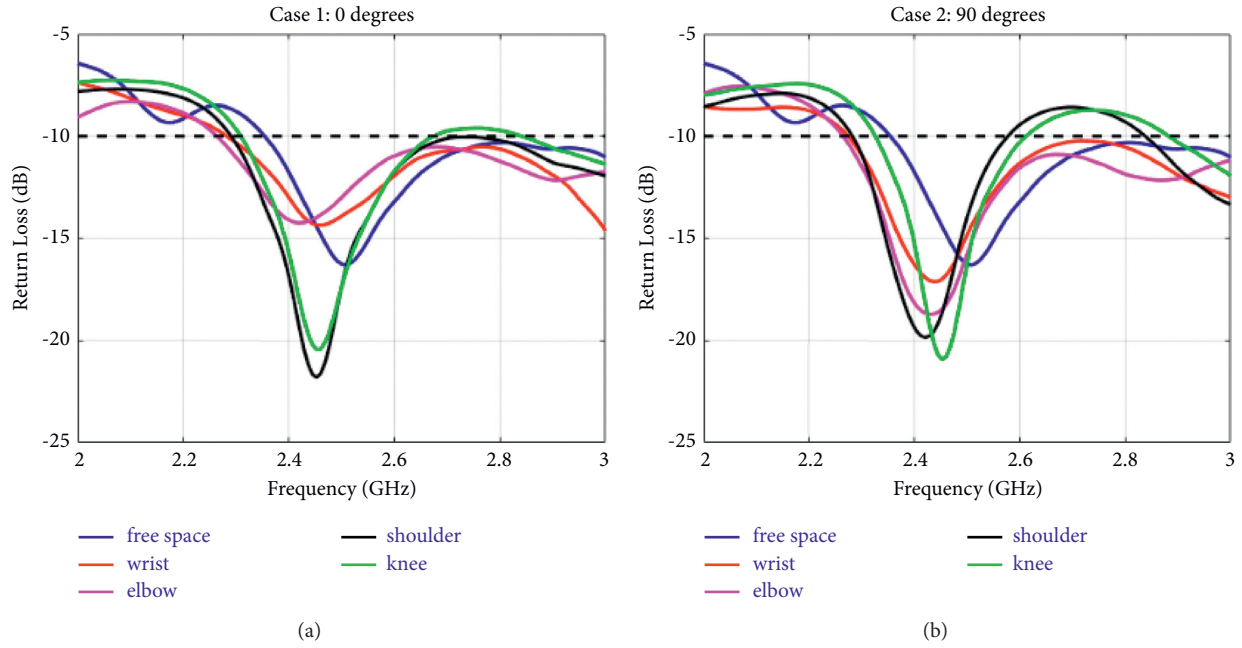


FIGURE 9: Variation in S_{11} results for the textile loop antenna for various on-body limb locations and bending radii: (a) position I (0 degrees) and (b) position II (90 degrees).

TABLE 2: Comparison of textile antennas with proposed antennas.

	Textile antenna structure	Substrate material/ conductive material	Antenna parameters					Bending effects (FS)	Body effects
			RF (GHz)	S_{11} (dB)	BW (MHz)	G (dB)	E (%)		
[31]	Wideband monopole: D: $50 \times 64.1 \text{ mm}^2$; F: 2.45 GHz	2 mm jeans cloth/ Copper tape	2.45	-17.2	667	3.27	—	—	—
[32]	E-shaped patch CPW feed structure: D: $32 \times 30 \text{ mm}^2$; F: 2.45 GHz	2 mm denim cloth/ Copper foil	2.45	-34	153	1.83	—	—	—
[33]	Rectangular loop, CPW fed transmission line, and backside reflector: D: $62 \times 32 \text{ mm}^2$; F: 2.45 GHz	1.5 mm denim fabric/ Conductive fabric	2.47	-17	285	—	—	—	Presence of reflector reduces effect of human body
[34]	Centre-fed patch with a U-shape aperture: D: $70 \times 85 \text{ mm}^2$; F: 2.45 GHz	6 mm felt fabric/ Copper tape	2.4	-12	100	—	—	Yes	Yes
[26]	Textile planar inverted F antenna (PIFA): D: $80 \times 140 \text{ mm}^2$; F: 433 MHz, 2.45 GHz	6 mm thick felt fabric/ Conductive textile sheet	2.42	-20	309	6.1	—	—	The efficiency decreases by 10% as the radiated patch is shielded by ground
[35]	Patch antenna with slots: D: $115 \times 123 \text{ mm}^2$; F: 2.45 GHz	2 mm woven cotton cloth Zari—silver metallic yarn wrapped in silk thread	2.4	-28	500	7.11	67	40, 60, and 80 mm radii significant changes for various body locations	Significant changes in S_{11} and RF for various body locations
[36]	Patch antenna with a full rear ground plane: D: $80 \times 100 \text{ mm}^2$; F: 2.45 GHz	1.7 mm felt fabric/ ShieldIT superconductive textile	2.44	-15	70	6.33	61	—	Changes observed

TABLE 2: Continued.

Textile antenna structure	Substrate material/ conductive material	Antenna parameters						Bending effects (FS)	Body effects
		RF (GHz)	S_{11} (dB)	BW (MHz)	G (dB)	E (%)			
[37] E-shape triband dipole antenna: D: $80 \times 80 \text{ mm}^2$; F: 2.4, 5.75, and 5.25 GHz	2 mm denim fabric/ Copper tape	Measured						30, 50, and 70 mm radii prominent changes observed	Considerable degradation observed
		2.45	-18	100	1.26	40			
Dipole antenna: D: $20 \times 60 \text{ mm}^2$; Loop antenna: D: $75 \times 80 \text{ mm}^2$; F: 2.4 GHz	0.44 mm jeans cloth/ Highly flexible copper e-threads	Measured						25, 43, 54, and 57 radii	Five body locations
		2.43/ 2.5	-21/ -16.3	Dipole/loop antenna 130/45		2.3/ 4.3	95/ 98		

The magnitude varies from -21 dB to -14 dB for the various on-body locations considered. This variation depends on various factors such as the bending radii, surface on which the antenna is placed on the body (directly on the skin/above clothing) and distance from the body surface. The shift in the resonant frequency from the free space results is less for the various bending radii chosen in comparison to that of the textile dipole antenna.

The shift ranges from 2.42 GHz to 2.45 GHz of frequency. It can be concluded that the type of antenna, location of the wearable antenna, bending radii of the antenna, and also the orientation of the limbs can cause some variation in the S_{11} characteristics such as resonant frequency, impedance bandwidth, and S_{11} magnitude. It is also observed that, in all the scenarios considered, the magnitude of the S_{11} is below -10 dB and also resonating close to the desired frequency of operation which is the 2.4 GHz ISM band. For the dipole antenna, the shift observed ranges from 10 MHz to 60 MHz and for the loop antenna, the shift observed is in the range of 20 MHz to 50 MHz, for on-body scenarios when compared with the desired 2.4 GHz resonant frequency.

5. Comparison with Related Previous Works

Table 2 compares the work described in this paper with the other existing works from the literature [26, 31–37]. The novelty of the work described in this paper lies in the fabrication of highly conformal, flexible, and compact textile antennas using highly flexible customized copper threads in an automated manner. The fabrication of these low-profile textile antennas was carried out on very thin textile substrates that are suitable for free space and body-centric applications. The performance of the two antennas is compared for various bending conditions and on-body scenarios for which a detailed analysis has been provided. It has to be mentioned that such comparison or analysis is very limited considering the research work on textile antennas present in the open literature. The body-centric measurements have been carried out for various locations on the body and also for different orientations of the limbs. The proposed antennas have been designed using a very thin textile jean cloth (of thickness 0.44 mm) and are still able to

achieve the desired resonant frequency in normal conditions as well as in bending scenarios. The proposed antennas are fabricated on the jeans cloth using digital embroidery technology with the radiating elements made from highly conformal and flexible customized copper e-threads of diameter 0.345 mm, which gives acceptable results for various on-body locations and limb orientations. The copper yarn is made from twisting multiple copper threads of 0.071 mm in diameter. The copper e-threads have higher conductivity and provide higher performance in comparison to threads made of other metals (such as silver or steel) that have been employed in previous works [14, 35, 38]. Most of the works in open literature use conductive fabrics [26, 33, 36] or copper tapes/foil [31, 32, 34, 37] which are glued over the textile fabric that makes the antenna not durable to withstand repeated use and harsh environments. The use of e-threads (conductive threads) as the radiating elements makes it feasible to integrate the antenna into clothing, thus making the movement of human subject unobtrusive and comfortable.

6. Conclusion

This work proposes two textile-based antennas for IoT and body-centric communication applications, namely, dipole and loop antenna. The performance of the wearable antenna is investigated in free space and in proximity with the human body. The antennas have been fabricated on cost-effective and commercially available textile cotton cloth and the radiating structure made of conductive copper threads has been formed using the sewing embroidered technique. The proposed antennas are compact and flexible with good agreement between the measured and simulated results operating at 2.4 GHz.

Return loss and radiation pattern characteristics for free space and on-body scenarios have been presented and discussed. The return loss of the antenna shows good performance in free space and on-body scenarios. The antenna radiation pattern becomes more directive for the wearable scenario in comparison to free space which is due to the presence of the human subject. Flexibility tests have also been carried out for different bending radii corresponding to the curvature of the human limbs which are probable

locations where the wearable devices can be placed or integrated with the clothing. The performance of the antennas deviates slightly in terms of resonant frequency, the bandwidth of the operation which is attributed to the bending condition and body effects leading to variation in the results. The antennas perform well in free space and on-body scenarios which make them suitable candidates for wearable communication applications.

Data Availability

Data are available upon request to Dr. Richa Bharadwaj (e-mail: richab@care.iitd.ac.in).

Conflicts of Interest

The authors declare that they have no conflicts of interest.

Acknowledgments

The authors would like to acknowledge the Defence Research and Development Organisation (RP03437G) for providing funding for this work.

References

- [1] F. John Dian, R. Vahidnia, and A. Rahmati, "Wearables and the internet of things (IoT), applications, opportunities, and challenges: a survey," *IEEE Access*, vol. 8, pp. 69200–69211, 2020.
- [2] M. El Gharbi, R. Fernández-García, S. Ahyoud, and I. Gil, "A review of flexible wearable antenna sensors: design, fabrication methods, and applications," *Materials*, vol. 13, no. 17, p. 3781, 2020.
- [3] S. G. Kirtania, A. W. Elger, M. R. Hasan et al., "Flexible antennas: a review," *Micromachines*, vol. 11, no. 9, p. 847, 2020.
- [4] M. E. Jalil, M. K. A. Rahim, N. A. Samsuri, N. A. Murad, N. Othman, and H. A. Majid, "On-body investigation of dual band diamond textile antenna for wearable applications at 2.45 GHz and 5.8 GHz," in *Proceedings of the 2013 7th European Conference on Antennas and Propagation (EuCAP)*, pp. 414–417, Gothenburg, Sweden, April 2013.
- [5] R. Bharadwaj, S. Swaisaenyakorn, C. G. Parini, J. C. Batchelor, and A. Alomainy, "Impulse radio ultra-wideband communications for localization and tracking of human body and limbs movement for healthcare applications," *IEEE Transactions on Antennas and Propagation*, vol. 65, no. 12, pp. 7298–7309, 2017.
- [6] H. R. Khaleel, H. M. Al-Rizzo, D. G. Rucker, and S. Mohan, "A compact polyimide-based UWB antenna for flexible electronics," *IEEE Antennas and Wireless Propagation Letters*, vol. 11, pp. 564–567, 2012.
- [7] A. Yadav, V. Kumar Singh, A. Kumar Bhoi, G. Marques, B. Garcia-Zapirain, and I. de la Torre Diez, "Wireless body area networks: UWB wearable textile antenna for telemedicine and mobile health systems," *Micromachines*, vol. 11, no. 6, p. 558, 2020.
- [8] M. Ur-Rehman, T. Kalsoom, N. A. Malik et al., "A wearable antenna for mmWave IoT applications," in *Proceedings of the 2018 IEEE International Symposium on Antennas and Propagation & USNC/URSI National Radio Science Meeting*, pp. 1211–1212, Boston, MA, USA, July 2018.
- [9] J. Pourahmadazar and T. A. Denidni, "60 GHz antenna array for millimeter-wave wireless sensor devices using silver nanoparticles ink mounted on a flexible polymer substrate," *Microwave and Optical Technology Letters*, vol. 59, no. 11, pp. 2830–2835, 2017.
- [10] R. Bharadwaj and S. K. Koul, "Assessment of limb movement activities using wearable ultra-wideband technology," *IEEE Transactions on Antennas and Propagation*, vol. 69, no. 4, pp. 2316–2325, 2021.
- [11] M. Ullah, M. Islam, T. Alam, and F. Ashraf, "Paper-based flexible antenna for wearable telemedicine applications at 2.4 GHz ISM band," *Sensors*, vol. 18, no. 12, p. 4214, 2018.
- [12] C. Hertleer, H. Rogier, L. Vallozzi, and L. Van Langenhove, "A textile antenna for off-body communication integrated into protective clothing for firefighters," *IEEE Transactions on Antennas and Propagation*, vol. 57, no. 4, pp. 919–925, 2009.
- [13] P. M. Potey and K. Tuckley, "Design of wearable textile antenna with various substrate and investigation on fabric selection," in *Proceedings of the 2018 3rd International Conference on Microwave and Photonics (ICMAP)*, pp. 1–2, Dhanbad, India, February 2018.
- [14] A. Tsoilis, W. Whittow, A. Alexandridis, and J. Vardaxoglou, "Embroidery and related manufacturing techniques for wearable antennas: challenges and opportunities," *Electronics*, vol. 3, no. 2, pp. 314–338, 2014.
- [15] A. Kiourti and J. L. Volakis, "High-geometrical-accuracy embroidery process for textile antennas with fine details," *IEEE Antennas and Wireless Propagation Letters*, vol. 14, pp. 1474–1477, 2015.
- [16] T. Kaufmann, I. Fumeaux, and C. Fumeaux, "Comparison of fabric and embroidered dipole antennas," in *Proceedings of the 2013 7th European Conference on Antennas and Propagation (EuCAP)*, pp. 3252–3255, Gothenburg, Sweden, April 2013.
- [17] B. Ivsic, D. Bonafacic, and J. Bartolic, "Considerations on embroidered textile antennas for wearable applications," *IEEE Antennas and Wireless Propagation Letters*, vol. 12, pp. 1708–1711, 2013.
- [18] Y. Sun, Y. Lei, Y. Liu et al., "Design of RFID textile dipole antenna," in *Proceedings of the 2018 Cross Strait Quad-Regional Radio Science and Wireless Technology Conference (CSQRWC)*, pp. 1–2, Xuzhou, China, July 2018.
- [19] M. M. Bait-Suwailam, I. I. Labiano, and A. Alomainy, "Impedance enhancement of textile grounded loop antenna using high-impedance surface (HIS) for healthcare applications," *Sensors*, vol. 20, no. 14, p. 3809, 2020.
- [20] M. Shahidul Islam, M. T. Islam, M. A. Ullah, G. Kok Beng, N. Amin, and N. Misran, "A modified meander line microstrip patch antenna with enhanced bandwidth for 2.4 GHz ISM-band internet of things (IoT) applications," *IEEE Access*, vol. 7, pp. 127850–127861, 2019.
- [21] M. Mantash, A.-C. Tarot, S. Collardey, and K. Mahdjoubi, "Investigation of flexible textile antennas and AMC reflectors," *International Journal of Antennas and Propagation*, vol. 2012, Article ID 236505, 10 pages, 2012.
- [22] A. Y. I. Ashyap, Z. Z. Abidin, S. H. Dahlan et al., "Compact and low-profile textile EBG-based antenna for wearable medical applications," *IEEE Antennas and Wireless Propagation Letters*, vol. 16, pp. 2550–2553, 2017.
- [23] M. E. Lajevardi and M. Kamyab, "Ultraminaturized metamaterial-inspired SIW textile antenna for off-body applications," *IEEE Antennas and Wireless Propagation Letters*, vol. 16, pp. 3155–3158, 2017.
- [24] BERNINA-720, <https://www.bernina.com/en-IN/MachinesIN/S%20eries-Overview/BERNINA-7-Series/BERNINA-720>.

- [25] C. Gabriel, "Compilation of the dielectric properties of body tissues at RF and microwave frequencies," Brooks Air Force, San Antonio, TX, USA, AL/OE-TR-1996-0037, 1996.
- [26] S. Yan, V. Volskiy, and G. A. E. Vandenbosch, "Compact dual-band textile PIFA for 433 MHz/2.4 GHz ISM bands," *IEEE Antennas and Wireless Propagation Letters*, vol. 16, pp. 2436–2439, 2017.
- [27] R. Bharadwaj, C. Parini, and A. Alomainy, "Experimental investigation of 3-D human body localization using wearable ultra-wideband antennas," *IEEE Transactions on Antennas and Propagation*, vol. 63, no. 11, pp. 5035–5044, 2015.
- [28] R. Bharadwaj and S. K. Koul, "Experimental analysis of ultra-wideband body-to-body communication channel characterization in an indoor environment," *IEEE Transactions on Antennas and Propagation*, vol. 67, no. 3, pp. 1779–1789, 2019.
- [29] S. Sankaralingam and B. Gupta, "Development of textile antennas for body wearable applications and investigations on their performance under bent conditions," *Progress in Electromagnetics Research B*, vol. 22, pp. 53–71, 2010.
- [30] D. Ferreira, P. Pires, R. Rodrigues, and R. F. S. Caldeirinha, "Wearable textile antennas: examining the effect of bending on their performance," *IEEE Antennas and Propagation Magazine*, vol. 59, no. 3, pp. 54–59, 2017.
- [31] A. Kavitha and J. N. Swaminathan, "Design of flexible textile antenna using FR4, jeans cotton and teflon substrates," *Microsystem Technologies*, vol. 25, pp. 1311–1320, 2019.
- [32] P. Balaji and R. Narmadha, "Wearable E-shaped textile antenna for biomedical telemetry," in *Proceedings of the 2021 International Conference on Advances in Electrical, Computing, Communication and Sustainable Technologies (ICAAECT)*, pp. 1–5, Bhilai, India, February 2021.
- [33] G. Atanasova and N. Atanasov, "Small antennas for wearable sensor networks: impact of the electromagnetic properties of the textiles on antenna performance," *Sensors*, vol. 20, no. 18, p. 5157, 2020.
- [34] R. Sanchez-Montero, P. L. Lopez-Espi, C. Alen-Cordero, and J. A. Martinez-Rojas, "Bend and moisture effects on the performance of a U-shaped slotted wearable antenna for off-body communications in an industrial scientific medical (ISM) 2.4 GHz band," *Sensors*, vol. 19, no. 8, p. 1804, 2019.
- [35] E. F. Sundarsingh and V. S. Ramalingam, "Design and experimental evaluation of a novel on-body textile antenna for unicast applications," *Microwave and Optical Technology Letters*, vol. 62, pp. 789–799, 2020.
- [36] K. Masrakin, H. A. Rahim, P. J. Soh et al., "Assessment of worn textile antennas' exposure on the physiological parameters and well-being of adults," *IEEE Access*, vol. 7, pp. 98946–98958, 2019.
- [37] H. I. Azeez, H.-C. Yang, and W.-S. Chen, "Wearable triband E-shaped dipole antenna with low SAR for IoT applications," *Electronics*, vol. 8, no. 6, p. 665, 2019.
- [38] K. N. Paracha, S. K. Abdul Rahim, P. J. Soh, and M. Khalily, "Wearable antennas: a review of materials, structures, and innovative features for autonomous communication and sensing," *IEEE Access*, vol. 7, pp. 56694–56712, 2019.

Research Article

A Novel Multiband Fractal Antenna for Wireless Application

Lan Wang , Jianguo Yu , Tangyao Xie, and Kun Bi

Beijing Key Laboratory of Work Safety Intelligent Monitoring (Beijing University of Posts and Telecommunications),
Beijing, China

Correspondence should be addressed to Lan Wang; 1879426363@qq.com and Jianguo Yu; yujianguo241401@163.com

Received 25 March 2021; Revised 28 April 2021; Accepted 3 June 2021; Published 17 June 2021

Academic Editor: Taimoor Khan

Copyright © 2021 Lan Wang et al. This is an open access article distributed under the Creative Commons Attribution License, which permits unrestricted use, distribution, and reproduction in any medium, provided the original work is properly cited.

This paper proposes a novel multiband antenna using circle and triangle fractals for wireless application. By cutting a triangle slot in the circular monopole, a novel fractal method of the circular nested triangle structure is presented. The above structure is iterated four times, which forms the proposed fractal antenna. The antenna adopts the microstrip feeding method. In order to improve out band rejection and expand bandwidth, a ring resonator is designed on the back of the dielectric plate. The designed antenna covers 1.8 GHz–2.9 GHz applied to Bluetooth, TD-SCDMA, WCDMA, CDMA2000, and LTE33-41, 3.4 GHz–4.6 GHz applied to LTE 42/43 and WiMAX, and 5 GHz–5.6 GHz applied to WLAN. The substrate is FR4 with a dielectric constant of 4.4 and a loss tangent of 0.02. The size of the fabricated antenna is $87.5 \times 61 \times 1.6$ mm. The measured pick gain achieves 2.98 dBi, 2.58 dBi, and 3.34 dBi at 2.6 GHz, 3.8 GHz, and 5.3 GHz, respectively. The measurement and simulation results are in good agreement, which verifies the rationality of the design.

1. Introduction

With the advancement of wireless communication technology, multiband antenna has played a very crucial role in the wireless personal area network [1–9]. Mobile devices, such as hand-held computers and smart phones, are widely using wireless local area network (WLAN) and worldwide interoperability for microwave access (WiMAX) [10–14]. The WLAN/WiMAX module, used to avail of these environments, is capable of operating at multiple frequency bands. The typical frequency bands required for a single antenna are therefore 2.4, 5.2, 5.4, and 5.8 GHz for WLAN applications, 3.3–3.8 GHz for WiMAX, and 2.4–2.484 GHz for Bluetooth applications [15–18]. The use of printed technology is the best choice since it allows to design low-cost planar antennas with high performances and compact size. Moreover, a printed antenna can be easily integrated into front-end circuits, providing low profile and a relatively simple fabrication [3, 19–21]. Therefore, a number of printed antennas with different geometries have been experimentally characterized to enhance the bandwidth for wireless applications. In the work by Gautam et al. [22], a low-profile planar triple-band microstrip antenna was used for WLAN/WiMAX

applications. The proposed antenna consists of F-shaped slot radiators and a defected ground plane. In the work by Augustin and Denidni [23], a multiband trapezoidal monopole antenna is proposed, which is fed by coplanar waveguide (CPW). Linear and circular polarizations are realized in a single substrate layer. In the work by Li and Mao [24], a novel Koch-like fractal curve is proposed. A small isosceles triangle is cut off from center of each side of the initial isosceles triangle; then, the procedure iterates along the sides like Koch curve does, forming the Koch-like fractal bow-tie geometry. In the study by Liu et al. [25], an optically controlled aperture ultrawideband antenna is presented, which is able to generate reconfigurable multiband notches. Two independent narrow-band complementary split ring resonators are controlled by two optically controlled microwave switches. In the work by Kunwar et al. [26], inverted L-slot patch with a defected ground plane is used for triple-band operation. A frequency-agile triple-band microstrip antenna using the defected ground structure is presented in [27]. MTM-inspired reactive loading and metamaterial transmission lines are used in [28, 29]. All the reported antennas exhibit multiband characteristic. However, bandwidths of these antennas are not wide enough to cover many

applications, and the structures are complex. The proposed antenna in this paper occupies the wider bandwidth and has simpler geometry, while ensuring the gain and efficiency performance. The proposed antenna structure is simple. It is easy to be fabricated. Moreover, the antenna model is extensible. On the basis of the proposed structure, the antenna can be fractal more times inward for higher frequency and can be fractal outward for lower frequency. Performance comparison of the proposed antenna with other antennas is shown in Table 1.

In this paper, a multiband antenna using a novel circle and triangle structures fractals is proposed and designed for wireless communication systems that can support Bluetooth/WCDMA/CDMA2000/LTE3341WLAN/WiMAX applications. The proposed antenna consists of a main fractal radiator, a $50\ \Omega$ microstrip feed line, a ring resonator, and a partial ground plane on the back of the substrate. The proposed antenna shows three distinct resonances with impedance bandwidths of 1.8–2.9 GHz (1.1 GHz), 3.4–4.6 GHz (1.2 GHz), and 5.0–5.6 GHz (0.6 GHz), respectively. The antenna configuration has a compact size of $87.5\ \text{mm} \times 61\ \text{mm}$. The antenna design and studies are described in Section 2. Section 3 includes results and discussion, which are followed by the conclusion in Section 4.

2. Antenna Design and Analysis

Firstly, a triangular gap is nested in a circular radiation patch. This basic geometry is called first-order fractal, as shown in Figure 1(a). The second step is to make an inscribed circle on the triangle gap and nest a triangular gap in the inscribed circle. The rest can be done in the same manner; the antenna radiator adopts four iterations of the square nested triangle slot fractal structure. The final configuration and size parameters of the proposed antenna are shown in Figure 2 and Table 2. In order to make the current flowing through the antenna surface longer, a certain distance d is kept between the circle and the top of the triangle. There is a certain proportion between the dimensions:

$$\begin{aligned} R_n &= \frac{(R_n - d)}{2}, \quad n = 1, 2, 3, \text{ and } 4, \\ a_n &= \sqrt{3} * (R_n - d), \quad n = 1, 2, \text{ and } 3. \end{aligned} \quad (1)$$

By optimizing the antenna radiating slot, the current direction on the metal surface of the microstrip antenna can be changed to achieve multiband coverage. In order to achieve multiband, while improving out band rejection and expanding bandwidth, a resonator ring is designed on the back side of the dielectric board. The current will be coupled to the resonant ring when it flows through the radiator, resulting in disturbing of the current direction and generating multiple resonance frequency points.

Figure 3 shows the reflection coefficient S_{11} of the antenna with different iterations, respectively. For the first and second iteration, S_{11} at the resonance point becomes smaller with the increase of iteration times. For the third iteration, reflection loss characteristics are not improved, but another resonance frequency appears at 4.6 GHz. S_{11} becomes further deeper for the

fourth fractal. The antenna property tends to be stable and the best matching status. Compared with the antenna with no resonant ring, the introduction of the resonant ring can improve the reflection coefficient characteristics, increase the resonance points, and effectively expand the bandwidth.

The black solid line presents the simulated reflection coefficient S_{11} of the final proposed antenna. The antenna covers three different frequency bands. At the center frequency, S_{11} is $-26\ \text{dB}$ at 2.6 GHz, $-30\ \text{dB}$ at 3.8 GHz, and $-15\ \text{dB}$ at 5.3 GHz, respectively. The simulated impedance bands with $S_{11} \leq -10\ \text{dB}$ are 46.2% from 1.8 GHz to 3.2 GHz, 31.6% from 3.4 GHz to 4.6 GHz, and 15.1% from 4.9 GHz to 5.7 GHz. These bands can be applied for 2G, 3G, 4G-LTE, Bluetooth, GPS, WLAN, COMPASS, GLONASS, and ISM2.4G.

As shown in Figure 4, current amplitude distribution of the antenna is presented, which illustrates the relationship between resonant frequencies and structure of the antenna. The red part represents strong current, and the blue and green parts represent weak current. Figures 4(a)–4(c) show the surface current at operation frequencies of 2.6 GHz, 3.8 GHz, and 5.3 GHz successively. In Figure 4(a), the current is mainly concentrated in the outer area of the radiator. The color of the middle area and the innermost area is mostly blue. Therefore, it can be understood that the 2.6 GHz resonance occurs due to the first fractal. In Figure 4(b), except for the part red area in the outer, there is also a lot of red in the middle. It is observed that the resonance occurs due to second fractal. The third resonant mode of the antenna, by considering the current distribution of the antenna as shown in Figure 4(c), arises from the currents in the inner area owing to the third fractal. Based on the above analysis, the current flows from outside to inside with the frequency increasing. According to $f = c/\lambda$, it can be known that the small size of the antenna produces high radiation frequency. Therefore, the resonance frequency generated by the inner ring is higher than the resonance frequency generated by the outer ring.

For the first resonance at 2.6 GHz, the maxima of the current occur in the outer ring. The length of the radiating patch responsible for first resonance can be calculated as

$$L_1 \approx 2 * \pi * R_4 * \frac{1}{3} \approx 50.24\ \text{mm}. \quad (2)$$

At the resonance, the length would be half of the wavelength. L_1 should be $\lambda/2$. For the printed antenna, half of it is on the media plate and the other half is in the air. The calculated wavelength should be between the medium wavelength and the free space wavelength. We take the intermediate value as the estimation temporarily to verify the rationality of the fractal design.

Therefore,

$$f_1 \approx \frac{1}{2} * \left(\frac{c}{2L_1\sqrt{\epsilon_r}} + \frac{c}{2L_1} \right) \approx 2.2\ \text{GHz}. \quad (3)$$

For the second resonance at 3.8 GHz, the maxima of the current occur in the middle ring. The length of the radiating patch responsible for second resonance can be calculated as

TABLE 1: Performance comparison of the proposed antenna with other antennas.

Ref.	Bands (GHz)	Gain (dBi)	Efficiency
[22]	2.0–2.76, 3.04–4.0, 5.2–6.0, and 5.2–5.8	1.5–3.05	87%–95%
[23]	2.21–4.40 and 5.13–5.55	0.5–2	66%–72%
[24]	1.71–2.03 and 5.02–5.28	3.5–7	60%–80%
[25]	2.2–2.9, 3.2–4.7, and 4.8–6.6	0–1	—
[26]	2.39–2.51, 3.15–3.91, and 4.91–6.08	1.6–2.8	—
[27]	2–2.15, 2.75–3.52, and 5.4–5.9	—	40%–70%
[28]	2.3–4 and 5–6.6	2.3–3.2	61.7%–76.5%
[29]	2.42–3.51	2.1	96.5%
Proposed	1.8–2.9, 3.4–4.6, and 5–5.6	2.58–3.34	75.8%–95.0%

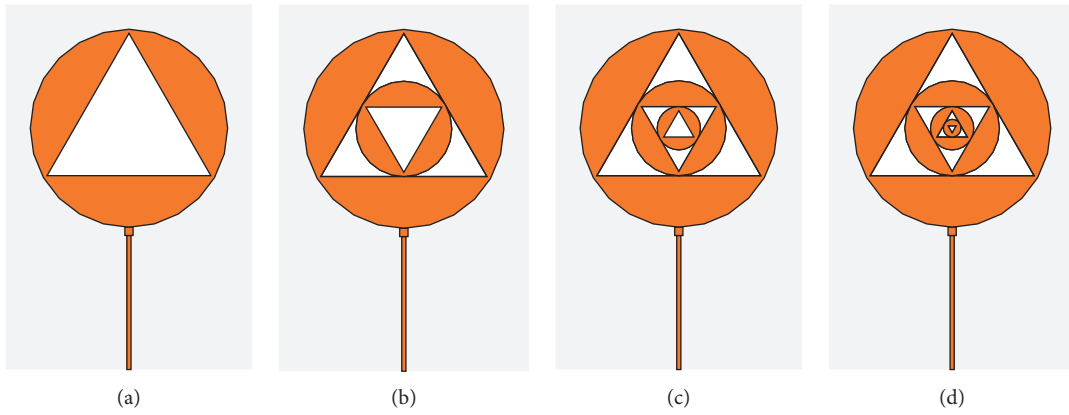


FIGURE 1: Fractal progress.

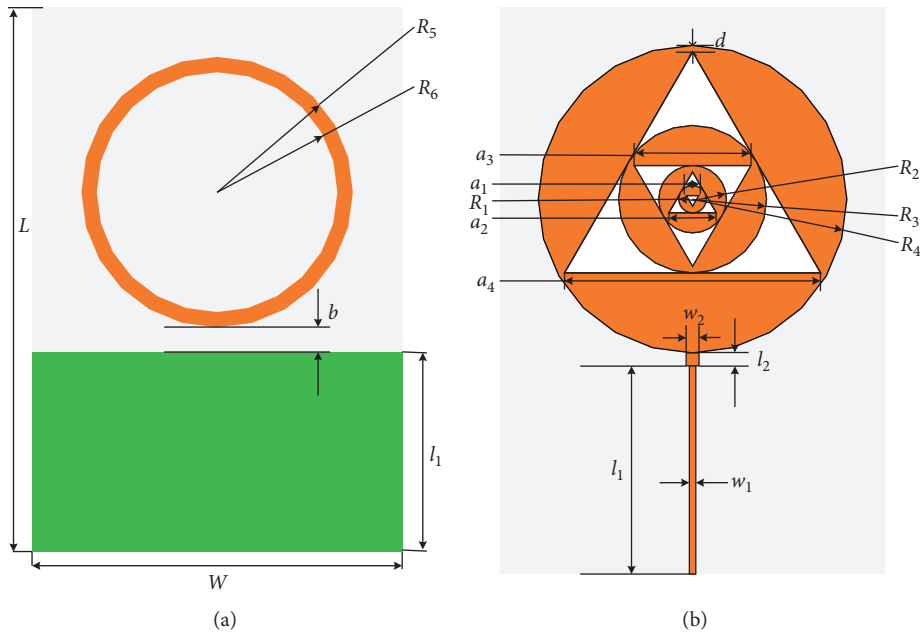
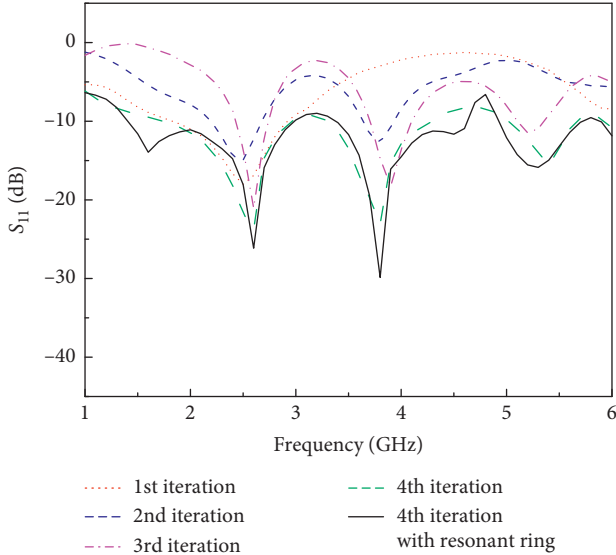


FIGURE 2: The configuration of the antenna: (a) bottom view; (b) top view.

TABLE 2: The dimensions of the proposed antenna.

Parameter	Values (mm)
W	61
w_1	1
w_2	2
R_1	2.125
R_3	11.5
R_5	22
a_1	1.95
a_3	18.19
b	4
L	87.5
l_1	32.5
l_2	2
R_2	5.25
R_4	24
R_6	19.5
a_2	7.36
a_4	39.84
d	1

FIGURE 3: The simulated S_{11} for the antenna iterations.

$$L_2 \approx 2 * \pi * R_3 * \frac{1}{3} \approx 24.07 \text{ mm},$$

$$f_2 \approx \frac{1}{2} * \left(\frac{c}{2L_2\sqrt{\epsilon_r}} + \frac{c}{2L_2} \right) \approx 4.5 \text{ GHz}. \quad (4)$$

For the third resonance at 5.3 GHz, the maxima of the current occur in the inner ring. The length of the radiating patch responsible for third resonance can be calculated as

$$L_3 \approx 2 * \pi * R_2 * \frac{2}{3} \approx 21.98 \text{ mm},$$

$$f_3 \approx \frac{1}{2} * \left(\frac{c}{2L_3\sqrt{\epsilon_r}} + \frac{c}{2L_3} \right) \approx 5.0 \text{ GHz}. \quad (5)$$

The 3D pattern of the designed antenna is shown in Figure 5, and the E/H plane polarization is shown in

Figure 6. The blue solid line represents coplanar polarization, and the red dotted line represents cross polarization. It can be seen from the figure that the three-dimensional spatial radiation field at three resonance points has certain changes. With the increase of the resonance frequency, the radiation directivity of the antenna becomes stronger. The main lobe becomes smaller, weak side lobes appear, and directivity becomes complicated. The maximum gain can achieve 3.33 dBi, 3.82 dBi, and 5.77 dBi at central frequencies of 2.6 GHz, 3.8 GHz, and 5.3 GHz, respectively.

3. Results and Discussion

The proposed multiband antenna is manufactured on a 1.6 mm thick FR4 substrate with a dielectric constant of 4.4 and a loss tangent of 0.02. The copper with 0.03 mm thick is laid over the patch and ground plane. The prototype of the fabricated antenna is shown in Figure 7.

The Keysight Technologies FieldFox Handheld Microwave Analyzer N9917A is used to measure the reflection coefficient of the fabricated antenna. Figure 8 illustrates the comparison of simulated and measured results. The measured -10 dB bandwidth is 42.5% from 1.8 GHz to 2.9 GHz, 30% from 3.4 GHz to 4.6 GHz, and 5.3% from 5 GHz to 5.6 GHz, which is in good agreement with the simulation result. The commercial band coverage is shown in Table 3. Slight discrepancies between measurement and simulation results may be caused by fabrication precision, interface error, and test environment. The substrate thickness of the antenna is only 1.6 mm, and the influence of the dielectric thickness change during the processing on the performance of the antenna cannot be ignored. The connection method of SMA between the feeder and the signal is solder connection. The solder increases the thickness of the dielectric board, which has a certain impact on the test results. The error is within the allowable range.

Figure 9 displays the measured 3D radiation patterns at central frequency of 2.5 GHz, 3.8 GHz, and 5.3 GHz, respectively. The pick gain can achieve 2.98 dBi, 2.58 dBi, and 3.34 dBi at frequencies of 2.5 GHz, 3.8 GHz, and 5.3 GHz, respectively. The measured radiation patterns are nearly omnidirectional. With the frequency increasing, the generation of higher order modes increases the side lobes.

Gain and efficiency variation with the frequency is shown in Figure 10. It is found that the gain varies from 1.9 to 4.1 dBi in I band, from 0.5 to 4.0 dBi in II band, and from 1.2 to 3.3 dBi in III band. The radiation efficiency of the antenna can achieve 92.5%, 75.5%, and 95.0% at central frequency of 2.5 GHz, 3.8 GHz, and 5.3 GHz. The test results are consistent with the simulation results basically. However, when testing the antenna pattern in the dark room, it is inevitable to connect the antenna to the test equipment with radio frequency cables and connectors. These RF cables and connectors are very close to the antenna, and their radiation will affect the pattern test. Therefore, it is inevitable that there is a certain deviation between the test results and the simulation results.

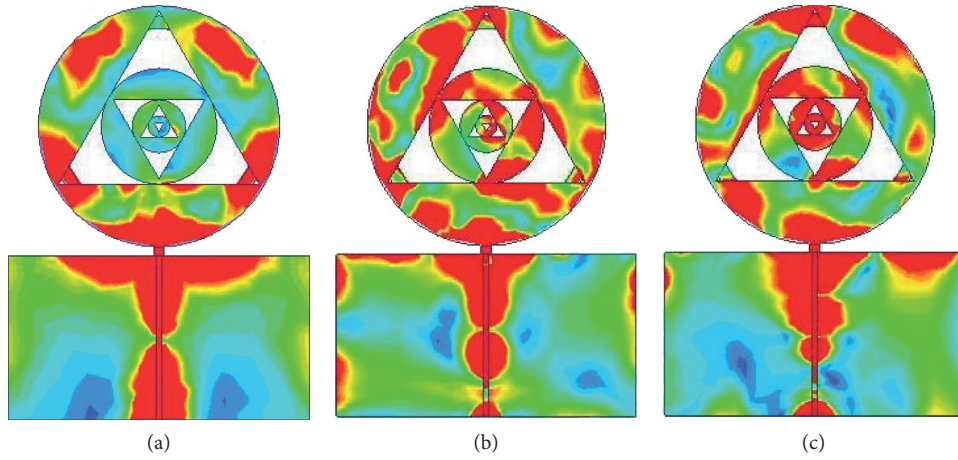


FIGURE 4: Current amplitude and vector distribution of the antenna at (a) 2.6 GHz, (b) 3.8 GHz, and (c) 5.3 GHz.

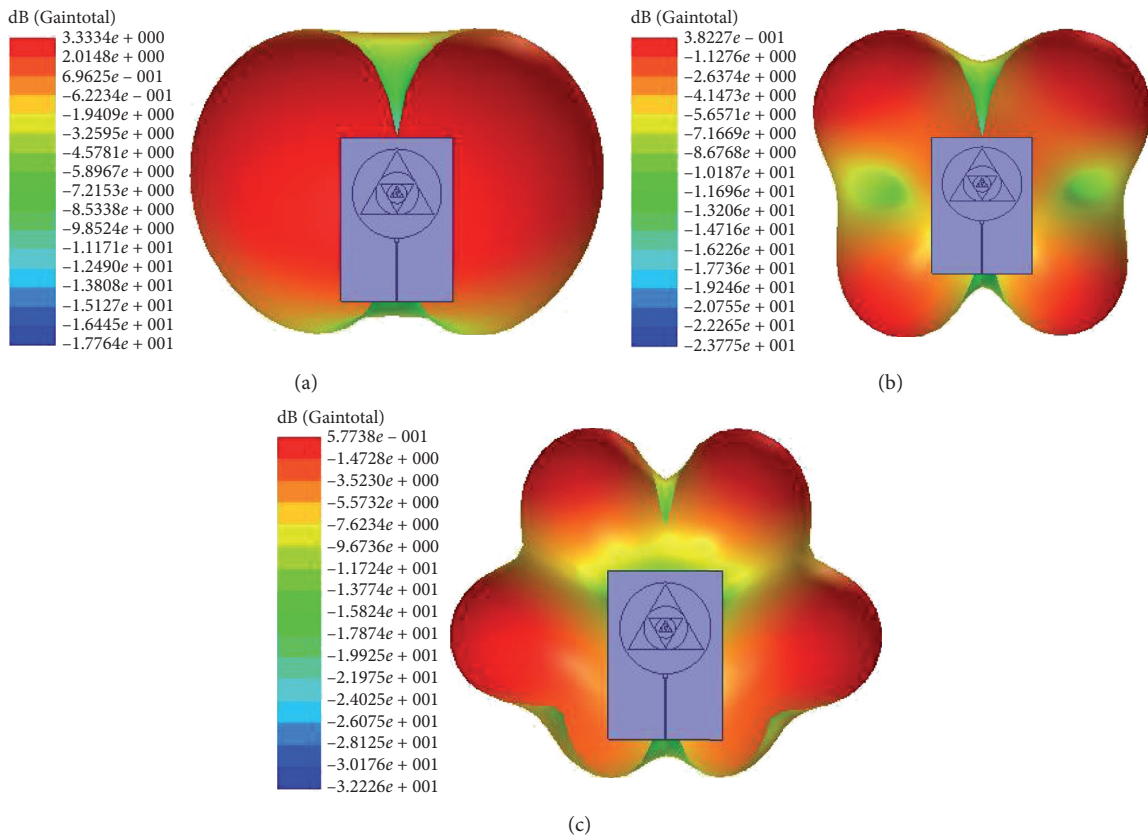


FIGURE 5: 3D radiation pattern at (a) 2.6 GHz, (b) 3.8 GHz, and (c) 5.3 GHz.

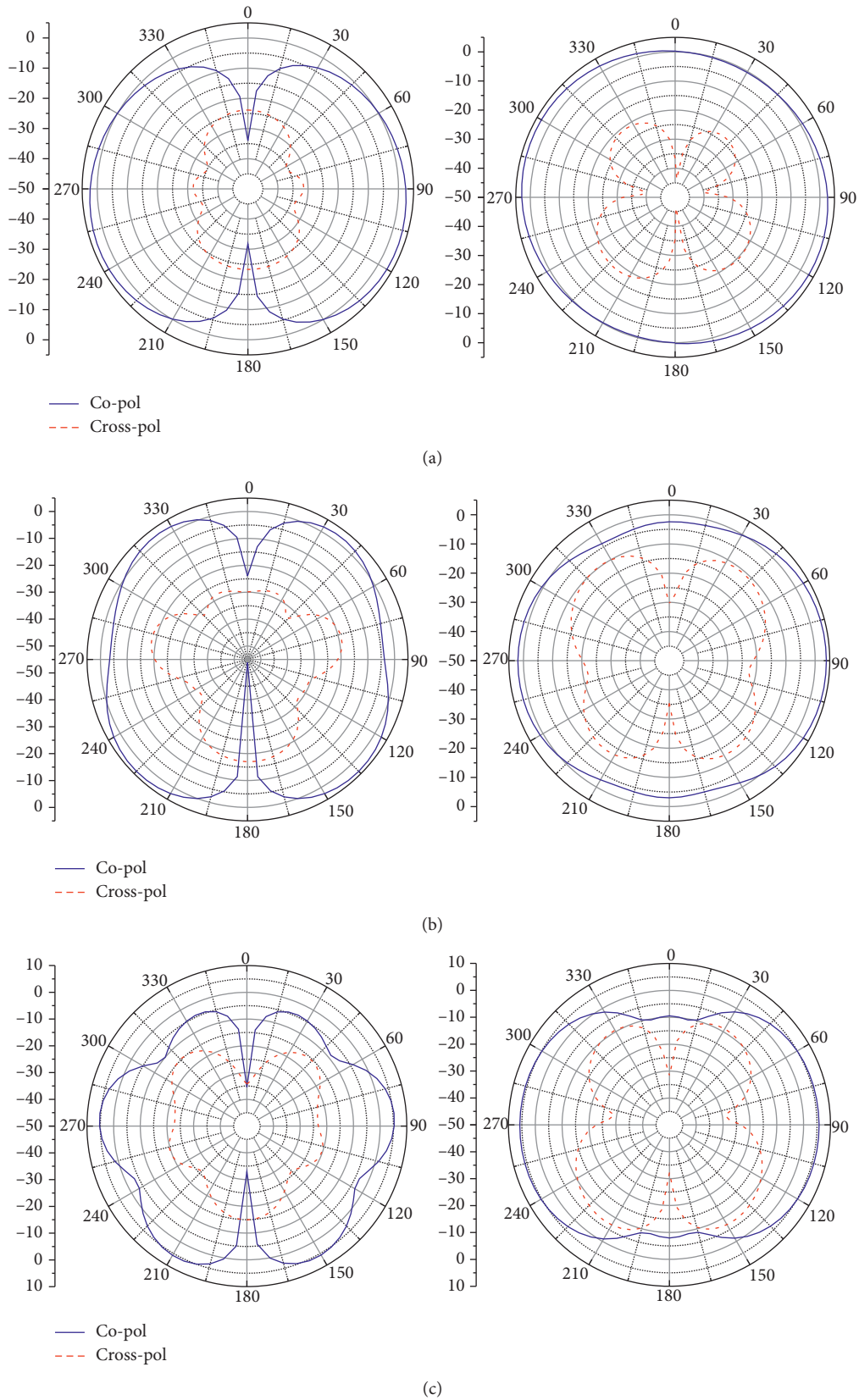


FIGURE 6: E/H plane polarization. (a) 2.6 GHz. (b) 3.8 GHz. (c) 5.3 GHz.

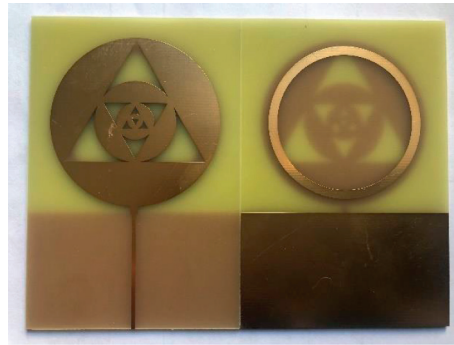


FIGURE 7: The configuration of the proposed antenna.

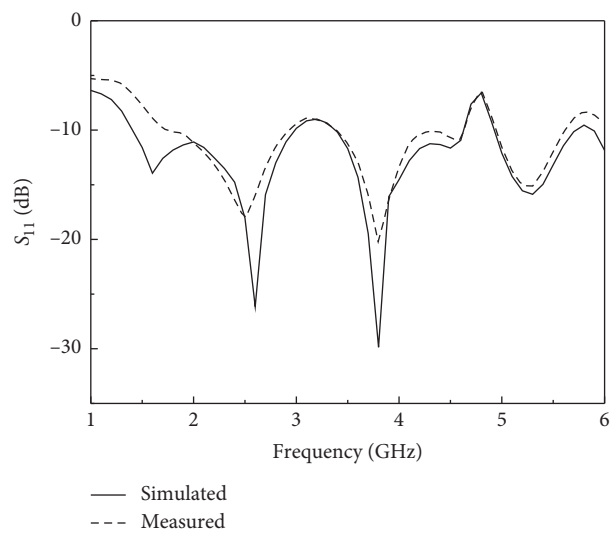


FIGURE 8: The comparison of simulated and measured S_{11} .

TABLE 3: Commercial band coverage by the designed antenna.

Frequency band	Bandwith	Commercial band coverage
1	1.8–2.9 GHz (42.5%)	TD-SCDMA (1880–2025 MHz) WCDMA (1920–2170 MHz) CDMA2000 (1920–2125 MHz) LTE33-41 (1900–2690 MHz) Bluetooth
2	3.4–4.6 GHz (30%)	LTE42/43 (3.4–3.8 GHz) WiMAX (3.3–3.8 GHz)
3	5.0–5.6 GHz (11.3%)	WLAN (802.11a/n:5.15–5.35 GHz)

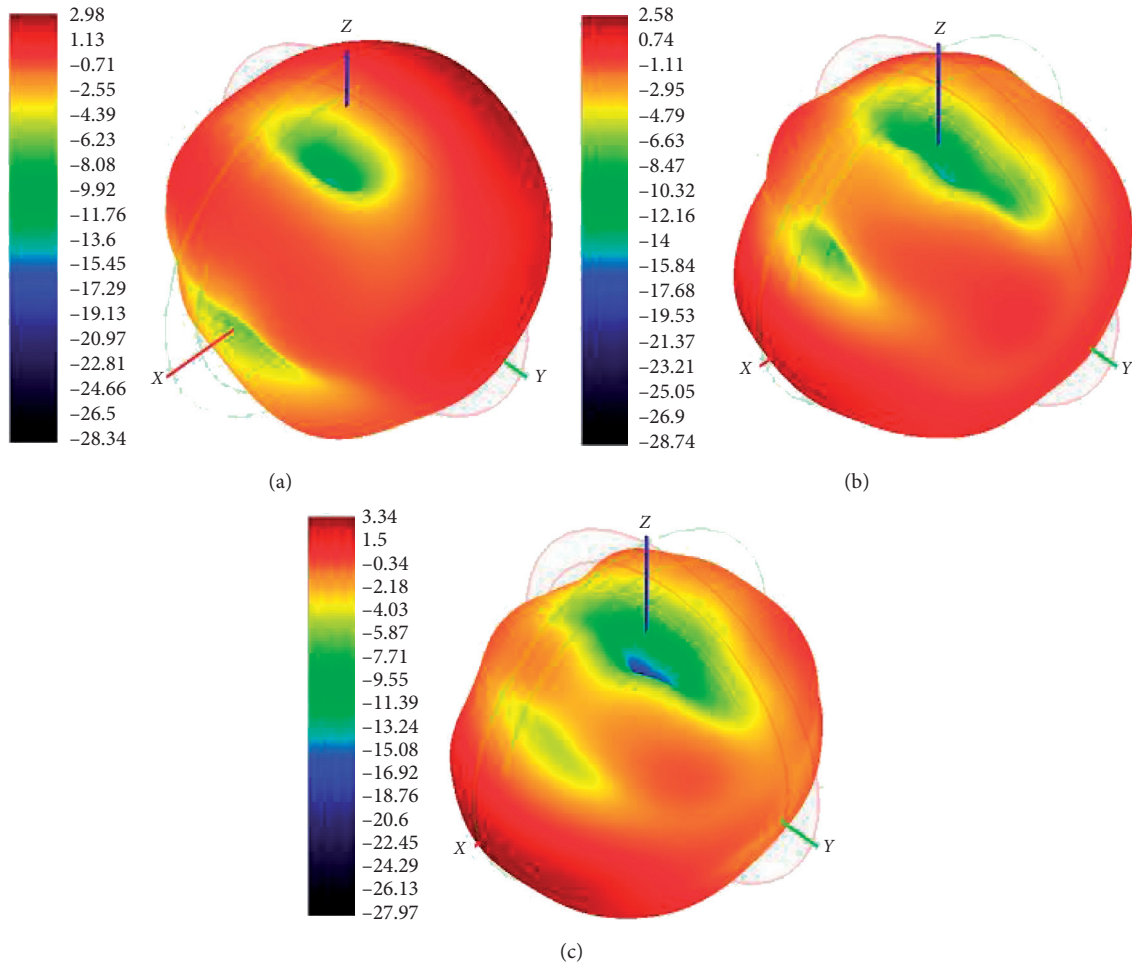


FIGURE 9: The measured 3D pattern. (a) 2.5 GHz. (b) 3.8 GHz. (c) 5.3 GHz.

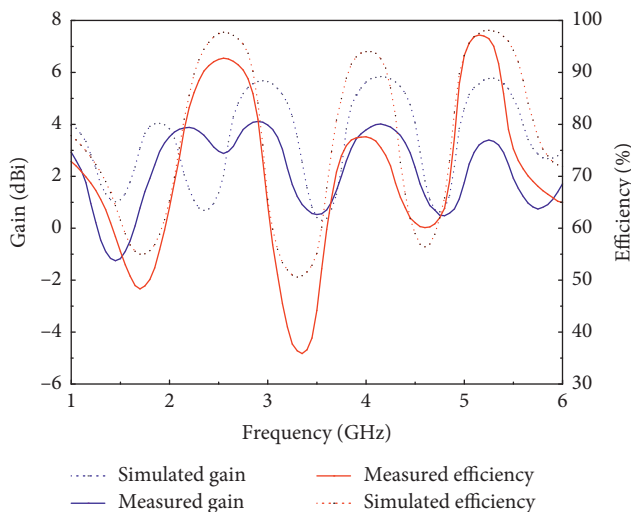


FIGURE 10: Gain and efficiency of the antenna.

4. Conclusion

In this paper, an optimal microstrip-fed printed antenna with a novel circular nested triangle slotting multiband

fractal is successfully proposed, simulated, and fabricated. The antenna consists of four parts, including a main fractal radiator, a $50\ \Omega$ microstrip feed line, a ring resonator, and a partial ground plane on the back of the substrate. The antenna is designed on a single-layer FR4 and covers the frequency of 1.8 GHz–2.9 GHz, 3.4 GHz–4.6 GHz, and 5 GHz–5.6 GHz. Experiments are carried out to validate the design concept and method, showing good agreement between simulations and measurements. At all frequency bands, the proposed antenna features stable radiation performance indicating that it can be a good candidate for Bluetooth, TD-SCDMA, WCDMA, CDMA2000, LTE33-41, WLAN, and WiMAX applications.

Data Availability

The data used to support the findings of this study are included within the article.

Conflicts of Interest

The authors declare that they have no conflicts of interest.

Acknowledgments

This work was supported by the National Natural Science Foundation of China (nos. 61531007 and 61821001).

References

- [1] S. Singhal, P. Singh, and A. Kumar Singh, "Asymmetrically CPW-fed octagonal sierpinski UWB fractal antenna," *Microwave and Optical Technology Letters*, vol. 58, no. 7, pp. 1738–1745, 2016.
- [2] T. Nguyen-Trung, Y. Yang, K.-Y. Lee, and K. C. Hwang, "Dual circularly-polarized spidron fractal slot antenna," *Electromagnetics*, vol. 37, no. 1, pp. 40–48, 2017.
- [3] R. K. Yadav, J. Kishor, and R. L. Yadava, "A chaucer microstrip fractal antenna for mobile applications," *Journal of Communications Technology and Electronics*, vol. 61, no. 2, pp. 138–144, 2016.
- [4] K.-L. Wong and L.-C. Lee, "Multiband printed monopole slot antenna for WWAN operation in the laptop computer," *IEEE Transactions on Antennas and Propagation*, vol. 57, no. 2, pp. 324–330, 2009.
- [5] Y.-S. Shin, B.-N. Kim, and W. I. Seong-Ook Park, "GSM/DCS/IMT-2000 triple-band built-in antenna for wireless terminals," *IEEE Antennas and Wireless Propagation Letters*, vol. 3, no. 1, pp. 104–107, 2004.
- [6] W. J. Krzysztofik, "Modified sierpinski fractal monopole for ISM-bands handset applications," *IEEE Transactions on Antennas and Propagation*, vol. 57, no. 3, pp. 606–615, 2009.
- [7] C.-J. Wang and K.-L. Hsiao, "CPW-fed monopole antenna for multiple system integration," *IEEE Transactions on Antennas and Propagation*, vol. 62, no. 2, pp. 1007–1011, 2014.
- [8] K. Yu, Y. S. Li, W. H. Yu et al., "A compact triple band antenna for bluetooth, WLAN and WiMAX applications," *Applied Computational Electromagnetics Society Journal*, vol. 32, no. 5, pp. 424–429, 2017.
- [9] H. Oraizi and S. Hedayati, "Circularly polarized multiband microstrip antenna using the square and giuseppe peano fractals," *IEEE Transactions on Antennas and Propagation*, vol. 60, no. 7, pp. 3466–3470, 2012.
- [10] P. S. Bakariya, S. Dwari, M. Sarkar, and M. K. Mandal, "Proximity-coupled microstrip antenna for bluetooth, WiMAX, and WLAN applications," *IEEE Antennas and Wireless Propagation Letters*, vol. 14, pp. 755–758, 2015.
- [11] S. C. Basaran, U. Olgun, and K. Sertel, "Multiband monopole antenna with complementary split-ring resonators for WLAN and WiMAX applications," *Electronics Letters*, vol. 49, no. 10, pp. 636–638, 2013.
- [12] J. H. Yoon, Y. C. Rhee, and Y. K. Jang, "Compact monopole antenna design for WLAN/WiMAX triple-band operations," *Microwave and Optical Technology Letters*, vol. 54, no. 8, pp. 1838–1846, 2012.
- [13] L. Kumar, A. Gautam, B. Kanaujia et al., "Design of compact F-shaped slot triple band antenna for WLAN/WiMAX applications," *IEEE Transactions on Antennas & Propagation*, vol. 64, no. 3, pp. 1101–1105, 2016.
- [14] W. Hu, Y.-Z. Yin, and P. Xi Yang, "Compact triband square-slot antenna with symmetrical L-strips for WLAN/WiMAX applications," *IEEE Antennas and Wireless Propagation Letters*, vol. 10, pp. 462–465, 2011.
- [15] A. Kunwar, A. K. Gautam, and B. K. Kanaujia, "Inverted L-slot triple-band antenna with defected ground structure for WLAN and WiMAX applications," *International Journal of Microwave and Wireless Technologies*, vol. 9, no. 1, pp. 191–196, 2017.
- [16] A. Foudazi, H. R. Hassani, and S. Mohammad Ali Nezhad, "Small UWB planar monopole antenna with added GPS/GSM/WLAN bands," *IEEE Transactions on Antennas and Propagation*, vol. 60, no. 6, pp. 2987–2992, 2012.
- [17] M. Rafaei Booket, A. Jafargholi, M. Kamyab et al., "Compact multi-band printed dipole antenna loaded with single-cell metamaterial," *IET Microwaves, Antennas & Propagation*, vol. 6, no. 1, pp. 12–23, 2012.
- [18] M. Tzortzakakis and R. J. Langley, "Quad-band internal mobile phone antenna," *IEEE Transactions on Antennas and Propagation*, vol. 55, no. 7, pp. 2097–2103, 2007.
- [19] H. W. Hsieh, Y.-C. Lee, K.-K. Tiong, and J.-S. Sun, "Design of a multiband antenna for mobile handset operations," *IEEE Antennas and Wireless Propagation Letters*, vol. 8, pp. 200–203, 2009.
- [20] M. Naghshvarian Jahromi, A. Falahati, R. M. Edwards et al., "Bandwidth and impedance-matching enhancement of fractal monopole antennas using compact grounded coplanar waveguide," *IEEE Transactions on Antennas and Propagation*, vol. 59, no. 7, pp. 2480–2487, 2011.
- [21] S. Dhar, K. Patra, R. Ghatak, B. Gupta, and D. R. Poddar, "A dielectric resonator-loaded minkowski fractal-shaped slot loop heptaband Antenna," *IEEE Transactions on Antennas and Propagation*, vol. 63, no. 4, pp. 1521–1529, 2015.
- [22] A. K. Gautam, L. Kumar, B. K. Kanaujia, and K. Rambabu, "Design of compact F-shaped slot triple-band antenna for WLAN/WiMAX applications," *IEEE Transactions on Antennas and Propagation*, vol. 64, no. 3, pp. 1101–1105, 2016.
- [23] G. Augustin and T. A. Denidni, "Coplanar waveguide-fed uniplanar trapezoidal antenna with linear and circular polarization," *IEEE Transactions on Antennas and Propagation*, vol. 60, no. 5, pp. 2522–2526, 2012.
- [24] D. Li and J.-f. Mao, "A koch-like sided fractal bow-tie dipole antenna," *IEEE Transactions on Antennas and Propagation*, vol. 60, no. 5, pp. 2242–2251, 2012.
- [25] X. Liu, M. M. Tentzeris, and S. H. Zheng, "Optically controlled reconfigurable band-notched UWB antenna for cognitive radio systems," *Electronics Letters*, vol. 50, no. 21, pp. 1502–1504, 2014.
- [26] A. Kunwar, A. K. Gautam, and B. K. Kanaujia, "Inverted L-slot triple-band antenna with defected ground structure for WLAN and WiMAX applications," *International Journal of Microwave and Wireless Technologies*, vol. 9, no. 1, pp. 191–196, 2017.
- [27] S. Joshi, A. K. Gautam, and R. Upadhyay, "Frequency agile triple band microstrip antenna for WLAN/WiMAX application," *International Journal of Future Computer and Communication*, vol. 3, no. 4, pp. 258–261, 2014.
- [28] H. Huang, Y. Liu, S. Zhang, and S. Gong, "Multiband metamaterial-loaded monopole antenna for WLAN/WiMAX applications," *IEEE Antennas and Wireless Propagation Letters*, vol. 14, pp. 662–665, 2015.
- [29] C. Zhou, G. Wang, J. Liang, Y. Wang, and B. Zong, "Broadband antenna employing simplified MTLs for WLAN/WiMAX applications," *IEEE Antennas and Wireless Propagation Letters*, vol. 13, pp. 595–598, 2014.